

Micro and nanostructured lithium niobate for integrated nonlinear optics

Dissertation
zur Erlangung des akademischen Grades
doctor rerum naturalium (Dr. rer. nat.)

vorgelegt dem Rat der Physikalisch-Astronomischen Fakultät
der Friedrich-Schiller-Universität Jena

von Diplom-Physiker Reinhard Geiß
geboren am 21.04.1983 in Jena

Gutachter

1. Prof. Dr. Thomas Pertsch, Friedrich-Schiller-Universität Jena
2. Prof. Dr. Detlef Kip, Helmut-Schmidt-Universität Hamburg
3. Prof. Dr. Arnan Mitchell, RMIT University Melbourne

Tag der Disputation: 22.11.2016

Table of contents

Table of contents	I
1 Introduction	3
2 Fundamental concepts and methods	15
2.1 Properties of lithium niobate	15
2.2 Electromagnetic wave propagation	16
2.2.1 Basic concepts of nonlinear optics	16
2.2.2 Waveguides and modal phase-matching	19
2.2.3 Optical resonators – figures of merit	20
2.2.4 Photonic band gap structures	20
2.3 Fabrication of micro and nanostructured lithium niobate	23
2.3.1 Lithography	23
2.3.2 Thin film deposition	25
2.3.3 Pattern transfer methods	26
2.3.4 Ion beam enhanced etching	27
2.4 Optical characterization techniques	30
2.4.1 Near-field characterization of photonic crystal waveguides	31
2.4.2 Tapered fiber coupling	32
2.4.3 Cross polarized scattering microscopy	33
3 Patterning of lithium niobate	36
3.1 Hydroxide solution assisted ion beam enhanced etching	36
3.1.1 Experimental conditions	37
3.1.2 Results and discussion	38
3.1.3 KOH based ion beam enhanced etching	40
3.2 Focused ion beam patterning of lithium niobate membrane substrates	42
3.2.1 Direct patterning of LNOI and helium ion irradiated LiNbO ₃ substrates	43
3.2.2 The effect of gallium contamination	44
3.3 Additional patterning approaches	46
3.3.1 Membrane thinning with ion beam etching	46
3.3.2 Circular saw dicing	47
3.3.3 Patterned SiN membrane irradiation mask	48
4 Linear and nonlinear optical properties of nanoscale waveguides	52
4.1 Planar optical waveguides	52
4.2 Freely suspended wire-type waveguides made from bulk LiNbO ₃	53
4.2.1 Fabrication by IBEE and process simulation	54
4.2.2 Optical characterization	57
4.3 Wire-type waveguides on LNOI substrates	59

4.3.1	Fabrication by KOH based IBEE	60
4.3.2	Optical characterization	62
4.4	Photonic crystal waveguides.....	64
4.4.1	Sample layout and fabrication	65
4.4.2	Optical characterization by SNOM	66
4.5	Plasmonic nanowaveguides - design considerations and fabrication	70
5	Linear and nonlinear optical properties of microsized resonators	74
5.1	Microdisk resonators.....	74
5.2	Photonic crystal waveguide cavities	77
5.3	Photonic crystal L3 cavities	80
5.3.1	Design considerations	81
5.3.2	Photonic crystal L3 cavities from bulk LiNbO ₃	82
5.3.3	Photonic crystal L3 cavities from LNOI substrates.....	88
5.3.4	Concluding comparison of bulk LiNbO ₃ and LNOI substrates for photonic crystal structures	91
5.4	Nanobeam cavities	92
6	Summary and conclusions	95
	List of abbreviations	99
	Zusammenfassung	100
	Bibliography	102
	Publications	123
	Acknowledgments	126
	Ehrenwörtliche Erklärung.....	127

1 Introduction

The development of the first functional laser in 1960[1] made a high intensity light source available that enabled the investigation of nonlinear optical effects[2]. Nonlinear, in this context, refers to the nonlinear response of the electric polarization density on the electromagnetic field of the incident light[3]. Nonlinear optics became a broad research field covering a multitude of different phenomena, including parametric frequency conversion, optical solitons or Raman scattering, and having strong impact on a similarly broad range of applications[4]. The applicability of nonlinear optical effects is particularly relying on the choice of suitable materials serving as nonlinear media. Early investigations about the nonlinear light matter interactions with different types of crystalline materials revealed that LiNbO₃ being an artificial crystal is an appropriate choice because it beneficially combines many advantageous properties[5]–[9]. LiNbO₃ has a strong second order nonlinear susceptibility[10], a large transparency range as well as large electro-optic and acousto-optic coefficients[11]. The combination of these properties made LiNbO₃ an ideal basis for nonlinear optical devices and applications in integrated optics[12]. The starting point of this development has been the advance in optical communication technologies accompanying the development of low-loss optical fibers. The unique electro-optic properties of LiNbO₃ were used to realize integrated devices for high bandwidth transmission by polarization control and amplitude or phase modulation. The strong optical nonlinearity of LiNbO₃ enables the mixing of optical signals at different frequencies for parametric amplification, second harmonic generation (SHG) and frequency conversion[12] in compact waveguide devices. Similarly, the generation of entangled photon pairs[13], efficient terahertz generation[14] and surface acoustic wave devices[15] have been realized. Well-established diffusion-based integrated waveguides in LiNbO₃ provide relatively weak confinement for propagating mode fields. Consequently, light guiding across an optical chip requires large bending radii of the waveguides, and efficient nonlinear frequency conversion requires long propagation lengths. The respective devices are typically centimeters long. Following a trend of miniaturization similar to electronics, a technological advancement is needed to realize more compact, highly efficient optical circuitry based on LiNbO₃ and to account for the growing demand for microstructured LiNbO₃ in modern integrated photonics.

In contrast to the developments in electronics, where the complementary metal-oxide-semiconductor (CMOS) technology provides a ubiquitous platform, no material or material

system serving all requirements of an ideal integrated photonics platform, including wavelength range, efficient light emission and detection, strong electro-optic and nonlinear coefficients, ease of fabrication and integration, scalability and reliability has been identified yet[16]. Amongst other materials being investigated, especially many semiconductors[17] and chalcogenide glasses[18], [19] show strong nonlinear optical responses. But in contrast to LiNbO_3 , these materials have a centrosymmetric crystal structure or are amorphous implying that only nonlinear effects of third order can be expected. An important exception is GaAs having a large second order nonlinear coefficient[20]. Nonetheless, applications for GaAs based devices are limited[21]. Another drawback of most semiconductors is related to their optical transparency window which is often significantly smaller than for LiNbO_3 . Furthermore, semiconductors are mostly lacking the capability of LiNbO_3 to be tuned by the electro-optic effect, hence, limiting their general applicability. On the contrary, when having an application in integrated optics in mind, semiconductors may be favored because they are compatible with well-established modern microstructure technology. While semiconductor patterning is well developed, the unmodified LiNbO_3 crystal is chemically very stable which makes high aspect ratio structures difficult to realize by means of standard micropatterning technologies. Therefore, several techniques have been developed that locally modify the LiNbO_3 crystal such that the subsequent etching step is enhanced. These modifications can be introduced in many ways including domain inversion[22], proton exchange[23], [24] or ion beam irradiation[25], [26]. The most promising approach is the ion beam enhanced etching (IBEE)[27] process which is of major significance for this work. It is the general aim of this work to investigate IBEE processes for micro- and nanostructured optical elements in LiNbO_3 that are based on current microstructure technology and that enable a high integration density for future integrated nonlinear optical devices. The scope of this work will be described in detail after the following review of the current state of knowledge.

Nonlinear integrated optical elements

In order to demonstrate the potential of the IBEE process for the targeted application, two very basic types of optical structures will be investigated in this work: waveguides and resonators. Both structures, when made out of an optical nonlinear medium, allow for an enhancement of the nonlinear interaction of optical fields[28]. In the case of waveguides this is achieved by confining an optical mode field during its propagation while phase-matching of the interacting mode fields can be mediated by either quasi-phase-matching[29] through periodically poled crystal domains[30] or by modal phase-matching[31]. Controlling the field

confinement and achieving phase-matching significantly enhances the efficiency of the nonlinear interaction in the waveguide. Similarly, a resonator enhances the field confinement even further at its resonance frequency. In this way, the resulting field build-up inside the resonator contributes to an efficiency enhancement of the nonlinear processes.

These general concepts found their technological realization as LiNbO₃ optical microstructures in many different configurations which are reviewed now. The review is organized following the respective patterning approaches. In doing so, it needs to be distinguished between horizontal patterning, such as planar lithography based approaches performed on the LiNbO₃ substrate surfaces, and vertical patterning for the creation of membranes or thin layers of LiNbO₃.

Membrane type LiNbO₃ substrates

Membrane type LiNbO₃ substrates are an important basis for applications in integrated optics because they can act as planar waveguides and confine the propagating mode fields close to the patterned substrate surfaces. These membranes can be realized in many different ways. The most basic approach is to grind and polish a LiNbO₃ wafer down to the required thickness which is demonstrated in[32] using a piece of periodically poled LiNbO₃ being attached to another LiNbO₃ substrate with an adhesive resin. Similarly, the two LiNbO₃ pieces can also be directly bonded without the need of an adhesive layer. In [33]–[35] it is shown how a gold strip is embedded in the surface of one of the LiNbO₃ wafers and then sandwiched between them after bonding. The top LiNbO₃ layer is eventually ground and polished down to a thickness of a few micrometers. In order to reduce the roughness and the number of defects that are induced by traditional polishing, chemical mechanical planarization can be used. It is reported that chemical additives like oxidizers and complexing agents can significantly improve the material removal rate and the surface quality[36]. Chemical mechanical planarization therefore is an ideal and sensitive process especially to finish layers of LiNbO₃ that are obtained by more elaborate methods than grinding of a full wafer. Such methods, like crystal ion slicing, use the irradiation with helium ions at a high dose to create a buried layer of modified material inside the LiNbO₃ crystal[37]–[48]. The irradiated wafer is then bonded to another substrate followed by either thermally[38], [48] or chemically[37], [49], [50] induced exfoliation of the LiNbO₃ film[51]. During thermal treatment the temperature is slowly elevated causing the implanted helium ions to agglomerate and form bubbles that induce mechanical stresses and split off the top LiNbO₃

layer. During chemical treatment wet etching with HF selectively removes the sacrificial layer of irradiated LiNbO_3 [25]–[27] resulting in the formation of the LiNbO_3 film[52].

The different approaches to realize thin films of LiNbO_3 through ion beam irradiation can be further distinguished by the method that is used to bond them to the carrier substrate. One way is to use the optically transparent adhesive polymer benzocyclobutene[53] that is employed for transferring several cm^2 of LiNbO_3 thin films with good reproducibility[54], [55]. Before the bonding, the respective substrate can also be coated with a metal layer that can serve as an electrode for electro-optic tuning of the fabricated structures, such as microring resonators[54] or photonic crystal slabs[56]. A drawback of employing benzocyclobutene as an adhesive is that it cannot withstand high temperature annealing which is necessary to remove remaining ion beam induced material modifications to recover the optical properties of the LiNbO_3 crystal. SiO_2 was found to be a temperature stable and suitable substitute to connect the LiNbO_3 film with the substrate[48]. The SiO_2 layer is deposited on the LiNbO_3 substrate by plasma-enhanced chemical vapor deposition which allows precise adjustment of the SiO_2 layer's planar stresses to be matched with the LiNbO_3 substrate. In this way, the so-called lithium-niobate on insulator (LNOI) substrates can be fabricated on the wafer scale[57]–[59] and became commercially available recently from the company NANOLN.

It is common to the methods described until now that they account for the similar thermal expansions of the thin LiNbO_3 film, the adhesive layer and the substrate, which is the reason why other substrates than LiNbO_3 are difficult to implement. A way around this is, for example, silver diffusion bonding of a silver coated silicon target substrate and a silver coated LiNbO_3 thin film carrier substrate[40]. In yet another approach for the realization of LiNbO_3 membranes no layer transfer between substrates is necessary. The monolithic process relies on IBEE where small volumes of helium ion beam irradiated LiNbO_3 are selectively removed by wet etching. In contrast to the previously described processes with the LiNbO_3 thin films having thicknesses of several micrometer, the irradiation here is carried out at lower ion energies and at low temperature (100 K) which avoids the formation of helium bubbles and destructive blistering of the sample surfaces[27], [52]. Using this process, ultrathin membranes of thicknesses down to 190 nm have been realized[52] without any additional polishing. The process was also used for the fabrication of freely suspended photonic crystal membranes in LiNbO_3 [60].

It can be summarized that a number of different approaches can enable the fabrication of membrane substrates from LiNbO_3 . A review of several planar patterning technologies that are available for laterally structuring these substrates is following.

Micro patterning of LiNbO_3

An example for large microoptic LiNbO_3 structures that are used for the exploitation of nonlinear optical effects, such as generation of photon pairs by parametric down conversion, are whispering-gallery mode resonators[61], [62]. These resonators are fabricated solely by polishing and have radii down to 1 mm and heights of 0.5 mm yielding quality factors larger than 10^7 . Another mechanical patterning approach uses circular saw dicing. Shallow trenches are cut by the saw blade across the sample surface. The spaces between these trenches form high aspect ratio ridge waveguides[63]–[66]. Although the overall quality of the resulting structures is very good, dicing is limited to a linear cutting motion. Ultra-precision milling processes[67] do not have this restriction and have been successfully applied to realize bent ridge waveguides in LiNbO_3 [68]. While the ridge confines the light in the horizontal direction in the given examples, the confinement in the vertical is done by either a membrane substrate or a diffusion waveguide. Besides the mechanical patterning, laser ablation also is a suitable tool for machining LiNbO_3 on the micrometer scale. The focused lasers employed for the patterning can be adjusted to structure the sample surfaces, e.g. with trenches[69], hexagonal hole patterns[70] or microdisk resonators[71], as well as to structure the full sample volume three-dimensionally, e.g. with waveguides[72] or more complex periodic patterns[73].

Diffusion waveguides in LiNbO_3

Since waveguides are an essential element of nonlinear integrated optics, considerable effort was put in the development of low-loss waveguides in LiNbO_3 . The most established techniques use diffusion of titanium[74], [75] or proton exchange[76] resulting in micrometer sized diffusion zones with elevated refractive index that support optical mode fields with dimensions of several micrometer in diameter. Alternative approaches yielding similar kinds of buried waveguides include a broad range of laser[77] and ion beam irradiation[78] mediated process. Although these techniques are reliable and well-developed, the dimensions of the waveguiding structures are too large for a high integration density. Nonetheless, they are frequently used as planar waveguides in combination with many types of surface patterns, like ridge waveguides[65] or photonic crystals[79], when membrane substrates are not available.

Domain engineering of LiNbO₃

In order to facilitate efficient nonlinear optical interactions in LiNbO₃, the interacting waves need to maintain a certain phase relationship. This phase-matching can be achieved through domain engineering of the LiNbO₃ crystal by electric field poling [80]. The polarization of the LiNbO₃ crystal along its z-axis is spatially modulated to achieve quasi-phase-matching through periodic arrangement of the respective domains[81], even complex two-dimensional patterns can be used[82]. Poling of LiNbO₃ is a sophisticated technique that has been studied extensively and is used for many applications which are too wide-ranging to be elaborated on here. The periods of the resulting poling patterns are typically in the order of tens of micrometers for light in the near-infrared wavelengths range. Engineering domains that are significantly smaller may be achieved by intentional overpoling[83] which is generally challenging. Besides electric field poling, other mechanisms can be employed for domain engineering with sub-micrometer feature sizes. These mechanisms include domain inversion induced by energetic electron[84]–[90] or ion[91] beams, calligraphic poling by scanning force microscope[92], domain engineering by ultraviolet direct write metal enhanced redox[93] or by irradiation of a patterned chromium film with intense visible laser light[94]. In contrast to the classical electric field poling, these techniques mostly do not allow the domain inversion through the full wafer and are restricted to the sample surface. Nonetheless, especially when using LiNbO₃ membrane substrates, where the functional LiNbO₃ layer has a thickness of less than a micrometer, this restriction is not prohibitive.

Wet etching of locally modified LiNbO₃

The latter two processes for diffusion waveguides and domain engineering do not intrinsically change the surface topography in a way that would be useful for microstructure technology. However, they introduce a modification into the crystal making it vulnerable to selective wet etching. In this way, ridge waveguides have been realized using adapted titanium indiffusion[95], [96] or proton exchange[23], [24], [97]–[99] processes. Also poled LiNbO₃ can be patterned similarly because the etch rates of positive and negative domain faces along the crystal z-axis are slightly different. Using this etch rate difference, any poling pattern can be transferred into the substrate surface. This was demonstrated down to sub-micrometer patterns[94] with their depth being limited by the depth of the domain .

Focused ion beam milling of LiNbO₃ nanostructures

Aside from these indirect approaches, the LiNbO₃ surface can be patterned using lithography based techniques, too. A large class of structures are directly patterned using focused ion beam (FIB) milling. This kind of patterning is especially interesting for research purposes where the focus is on single structures and where short processing times are required. An example for larger micrometer size patterns are microchannels patterned in LiNbO₃[100]. On a similar length scale, FIB can be used to polish microdisk resonators cut in LNOI substrates by laser writing[71]. Besides these examples, FIB is mostly used for the patterning of various types of photonic crystals in LiNbO₃. This includes plain hexagonal photonic crystals in erbium doped LiNbO₃ for investigating the Purcell effect[101], as well as, in undoped LiNbO₃ for performing optical transmission[56] and scanning near-field optical microscope (SNOM) experiments[102]. In most cases, annealed proton exchanged (APE) waveguides are used as a substrate for the patterning of photonic crystals[103] and photonic crystal waveguides[104]. Additionally, the properties of photonic crystal structures can be combined with the material properties of LiNbO₃. In this way, photonic crystal superprisms are realized and characterized using SNOM[105] which can be tuned electro-optically[79]. The electro-optic effect generally can be used to tune the photonic crystal bandgap[106] while also making use of slow light enhancement[107], [108]. Similarly, one-dimensional photonic crystals are fabricated in ridge waveguides that are made from planar diffusion waveguides[109] or ion-sliced LiNbO₃ films[110], these structures are operated as electro-optic tunable optical filters with slow light enhancement. Furthermore, Fabry-Perot type photonic crystal cavities patterned in diffusion waveguides can be built[111] with the addition of electro-optic tuning[112]. Using the pyroelectric effect, temperature sensors can be fabricated from a photonic crystal cavity[113]. In the same way, acousto-optically tunable photonic crystals[114] are possible as well. A slightly different configuration is not relying on diffusion waveguides. Instead, ion beam irradiation and subsequent etching are used to fabricate a LiNbO₃ slab of several micrometer thickness that acts as a planar waveguide. The resulting LiNbO₃ layer can be patterned by FIB[115]. Also using ion beam irradiation with helium ions, the refractive index of LiNbO₃ can be modified to form buried channel waveguides which can be patterned by FIB at the surface[116]. Yet another configuration uses diced ridge waveguides and FIB milling to pattern photonic crystals on the side walls of the waveguide[117]. Generally, it can be stated that FIB is a versatile tool and allows for the realization of a broad range of devices. Nonetheless, the FIB process is limited mainly by redeposition of sputtered material at the

patterned surfaces causing non-perpendicular sidewalls and affecting the optical properties. In the case of FIB patterned hole patterns, such as photonic crystals, conicity and depth effects have significant influence on the transmission properties[118], [119]. Investigating the shape of the holes cut by FIB in LiNbO_3 [120] and possible improvements for the realization of high aspect ratio structures[121] therefore is of considerable significance.

Dry etching of lithographically patterned LiNbO_3

Although FIB is generally suitable for the fabrication of high quality photonic structures, its applicability for large area patterning is intrinsically limited. Such large area patterns include long ridge or photonic crystal waveguides and other integrated optical components. The more suitable approach to realize these structures in LiNbO_3 is based on optical or electron beam lithography combined with standard dry etching techniques like ion beam etching, reactive ion etching[122]–[125] or inductively coupled plasma reactive ion etching[126]–[128]. Along with studying the general etching behavior, several optical structures were realized. Especially important for integrated optics are basic components like ridge waveguides which can be fabricated by either ion beam etching or reactive ion etching in bulk LiNbO_3 [39], [129]–[132] as well as in LNOI substrates[57]–[59], [133]. Also, more advanced structures such as surface plasmon-polariton waveguides[34] or plasmonic silver- LiNbO_3 coaxial nanostructures[134]–[136] are possible. Further examples for purely dielectric LiNbO_3 patterns include Bragg grating waveguides[137], photonic crystals[138], [139] and microring resonators[140]. The interest in patterning LiNbO_3 on the sub-micrometer scale on large areas is growing, especially along with the convenient LNOI substrates becoming commercially available. Nonetheless, a major disadvantage of dry etching LiNbO_3 is that the resulting sidewalls are strongly inclined and not vertical. Patterns with high aspect ratio elements like densely spaced holes or waveguide ridges cannot be realized. This general limitation can be accounted for by introducing it into the devices design[141].

Ion beam enhanced etching of LiNbO_3

Another lithography based approach that results in perpendicular sidewalls relies on ion beam irradiation and subsequent wet etching[25], [26]. The irradiation is done through a patterned mask and designed to modify the crystal from the surface down to the designed depth. The interaction of ion beam irradiation with LiNbO_3 crystals is experimentally studied extensively[26], [27], [46], [78], [142]–[158]. In contrast to the bulk crystal, irradiated LiNbO_3 has a significantly higher etch rate in HF based etchants. The defect formation and

the etching behavior are well understood. Transferring these findings into patterning functional LiNbO₃ devices results in ridge waveguides[159], freestanding photonic crystal membranes[60], microdisk resonators[160] and gold-LiNbO₃ coaxial nanostructures[161].

LiNbO₃ deposition and growth processes

Besides the deterministic approaches for patterning LiNbO₃ micro- and nanostructures that have been reviewed up to here also a number of deposition and growth processes have been reported. These processes are outside the scope of this work and will be mentioned only briefly. In contrast to splitting or polishing single crystal wafers, LiNbO₃ thin films can be fabricated also by means of common deposition techniques including pulsed laser deposition[102], [162], [163], metalorganic chemical vapor deposition[164], liquid phase epitaxy[165], [166] and sputtering[167]. The resulting films are patterned for waveguiding, photonic crystal and surface acoustic wave applications. Nonetheless, in comparison to the established single crystal thin films, the overall optical quality and especially the crystallinity of the deposited films seemed to be not sufficient. Another well-developed approach for the fabrication of single crystal structures is the chemical synthesis of LiNbO₃ nanoparticles with cross sections of several tens of nanometers and lengths of a few micrometers[168]–[170]. Because their chemical synthesis is an entirely stochastic non-deterministic process, it is not relevant for the kind of patterning which is the focus of this work.

Aim and structure of this thesis

Upon reviewing the current state of knowledge for patterning micro- and nanostructured LiNbO₃ optical elements, it can be concluded that a broad range of techniques is available. It is the general aim of this work to realize nonlinear interactions in LiNbO₃ on the micrometer scale. The efficiency of these interaction processes can be significantly enhanced by a confinement of the optical fields to waveguide or resonator modes. The designed functionalities of the respective optical elements depend strongly on the specific sample layout and can be implemented only with a sophisticated microstructure technology. This work, therefore, needs to contribute to the advancement and development of existing patterning approaches and their application to the realization of microstructured waveguides and resonators with nonlinear optical functionalities. While IBEE has been extensively studied before with the focus mainly on the material modification processes[27], in this work the full potential of IBEE is explored by applying it to the realization of advanced optical structures such as photonic crystals. At the same time, this work also accounts for the recently

established LNOI substrates by investigating a modified IBEE process which is based on KOH instead of HF. In this regard, the etching behavior of ion beam irradiated LiNbO₃ in different hydroxide solutions (KOH, NaOH, CsOH, and RbOH) is studied for a broad range of experimental conditions. Substituting HF by KOH makes LNOI substrates fully compatible with IBEE because KOH does not etch the SiO₂ layer sandwiched between the top LiNbO₃ layer and the LiNbO₃ substrate. In contrast to other patterning approaches, IBEE can be used to etch large area patterns into the LiNbO₃ surface with high aspect ratio because of the characteristically perpendicular side walls. Contrary to the commonly used FIB direct patterning of photonic structures which is restricted to small areas, in this work IBEE is used in combination with electron beam lithography for large area patterning. In particular, it is used for the realization of nanoscale ridge waveguides and photonic crystal waveguides that are sufficiently long for the observation of propagation effects with a SNOM. Aside from the advantageous properties of IBEE based patterning, the use of FIB for rapid prototyping of single structures is necessary for research purposes. In this work, FIB is used for the patterning of thin LiNbO₃ membranes produced by either IBEE or obtained from LNOI. The formation of the membranes including their underetching and height adjustment by additional planar dry etching is studied. The impact of gallium ion contaminations from the FIB milling, which remain in the substrate and impair the dimensional accuracy of the process, is investigated. It is further studied how this effect needs to be considered to avoid potentially detrimental effects on the crystals' optical properties. In this work, FIB patterning is eventually used for the fabrication of microdisk resonators and photonic crystal resonators. Their linear and nonlinear optical characterization is presented, particularly the resonantly enhanced SHG from a photonic crystal resonator specifically designed for enhanced vertical emission. Particularly the nonlinear characterization of nanoscale waveguides and resonators is enabled only by the investigation of sophisticated patterning technologies.

The results presented in this thesis are part of a number of collaborations between different individuals. The respective contributions include technological, experimental and theoretical input and will be outlined in the following. At first I will address the broad field of microstructure technology. The sample fabrication relies on facilities that are jointly operated and used by the Institute of Applied Physics (IAP) of the Friedrich-Schiller-Universität Jena, the Fraunhofer Institute of Applied Optics and Precision Engineering (IOF) Jena and the Leibnitz Institute of Photonic Technology (IPHT) Jena. Every sample reported in this thesis was fabricated either directly by myself or by technicians of the IAP under my close

supervision. Processes carried out by technicians have been pre-defined by myself. The distribution of basic tasks to technicians guaranteed constant quality and optimum handling times throughout the entire sample fabrication. Further technical support was needed for chemical vapor phase deposition (Andreas Ihring, IPHT) and ion beam irradiation (Patrick Hoffmann, Institute of Solid State Physics, Friedrich-Schiller-Universität Jena). Experiments about hydroxide based IBEE have been carried out by Juliane Brandt under my supervision as part of her Bachelor thesis. I was directly involved in the optical characterization experiments of the fabricated samples. The experiments have been done at setups that were in some instances preexisting at the IAP. The setup for measuring the linear and nonlinear optical properties of nanoscale waveguides was initiated by Rachel Grange and Anton Sergeev (both ETH Zürich). Another more advanced setup used for the same purpose is operated by Sina Saravi. For the characterization of the LiNbO_3 microdisk and photonic crystal waveguide resonators the setup from Carsten Schmidt was used, including contributions from Wei-Kun Chang (NCU Jhongli, Taiwan) and Arstan Bisianov. SNOM measurements were carried out by Severine Diziain. A setup for cross-polarized scattering microscopy and SHG detection was developed, built and used together with Severine Diziain. The theoretical work for this thesis was mostly done by collaborators. I was involved by evaluating and defining general conditions for the feasibility of fabrication and optical characterization of the designed structures. The photonic crystals were designed by Rumen Iliev (Institute of Condensed Matter Theory and Solid State Optics (IFTO), Friedrich-Schiller-Universität Jena), Christoph Etrich (IFTO) and Severine Diziain. Numerical studies of LiNbO_3 nanoscale waveguides were initiated by Alexander Solntsev (Australian National University, Canberra) and advanced by Anton Sergeev and Sina Saravi. Numerical studies of microdisk resonators were initiated by Carsten Schmidt and continued by Severine Diziain. A simulation tool for the IBEE process was initiated by Holger Hartung and further advanced by myself.

Being partner of various collaborations, I contributed to many projects myself mostly through sample fabrication. These projects include investigations about fluorescence excitation of dyes through LiNbO_3 nanowires under the supervision of Rachel Grange and mode analysis of photonic crystal L3 resonators under the supervision of Severine Diziain. I further contributed to projects about domain engineered LiNbO_3 waveguide devices for nonlinear frequency conversion with Yen-Hung Chen (NCU Jhongli, Taiwan). For this collaboration I fabricated and optically characterized small-period Bragg gratings on waveguides. Also, I

designed and simulated optical parametric oscillators composed from periodically poled LiNbO₃ with electro-optic polarization-mode converters.

2 Fundamental concepts and methods

2.1 Properties of lithium niobate

Lithium niobate (LiNbO_3) is the substrate material for various optical components that have been realized as a result of this work. This section therefore provides a brief introduction to the material properties of LiNbO_3 especially in consideration of LiNbO_3 being an optical material. LiNbO_3 is one of the most commonly used crystalline materials with many applications in integrated and nonlinear optics. It is an artificial material that is fabricated using the Czochralski process where a LiNbO_3 seed crystal is pulled out of a melt composed from lithium oxide and niobium pentoxide[5], [7]–[9], [171]. The crystal growth process is technologically well established. Single crystal wafers of up to six inches in diameter are commercially available. Depending on the ratio of both starting materials, the resulting LiNbO_3 is either congruent (ratio $\text{Li/Nb} = 0.96$) or stoichiometric (ratio $\text{Li/Nb} = 1$). Both compositions have just slightly different optical properties. Throughout this work, congruent LiNbO_3 is used exclusively. LiNbO_3 consists of a trigonal crystal lattice without inversion symmetry. In the crystal structure, the position of lithium and niobium ions is along the polar c-axis between layers of oxygen ions. Because of their centrosymmetric alignment, a displacement of lithium and niobium ions is possible only along the c-axis. The direction of the displacement defines the orientation of the spontaneous polarization. As a result, only antiparallel domains along the c-axis can be obtained in LiNbO_3 . LiNbO_3 strongly displays various effects associated with its crystal structure, like the electro-optic effect, pyroelectricity, piezo-electricity and second-order optical nonlinearity[172]. The crystal structure leads to a noticeable anisotropy of these effects. Hence, LiNbO_3 also has a negative uniaxial birefringence with refractive indices of $n_o=2.21$ and $n_e=2.14$ in the near-infrared wavelength range. Compared to most semiconductor materials LiNbO_3 benefits from a large transparency range (350.. 5200 nm). All of these properties combined in a single material along with well-established patterning technologies make LiNbO_3 an important substrate for functional optical devices. The patterning technologies have been outlined in the introduction before and include methods for the realization of low-loss waveguides and gratings of crystal domains with alternated polarity.

2.2 Electromagnetic wave propagation

2.2.1 Basic concepts of nonlinear optics

The aim of this section is the derivation of an equation that relates the efficiency of generated second harmonic in a nonlinear medium to experimental conditions and material parameters. It is outside the scope of this section to provide a comprehensive insight in the broad field of nonlinear optics. During the following concise derivation some of the major concepts being important for general design guidelines and optical characterization of the tested structures will be introduced.

The propagation of electromagnetic waves can be fully described by the Maxwell equations[173]. Assuming the material is non-magnetic and external charges are absent, the Maxwell equations in frequency space can be simplified to the form

$$\begin{aligned} \text{rot}\tilde{\mathbf{E}}(\mathbf{r}, \omega) &= -i\omega\mu_0\tilde{\mathbf{H}}(\mathbf{r}, \omega), \\ \text{rot}\tilde{\mathbf{H}}(\mathbf{r}, \omega) &= -i\omega\varepsilon_0\tilde{\mathbf{E}}(\mathbf{r}, \omega) - i\omega\tilde{\mathbf{P}}(\mathbf{r}, \omega), \\ \varepsilon_0\text{div}\tilde{\mathbf{E}}(\mathbf{r}, \omega) &= -\text{div}\tilde{\mathbf{P}}(\mathbf{r}, \omega), \\ \text{div}\tilde{\mathbf{H}}(\mathbf{r}, \omega) &= 0. \end{aligned} \quad (1)$$

$\tilde{\mathbf{E}}(\mathbf{r}, \omega)$ is the electric field vector, $\tilde{\mathbf{H}}(\mathbf{r}, \omega)$ the magnetic field vector, $\tilde{\mathbf{P}}(\mathbf{r}, \omega)$ the polarization vector, ε_0 the dielectric constant for vacuum, μ_0 the magnetic permeability of vacuum, \mathbf{r} the spatial coordinate vector, ω the angular frequency of the field.

Taking the curl of the first equation in (1) and inserting the second equation, the wave equation can be derived as

$$\text{rot rot}\tilde{\mathbf{E}}(\mathbf{r}, \omega) - \omega^2\varepsilon_0\mu_0\tilde{\mathbf{E}}(\mathbf{r}, \omega) = \mu_0\omega^2\tilde{\mathbf{P}}(\mathbf{r}, \omega). \quad (2)$$

The response of a dielectric material to an electric field $\tilde{\mathbf{E}}(\mathbf{r}, \omega)$ is described by the polarization $\tilde{\mathbf{P}}(\mathbf{r}, \omega)$, which can be expanded in a series of ascending powers of the electric field[174]

$$\tilde{\mathbf{P}}(\mathbf{r}, \omega) = \sum_{n=1}^{\infty} \tilde{\mathbf{P}}^{(n)}(\mathbf{r}, \omega).$$

The components of $\tilde{\mathbf{P}}^{(n)}(\mathbf{r}, \omega)$ are expressed as

$$\tilde{\mathbf{P}}_i^{(n)}(\mathbf{r}, \omega) = \varepsilon_0 \sum_{\eta_1 \dots \eta_n} \int_{-\infty}^{+\infty} d\omega_1 \dots \int_{-\infty}^{+\infty} d\omega_n \chi_{i\eta_1 \dots \eta_n}^{(n)}(\mathbf{r}, -\omega_\sigma; \omega_1, \dots, \omega_n) \tilde{\mathbf{E}}_{\eta_1}(\mathbf{r}, \omega_1) \dots \tilde{\mathbf{E}}_{\eta_n}(\mathbf{r}, \omega_n) \delta(\omega - \omega_\sigma) \quad (3)$$

with a summation of all $\eta_1 \dots \eta_n$ over x , y and z [174]. The frequencies of the interacting electric fields need to fulfill

$$\omega = \omega_\sigma = \sum_{j=1}^n \omega_j$$

in order to comply with the requirement of energy conservation. ω_σ is the frequency of a polarization field induced by the interaction of the individual electric field components. This interaction between the material and the electric fields is described by the materials n th-order susceptibility tensor $\chi_{i\eta_1\dots\eta_n}^{(n)}(\mathbf{r}, -\omega_\sigma; \omega_1, \dots, \omega_n)$ which accounts for different optical effects. The effects of linear optics are described through $\tilde{\mathbf{P}}^{\text{linear}}(\mathbf{r}, \omega) = \epsilon_0 \chi^{(1)}(\mathbf{r}, -\omega; \omega) \tilde{\mathbf{E}}(\mathbf{r}, \omega)$, where the first-order, linear susceptibility is related to the more commonly used dielectric function through $\epsilon(\mathbf{r}, \omega) = 1 + \chi^{(1)}(\mathbf{r}, -\omega; \omega)$. Amongst the various higher order effects, only effects of second order are relevant for this work. Particularly interesting is the generation of a second harmonic (SH) frequency ω_{SH} from a fundamental harmonic (FH) field with frequency $\omega_{\text{FH}} = \frac{1}{2} \omega_{\text{SH}}$. The $\chi^{(2)}$ tensor in (3) describes the interaction of three electric field components. In the case of degenerate SHG, two of these components belong to the same field. The description of the induced polarization $\tilde{\mathbf{P}}^{\text{nonlinear}} \sim \epsilon_0 \chi^{(2)} \tilde{\mathbf{E}}^2$ is further simplified by assuming that the nonlinear medium is nondispersive, homogenous and isotropic. Furthermore, linearly polarized optical fields are assumed such that the tensor nature of $\chi^{(2)}$ can be omitted and is replaced by the quantity $d = \frac{1}{2} \chi^{(2)}$. The complete optical field can be expressed as a superposition of SH and FH plane waves

$$E(z, t) = \sum_{m=\text{SH, FH}} \frac{1}{2} [E_m(z) \exp(i\omega_m t - ik_m z) + \text{c.c.}] \quad (4)$$

propagating in z direction with field amplitudes $E_{\text{SH, FH}}(z)$. Assuming slowly varying envelopes[174]

$$\frac{dE_{\text{SH, FH}}(z)}{dz} k_{\text{SH, FH}} \gg \frac{d^2 E_{\text{SH, FH}}(z)}{dz^2} \quad (5)$$

and using the wave equation (2) with (4), the following set of coupled wave equations can be derived

$$\begin{aligned} \frac{dE_{\text{FH}}(z)}{dz} &= -i\omega_{\text{FH}} \sqrt{\frac{\mu_0}{\epsilon_{\text{FH}}}} d E_{\text{SH}}(z) E_{\text{FH}}^*(z) \exp(-i(k_{\text{SH}} - 2k_{\text{FH}})z) \\ \frac{dE_{\text{SH}}(z)}{dz} &= -i\omega_{\text{SH}} \sqrt{\frac{\mu_0}{\epsilon_{\text{SH}}}} d E_{\text{FH}}(z) E_{\text{FH}}(z) \exp(-i(2k_{\text{FH}} - k_{\text{SH}})z). \end{aligned} \quad (6)$$

This set of equations shows how the electric fields for FH and SH are coupled through the nonlinear polarization represented by the nonlinearity d . It will be used to discuss the basic properties of SH generation. A further simplification is introduced by assuming that the medium is lossless and that the conversion efficiency of the SHG is rather weak, which is

valid throughout this work. It allows the assumption $dE_{\text{FH}}/dz \approx 0$ implying that the power of the FH field does not change significantly by either linear losses or conversion to the SH field. Integration of equations (6) then results in an SH amplitude at the output of the nonlinear medium assuming $E_{\text{SH}}(z=0) = 0$

$$E_{\text{SH}}(z=L) = -i\omega_{\text{FH}} 2\sqrt{\frac{\mu_0}{\varepsilon}} d E_{\text{FH}}^2(L) \frac{\exp(i\Delta k L) - 1}{i\Delta k} \quad \text{with } \Delta k = k_{\text{SH}} - 2k_{\text{FH}}. \quad (7)$$

In order to derive an expression for the SH conversion efficiency, the SH intensity at $z=L$ is used

$$\frac{P_{\text{SH}}}{\text{area}} = \frac{1}{2} \sqrt{\frac{\varepsilon}{\mu_0}} E_{\text{SH}}(L) E_{\text{SH}}^*(L). \quad (8)$$

The SH conversion efficiency can now be written as

$$\frac{P_{\text{SH}}}{P_{\text{FH}}} = 8 \left(\frac{\mu_0}{\varepsilon} \right) \frac{\omega_{\text{FH}}^2 d^2 L^2}{n^3} \left(\frac{P_{\text{FH}}}{\text{area}} \right) \text{sinc}^2 \left(\frac{\Delta k L}{2} \right) \quad \text{with } \varepsilon_{\text{FH}} \approx \varepsilon_{\text{SH}} \approx \varepsilon_0 n^2. \quad (9)$$

In the following, this expression will be used to discuss concepts that increase the efficiency of SHG. This discussion assumes that the nonlinear medium is always the same, i.e. LiNbO₃, and that the material coefficients are fixed.

A tuning parameter that is easily accessible in the experiment is the FH power P_{FH} at the input of the nonlinear medium. The FH power is initially limited by the laser system used in the experiment. One way to increase it further is using the field enhancement in any kind of resonator. In such systems the intracavity power can be much larger than the initial input power. Therefore, the efficiency of nonlinear frequency conversion processes taking place in nonlinear media that are located inside a resonator can be greatly enhanced. Following this concept, microstructured resonators in different configurations have been realized in LiNbO₃ which will be discussed in chapter 5. Another tuning parameter is the interaction length L that should be as large as possible. It is usually limited by the size of the nonlinear crystal or by the design of the optical element. From this point of view resonators are again beneficial because the numerous roundtrips taken inside a cavity effectively extend the interaction length and increase the power stored in the cavity. According to (9) it can further be concluded that the area illuminated by the FH input should be small for maximized conversion efficiency. A very important implementation of this requirement are waveguides. They confine light over long distances while maintaining a small cross sectional area. Especially the realization of nanoscale waveguides in LiNbO₃ represents a key result of this work and will be explained in chapter 4.

Returning again to (9) one more prerequisite for high efficiency SHG, being $\Delta k = 0$, can be identified. It implies that SH waves generated at different positions along their propagating through the nonlinear medium must be in phase. If $\Delta k \neq 0$ the SH waves are out of phase because they are emanating from different spatial positions. The resulting interference is accounted for by the sinc^2 function in (9). This factor is used to define the so-called coherence length $L_c = 2\pi/\Delta k$ representing a measure of the maximum length in which SH can be efficiently generated. To fulfill the phase-matching condition $\Delta k = 0$, a number of mechanisms exist including birefringence, modal phase-matching and quasi-phase-matching. For this work, just the latter two are important.

2.2.2 Waveguides and modal phase-matching

Electromagnetic waves can be guided in any transparent medium when the interfaces of the medium transverse to the propagation direction are reflective. To provide long propagation distances of the guided light, this reflectivity should be maximal, which is typically realized by total internal reflection. A waveguide can be any arrangement of dielectric media that is guiding along z because of its specific refractive index distribution $n(x, y)$. The guided light is characterized by its field distribution in the cross-sectional area of the waveguide propagating along the waveguide $\mathbf{E}(x, y, z) = \mathbf{E}_0(x, y) \exp(i(\beta z - \omega t))$, where β is the propagation constant[28]. The modal field distributions and their respective propagation constants are obtained mostly numerically from $n(x, y)$. Usually, small cross-sectional areas of a waveguide result in a strong confinement and, hence, higher field intensity of the respective mode that can be used to increase the efficiency of the SHG. For high nonlinear efficiencies the cross-sectional area should ideally be in the order of the wavelength of the light that is guided. If it is smaller and assuming a low-refractive index cladding, the field would be localized mostly outside the waveguide, where it does not contribute to the SHG. In waveguides with sufficiently small cross-sections modal phase-matching can be accomplished by taking advantage of the modal dispersion of the waveguide modes[31], [175]. In the case of SHG in LiNbO_3 the refractive index increases when doubling the frequency. This is why the effective indices of the fundamental waveguide modes of SH and FH are always different, hence, not phase-matched. Modal phase-matching is therefore realized with the lowest order waveguide mode of the FH and a higher order waveguide mode of the SH. Furthermore, it must be ensured that the interacting modes have a matching symmetry, otherwise the overlap between FH and SH vanishes. In contrast to other phase-matching techniques used for

waveguides, this approach is fairly simple to realize technologically and, additionally, is very suitable for monolithic integration schemes. On the other hand, the SH conversion efficiency might be affected because of the small overlap of the interacting modes as well as the larger propagation losses of the higher order modes[176].

2.2.3 Optical resonators – figures of merit

An optical resonator is a device that is characterized by a resonance frequency for electromagnetic waves where it oscillates with larger amplitude than at other frequencies. The quality factor $Q = \omega W/P$ of a resonator is a measure to quantify the ratio of the energy W inside the cavity to the power P dissipated by the resonator at a resonance frequency ω . The Q factor can also be understood as a measure for the photon lifetime τ inside the resonator and can be written as

$$Q = \omega\tau = \frac{\omega}{\Delta\omega} = \frac{\lambda}{\Delta\lambda}, \quad (10)$$

where ω and λ are the resonance frequency and wavelength divided by their respective resonance widths[28]. A typical Q factor for photonic crystal resonators fabricated in semiconductors with high refractive index can be as high as 10^7 for a silicon heterostructure nanocavity[177]. In order to confine light and use resonant structures for the enhancement of nonlinear interaction processes, high Q factors are usually wanted. At the same time a compromise has to be made because high quality factor also means long photon lifetime and, hence, limited bandwidths in case of pulsed beam interaction. In the case of SHG in a resonant structure, the interacting fields at frequencies ω_{FH} and $\omega_{\text{SH}}=2\omega_{\text{FH}}$ will be enhanced proportional to the Q factors at their respective frequencies. In the case of perfectly overlapping spatial mode profiles the enhancement factor amounts to $Q_{\text{FH}}^2 Q_{\text{SH}}$.

2.2.4 Photonic band gap structures

In the past decades a remarkable technological development of the facilities for semiconductor micro and nanofabrication took place. A similar trend of miniaturization based on these well-established tools is anticipated for the field of integrated optics. Functional macroscopic optical elements could be transformed into highly integrated on-chip devices. A well-known platform for the implementation of the intended high integration densities are planar photonic crystals that will be the focus of this section.

Photonic crystals are dielectric structures composed from a periodic arrangement of materials with different refractive indices that can be designed to modify the propagation of electromagnetic waves in many ways[178]. Considering a structure that is periodic in one dimension, a propagating electromagnetic wave will be partially reflected and transmitted at each interface. The phases of the interacting waves originating from the successive surfaces interfere and eventually determine the response of the full structure. Using the Floquet-Bloch analysis it can be proved that waves can propagate through periodic media without effective scattering. The formalism can be applied to conveniently rewrite Maxwells equations as an eigenproblem [179]

$$\nabla \times \frac{1}{\varepsilon(\mathbf{r})} \nabla \times \mathbf{H}(\mathbf{r}) = \left(\frac{\omega}{c} \right)^2 \mathbf{H}(\mathbf{r}), \quad (11)$$

with eigenvalue $\left(\frac{\omega}{c} \right)^2$ and eigenoperator $\nabla \times \frac{1}{\varepsilon(\mathbf{r})} \nabla \times$.

The dielectric function representing the photonic crystal $\varepsilon(\mathbf{r}) = \varepsilon(\mathbf{r} + \mathbf{R})$ is assumed to be periodic for certain lattice vectors \mathbf{R} . According to the Floquet-Bloch approach, periodic eigenproblems such as (11) have solutions of the form $\mathbf{H}(\mathbf{r}) = \exp(i\mathbf{k} \cdot \mathbf{r}) \mathbf{H}_{n,\mathbf{k}}(\mathbf{r})$ with eigenvalues $\omega_n(\mathbf{k})$ and with $\mathbf{H}_{n,\mathbf{k}}(\mathbf{r})$ being a periodic envelope function. Consequently, (11) can be rewritten as

$$(\nabla + i\mathbf{k}) \times \frac{1}{\varepsilon(\mathbf{r})} (\nabla + i\mathbf{k}) \times \mathbf{H}_{n,\mathbf{k}}(\mathbf{r}) = \left(\frac{\omega_n(\mathbf{k})}{c} \right)^2 \mathbf{H}_{n,\mathbf{k}}(\mathbf{r}). \quad (12)$$

Because the primitive cell is finite for periodic structures, n discrete eigenvalues $\omega_n(\mathbf{k})$ being continuous functions of \mathbf{k} exist that are forming discrete bands in the dispersion plot. This plot, also known as band diagram, includes all possible modes inside the periodic structure. Of practical importance are photonic crystal structures that exhibit a complete photonic band gap, meaning a frequency range where no propagating modes exist for any \mathbf{k} with adjacent propagating modes existing below and above the gap. Rigorous criteria for the existence of a band gap in structures that are periodic in two or three dimensions have not yet been identified. Computational treatment of these structures is therefore inevitable and usually the basis of any experimental investigation of photonic crystals.

Exclusively relevant for this work are two-dimensional periodic patterns. Amongst the many kinds of possible arrangements very commonly used is the hexagonal hole lattice[178]. Depending on the refractive index difference and the ratio of hole diameter and period of the hexagonal lattice it is possible to design a structure that has a complete photonic band gap for transverse electric (TE) and transverse magnetic (TM) polarization. In order to realize

efficient interaction of incident light and this planar photonic crystal structure, the light needs to be guided in this plane. This is accomplished by introducing a slab waveguide where the slab containing the photonic crystal has a larger refractive index than the adjacent layers. By introducing the slab, just the in-plane wave vector $\mathbf{k}_{\parallel} = (k_x, k_y)$ remains a conserved quantity whereas k_z being the vertical wave vector is not conserved. Plotting the projected band diagram ω versus \mathbf{k}_{\parallel} the continuous light line $\omega \geq c|\mathbf{k}_{\parallel}|$ can be identified. In the picture of geometrical optics, wave vectors with frequencies above the light line correspond to incidence angles that are too large to allow for guiding by total internal reflection. The respective modes couple to radiative modes in the substrate which leads to increased losses. Our investigations focus on LiNbO_3 being a substrate material with relatively low refractive index. A slab consisting of LiNbO_3 deposited on a silica cladding or made by standard LiNbO_3 waveguide technologies will suffer from weak confinement because of the small refractive index difference. The resulting modal fields will consequently extend into the substrate causing radiative losses[180]. The weak confinement also pulls the photonic bands towards and above the light line that represents the limiting condition for waveguiding in the slab. The objective of this work therefore is to maximize the refractive index difference between the slab and the surrounding material by suspending the photonic crystal slab in air.

In order to confine light not just vertically by the slab but also horizontally, the planar hexagonal photonic crystal structure cannot be used unperturbed. Instead, defects need to be introduced for example by omitting a single hole in the lattice. These defects give rise to modes with frequencies situated in the photonic band gap of the unperturbed lattice[178]. Modes of this kind cannot propagate through the lattice and are reflected. Therefore, such point defects form optical resonators for frequencies inside the photonic band gap. The continuation of introducing defects yields structures with entire rows of holes being omitted. The resulting photonic crystal waveguide confines light horizontally through the photonic band gap and vertically through total internal reflection in the slab. This concept has been used for LiNbO_3 photonic crystals and realizations in LiNbO_3 will be presented later in this work.

As already indicated above, numerical modelling plays a major role in photonic crystal research. It is used to design large varieties of photonic crystal structures that confine, guide and manipulate light in many ways. Using the appropriate fabrication technology offers almost endless possibilities to ultimately realize the resulting structures for experimental characterization. Hence, there is a large freedom in the design process. The design is usually

obtained from a computational treatment of the system. From the broad field of computational photonics several numerical methods are known that allow for quantitative theoretical predictions of the final photonic crystal's optical properties. Relevant for this work is the finite-difference time-domain (FDTD) method to simulate the full time-dependent Maxwell equations[181]. It discretizes space and time into a grid of points with the partial derivatives being approximated by finite differences. The resulting equations are calculated in every point on the grid from the respective preceding point in time. In this way, the spatial and temporal evolution of all components of electric and magnetic fields can be evaluated.

2.3 Fabrication of micro and nanostructured lithium niobate

This section briefly introduces commonly used micro and nanostructure technologies that are relevant for this work or might become relevant when discussing future developments. The following summary is restricted to planar deterministic approaches representing mostly state of the art technologies used in the modern semiconductor industry. This intentionally incomplete overview can be supplemented by further literature giving a comprehensive overview about micro and nanostructure fabrication technologies.

2.3.1 Lithography

In general, lithography is a printing technique for pattern generation into or onto a medium which must be sensitive to the respective interaction mechanism. In terms of microstructure technology, these mechanisms are distinguished by their physical origin in photon-, electron- and ion beam mediated lithography. The medium usually used for recording is mostly a polymeric resist that changes its chemical properties after irradiation with any of these beams and, as a consequence, can be dissolved in a developer solution subsequently. Such a behavior is characteristic for positive resists. Negative resists behaving in the opposite way are also frequently used.

Electron beam lithography

Electron beam lithography (EBL) uses a beam of electrons that is scanned across a resist coated surface. Being a maskless process the respective pattern is directly written with the scanning electron beam[182]. Depending on the shape of the beam cross-section, EBL can be categorized into systems using a fixed-shape beam (mostly Gaussian) or a variable-shape

beam defined by an aperture that can take almost any form[183]. Maybe the most important characteristic of EBL is the nanoscale resolution[184], which along with the serial direct writing scheme may also become a restriction by limiting the size of patterned areas. EBL therefore is no means to facilitate mass production of patterned surfaces. Instead, it is advantageously used for prototyping of designs or mask preparation for pattern replication via optical lithography. In the research of micro and nanostructured optics, EBL is routinely used because it offers the largest flexibility of the patterning.

Optical lithography

Optical lithography (OL) uses light to replicate micro and nanoscale patterns from a photomask to a photosensitive resist[185]. The wavelengths used for exposure in combination with the respective optical projection system determines the resolution of OL. For example, using extreme ultraviolet light sources, the resolution can be well below 100 nm[186]. In the context of microoptic research, OL is commonly used for recurring patterning tasks on the micrometer scale. This is because of the relatively low resolution and because any pattern requires a specific photomask making the process slow and inflexible, at first.

Ion beam lithography

Ion beam lithography is a general term describing the direct patterning of a surface by means of charged and energized particles similar to EBL[187], [188]. Most commonly, a focused ion beam (FIB) of gallium ions is used to locally remove material. Throughout this work, the term FIB always refers to a gallium ion device. The etching process is based on the physical interaction of the accelerated chemically inert gallium ions and the substrate. Therefore, the substrate can be composed from any kind of solid material. It is directly patterned with a resolution of down to 10 nm and does not need an additional development step[189]. The areas that can be structured by FIB are in the order of $100 \times 100 \mu\text{m}^2$, which is relatively small and not compatible with mass-production. FIB patterning is, on the other hand, ideally suited for research purposes, where the focus is often just on single structures or design ideas that greatly benefit from fast turn-around times of the samples. On the contrary, FIB patterning of optical structures such as photonic crystals in dielectric substrates or plasmonic structures in metal films might decrease their functionality because of the inevitable deposition of gallium ions in the patterned surfaces[190]. This problem can be reduced by an alternative technological approach that uses helium ions instead of gallium, which increases the resolution below 1 nm but decreases the sputtering yield by around two orders of

magnitude compared to FIB[191]. Helium ion microscopes (HIM) are nonetheless used for direct write lithography [192] and, more successfully, for resist based lithography in hydrogen silsesquioxane[193] that outperforms EBL in terms of resolution and proximity-effect.

2.3.2 Thin film deposition

Thin film deposition in this work is mainly used to prepare resist layers for lithography or for layers used as hard masks to pattern the underlying LiNbO_3 substrate. The thin films represent an important intermediate step in the respective process chains. However, their deposition is done by means of certain well-established standard technologies which shall justify the brief nature of the following explanations and the exclusion of methods irrelevant for this work.

In general terms, the deposition of a thin film can originate from a liquid or gaseous phase. A liquid phase deposition method, that is relevant here, is spin coating where a small amount of liquid is dropped on a rotating substrate. The resulting uniformly thick layer is subsequently treated to harden forming a solid film. In the case of spin coating of resist for lithography applications this treatment would be a baking step.

Gas phase deposition can be distinguished according to the underlying mechanism into physically and chemically assisted techniques. It is common to all physical vapor deposition techniques that a solid target material is brought into the gaseous phase by a physical interaction process[194]. This could be high temperatures in the case of electron-beam and thermal evaporation or the irradiation with energetic particles in the case of sputtering or ion-assisted deposition. The resulting vapor condenses at the substrate surface forming a closed film. The mostly inhomogeneous emission profiles of such sources are compensated by rotating the substrate, which increases the uniformity of the film thickness. These physical vapor deposition techniques work for a broad range of materials. In this work, they are typically used to deposit carbon and metal films used as etching masks or as conductive layers during particle beam imaging (SEM, FIB, EBL).

Chemical vapor deposition (CVD) techniques use a chemical reaction to create a solid film from a gas state[195]. The dissociation of the molecules of the reaction gases is typically enabled by heating the substrates. Especially for temperature sensitive materials, such as LiNbO_3 , the CVD process can be enhanced by a plasma (PECVD) as an additional energy source to keep the substrate temperature low. CVD results in very homogeneous films covering also patterned and uneven surfaces. Throughout this work, all SiO_2 and SiN films are from PECVD. The films are used as hardmasks for subsequent etching steps or for surface

and edge protection during mechanical polishing. Another type of CVD often complements FIB applications: A precursor gas, specific to the material that has to be deposited, is injected in the scanning field of a focused ion or electron beam[196]. The gas will be dissociated and material is deposited at the beam position. Because the gas can be injected locally at the beam position, this process can be used as a lithography system. In this work, platinum is used in FIB for cross-section preparation as cover layer or as an adhesive for microscale sample manipulation.

2.3.3 Pattern transfer methods

Methods for the transfer of any lithographically defined resist pattern into another substrate or functional layer can be divided into subtractive and additive approaches[197]. The most important example for additive transfer is the lift-off technique: A functional material is deposited on a sacrificial resist pattern covering the resist at the top and the substrate through the openings in that pattern. After the removal of the resist in a solvent, the inverse pattern composed from the target material remains on the substrate. This process is limited in many ways which is why subtractive patterning, in most cases removal by etching, is of larger practical importance. Generally, it can be distinguished between dry and wet etching. Given that the substrate is unmodified and isotropic, a liquid etchant will remove the substrate surface without directionality causing a lateral underetching of the masking layer. Dry etching techniques are more advantageous in this context because they allow precise control of the directionality of the etching and therefore enable high aspect ratio patterns with high lateral resolution. Various technological realization schemes exist[198], three of the most important examples will be described here. Ion beam etching (IBE) uses energetic inert ions, usually argon, to physically remove material, similar to sputtering without the recollection of removed material. IBE has a high etch rate, good directionality but small material selectivity[199]. When a reactive gas is added to the inert gas (reactive ion beam etching, RIBE) or used instead (reactive ion etching, RIE), the material selectivity of the etching along with the respective etch rate is improved by an additional chemical reaction taking place at the substrate surface. A modification to the RIE process uses an inductively coupled plasma (ICP) to create energetic ions. The etching conditions in the ICP-RIE can be broadly tuned by alteration of the many process parameters making ICP-RIE a very versatile tool. Throughout this work, any of these etching techniques have been used for the patterning of LiNbO_3 , SiO_2 , SiN and Cr .

2.3.4 Ion beam enhanced etching

Ion beam enhanced etching (IBEE) is a directional wet etching process where an anisotropy is introduced by ion beam irradiation. It was developed for structuring LiNbO₃ on the nano and micrometer scale. The description of this method has been excluded from the preceding section because it is an essential part of this work and, therefore, requires a more elaborate treatment.

Ion solid interaction

High energy ions interacting with the lattice of a crystalline solid are causing a broad range of effects. Generally, the ion will transfer its kinetic energy to the lattice atoms. It can be distinguished between nuclear and electronic energy loss, which are the dominating effects amongst others. The nuclear energy loss is caused by elastic scattering of the energetic ions at atomic nuclei and introduces point defects such as displacements or vacancies in the crystal lattice. Depending on the energy of the ion, this defect formation extensively cascades until the ion stops. The electronic energy loss, on the other hand, results from inelastic interaction with the target atoms which leads to ionization or excitation of the atoms. The mass and energy of the ions that are used for irradiation defines whether the nuclear or the electronic energy loss is dominant. Although both effects are suitable for patterning LiNbO₃[145], this work relies on the nuclear energy loss. It modifies the crystal structure of LiNbO₃ in a way that its resistance against chemical wet etching is significantly reduced[25], [200].

The defect formation in the target substrate induced by the ion beam irradiation depends on many parameters, such as ion energy, ion species, target material and temperature. It is a statistical process that includes a large number of interaction events which can be partially understood by means of computational physics. A well-established simulation tool that serves this purpose is SRIM (Stopping and Range of Ions in Matter)[201]. It is based on a Monte Carlo simulation method of the binary collision approximation where the distance to and the impact parameter of the next interacting ion is selected randomly for a probability distribution that depends on the atomic density of the target. With the SRIM tool 3D distributions of displacements in the target material are calculated that will be used throughout this work.

To quantify the displacement distribution the normalized fluence can be introduced as

$$n_{\text{dpa}} = \frac{N_{\text{displ}} N_{\text{I}}}{N_0}. \quad (13)$$

N_{displ} is the number of displacements per atom per irradiated ion and depth interval, it can be deduced from the SRIM simulation. N_1 is the ion fluence defined as number of irradiated ions per area. N_0 is the atomic density (LiNbO_3 $N_0 = 9.457 \cdot 10^{22} \text{ cm}^{-3}$). The normalized fluence n_{dpa} is given in units of dpa (displacements per atom). It is important to note that n_{dpa} is obtained from a simulation that does not take all experimental conditions into account, especially temperature related effects such as thermal annealing during the irradiation.

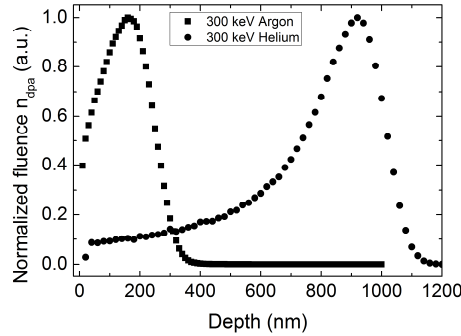


Figure 1: Simulated depth distribution of the normalized fluence for the irradiation of LiNbO_3 with argon and helium ions with an energy of 300 keV.

The relation between the simulated n_{dpa} and the actual defect concentration n_{da} (number of displaced atoms) was obtained experimentally for the irradiation conditions that are relevant for this work[202]. To illustrate the impact of energy and ion species on the depth distribution of displacements a simulation of n_{dpa} was done for a typical irradiation of LiNbO_3 with argon and helium ions with an energy of 300 keV (see Figure 1). Because both ion species have different masses at the same energy, their scattering cross-section is different which leads to different penetration depths. The lighter helium ions penetrate significantly deeper than the heavier argon ions.

Etching of ion beam irradiated LiNbO_3

LiNbO_3 is chemically very stable and therefore difficult to process in microstructure technology. The etch rate of pristine LiNbO_3 in concentrated HF (40%) is negligible[27]. In order to make LiNbO_3 vulnerable to wet etching in diluted HF (4%) the IBEE process uses ion beam irradiation to damage the crystal structure. A comprehensive investigation about this HF based etching process has been done before[150]. The findings presented in reference [150] will be used throughout this work. The main result is the dependence of the etch rate on the normalized fluence. It was found that no etching occurred below 0.15 dpa. In the range of 0.15 to 0.4 dpa the etch rate rapidly increases and saturates at the maximum value for fluences

above 0.4 dpa. Typical values for an etch rate in the saturation region is around 120 nm/min for LiNbO₃ etched in HF (4%) at 40°C. The wet etching step of IBEE does not require precise control of the process parameters because the process is self-limited by the shape of the damaged area in the crystal.

Surface patterning of LiNbO₃

The lateral patterning starts with the fabrication of an irradiation mask which is composed of a SiO₂ layer and a chromium layer. At first, the chromium layer is patterned by EBL and dry etching. Subsequently, it is used as a mask for dry etching the SiO₂. The mask material and their thicknesses are chosen to block the ion beam irradiation that is used to damage the unmasked regions[60]. The irradiation conditions must be adjusted to result in a homogeneous material damage starting from the surface of the LiNbO₃ down to the designed depth. This is typically realized by a series of argon ion irradiations with different energies and fluences. Figure 2 shows the calculated normalized fluence for an argon ion irradiation with energies of 60, 150, 350 and 600 keV and fluences of $2.3 \cdot 10^{14}$, $2.3 \cdot 10^{14}$, $2.3 \cdot 10^{14}$ and $1.2 \cdot 10^{15}$ cm⁻².

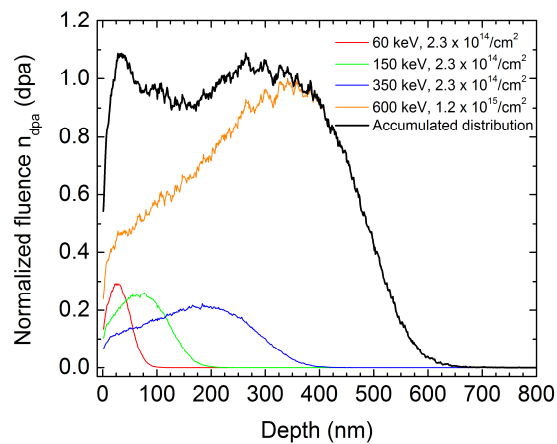


Figure 2: Simulated depth distribution of the normalized fluence for a series of argon ion irradiations. The accumulated depth distribution shows the formation of a homogeneously damaged layer.

The accumulated displacement is mostly homogeneous down to a depth of 550 nm at a value of 0.2 dpa. 0.2 dpa is the threshold value for HF wet etching and defines the final depth of the pattern[150]. Before any further processing of the irradiated sample, the mask has to be removed. If just a surface patterning is required, the final wet etching follows immediately. If a patterned membrane is required, another ion beam irradiation follows before the etching.

Patterning of a LiNbO₃ membrane

In order to realize a freestanding patterned LiNbO₃ membrane, the lateral patterning is followed by a helium ion irradiation that defines the geometry of the air gap underneath the patterned LiNbO₃ surface layer[52] upon the final wet etching. The irradiation conditions result in a displacement distribution located below the surface where it connects to the previously irradiated areas. The position and width of this distribution can be precisely adjusted by tuning the energy and the fluence of the ions. The helium ion irradiation is performed at a temperature of 100 K to avoid the agglomeration of bubbles that could expand inside the substrate and mechanically destroy the surface[38], [46], [52]. In addition, the membrane formation can be controlled precisely by thermal annealing (30 min at 300°C) between the helium ion irradiation and the final etching step. The annealing causes the shape of the displacement distribution to become narrower. While the peak of this distribution is still above the etching threshold the slopes decline below it on a much shorter depth interval compared to a sample without annealing. This measure defines the interface of modified and unmodified material more clearly and increases the etching contrast[52]. The final wet etching step removes all the material that is damaged above the threshold. This also means that slightly modified material is still present. The remaining modification is big enough to cause a volume expansion of the LiNbO₃ that results in mechanical stresses and deformation of the etched structures[142], [144], [158], [200]. The expansion is very anisotropic and needs to be considered carefully when designing a patterned membrane. Full annealing of all defects of the LiNbO₃ is eventually accomplished by heating the sample at 500°C for 60 min[60].

2.4 Optical characterization techniques

The optical characterization of LiNbO₃ micro and nanostructures requires light to be coupled efficiently in and out of the respective structures. To obtain high efficiency coupling the incident optical field must be closely matched to the modal field distribution of the tested structure. The LiNbO₃ waveguide and resonator structures under investigation here have small mode field sizes. Therefore, efficient coupling is demanding and requires precisely aligned localized light delivery for example through microscope objectives and tapered or lensed optical fibers. This section introduces the respective elaborate optical characterization techniques that are relevant for the LiNbO₃ structures discussed in this work.

2.4.1 Near-field characterization of photonic crystal waveguides

In order to visualize light propagation in photonic crystal waveguides, a number of techniques can be used. For example, the surface of a photonic crystal can be recorded with a microscope[203]. When light is coupled in the waveguide, light emission along the line defect can be observed. It originates from the light scattering at surface defects and from radiation of leaky modes situated above light line. Both effects can be enhanced by an adapted design with engineered defects[204] or deliberate coupling to leaky modes[205]. Nonetheless, this kind of imaging is only an indirect, qualitative method and of limited reliability. Even a straight forward approach like measuring the input and output power of light transmitted through a photonic crystal waveguide is disturbed by extrinsic effects such that the results of these measurements may lead to normalized transmission efficiencies above 100%[206]. In order to fully characterize the modal properties of a photonic crystal waveguide, far-field imaging of the surface for different wavelengths can be used to retrieve the Bloch wave components of the leaky modes[205]. Propagating waveguide modes, which are evanescent in air, cannot be detected in the far-field. Instead, evanescent field coupling between the waveguide and a tapered optical fiber could be used[207]. More efficiently and with high spatial resolution is the detection with a scanning near-field optical microscope (SNOM)[208]. The SNOM scans a fiber optic tip across the sample surface at very small distance through which the optical near-field is collected and recorded. The scanning of the tip over large sample areas requires accurate positioning in-plane. In the direction normal to the surface, the positioning of the tip is challenging because a constant small gap of several nanometers needs to be maintained while scanning. This is accomplished through feedback mechanisms using constant force, shear force or tapping. Most relevant here is the shear force feedback, where the tip is mounted on an oscillating tuning fork. Amplitude and frequency of this oscillation are controlled and monitored to be fed back to the height control. This kind of feedback mechanism allows for the recording of a topographical image of the sample surface together with a map of the optical near-field. For collection of the near-field of the photonic crystals, dielectric fiber optic tips are commonly used. These fibers are also guiding the optical signal to a sufficiently sensitive detector. In this way using SNOM, evanescent fields of waveguide modes in integrated optical devices were imaged[207]. SNOM also allows the mapping of more complex patterns like photonic crystals of all kinds such as plain two-dimensional patterns[209], resonators[210] and waveguides[211]. SNOM is a very sophisticated technique that has many potential applications in the optical characterization of photonic crystals. In this

work it is used for mapping of waveguide modes and local loss and transmission measurements.

2.4.2 Tapered fiber coupling

An efficient way to couple light in and out of optical microstructures, such as waveguides and resonators, is evanescent coupling through a tapered optical fiber[212]. While this coupling scheme is commonly used for testing optical whispering gallery mode microdisk resonators[213], it can also be applied to photonic crystal waveguides[207], [214] and resonators[215], [216]. The characterization setup used in this work was developed by Carsten Schmidt[217] and will be described in the following. Fiber tapering is achieved by reducing the diameter of a standard optical telecom fiber with a diameter of 125 μm down to a diameter of approximately 1 μm . The fabrication of the tapered section uses a flame-brushing technique, where a hydrogen flame locally melts the fiber while it is pulled apart. In this way, the diameter of the fiber adiabatically decreases in this area[218]. When light is propagating through such a tapered fiber, it is guided in the core region of the fiber at first. In the tapered region, this mode field is transferred to a cladding guided mode with a substantial amount of optical power situated outside the tapered fiber. This effect enables the coupling to the evanescent fields of any suitable optical structure. Besides field overlap, another requirement for efficient coupling is the matching of the mode of the optical structure with the mode of the tapered fiber in space and time. This phase-matching can be adjusted by tuning the wavelength of the incoupled light and by tuning the propagation constants of the interacting modes. The diameter of the tapered region should be thin enough to cut-off higher order taper modes. Otherwise, light that is coupled to these modes is strongly damped during the transition to the single mode optical fiber part and possibly yielding inconclusive measurement data[219]. For the actual optical characterization of the respective structure, the tapered fiber is brought into its close proximity. This positioning requires high stability and precision since the coupling efficiency sensitively depends on the distance between fiber taper and optical microstructure. The positioning is done by motorized translation stages and is monitored through the closed-loop piezo actuator drivers, as well as through an optical microscope. The light sources used for the experiments in this work are tunable continuous wave (cw) lasers operating in the near infrared (NIR). Between the laser and the tapered fiber, a fiber optic circulator is installed. This setup allows the simultaneous measurement of the spectral characteristics of the transmission (behind the tapered fiber) and the reflection (at the

circulator) of the experimental system. In the case of a resonant structure, when the wavelength is tuned over a resonance wavelengths, a dip will appear in the transmission spectrum.

2.4.3 Cross polarized scattering microscopy

Optical microscopy is a general tool that is used throughout this work for many purposes including inspection during sample fabrication as well as optical excitation during elaborate characterization experiments. Optical microscopes are used in two ways: magnified imaging of small sample areas and local light delivery. Both aspects are implemented for example in the routinely performed characterization of light guiding structures. Light is incoupled from one side of the structure by focusing with an optical microscope. At the position where the light is outcoupled, another microscope images the signal on a detection device such as a photo diode or a camera. Many configurations are possible with the excitation beam being in-line with the guiding structure or perpendicular to it. It is beyond the scope of this section to give an in-depth review of all the relevant reported characterization techniques. Instead, the focus is put on just one technique, the cross polarized scattering microscopy, which is important in this work for the optical characterization of photonic crystal microresonators in chapter 5. These resonators typically have a strong mode confinement inside the waveguiding layer resulting in very weak coupling to the surrounding medium. The experimental access is difficult to realize and could be approached indirectly by adding a fluorescent or active medium in the cavity that radiates in correspondence with the cavity's mode field[220]–[222]. In the case of LiNbO_3 , this is nontrivial yet achievable by erbium doping, for example[223]. Another approach to test photonic crystal cavities could be evanescent field coupling either through a tapered fiber as described in the previous section or by direct integration of a waveguide in the sample fabrication. Both schemes may impede the characterization process by adding more control parameters and additional mechanical load to a fragile structure. In contrast, cross polarized scattering microscopy appears to be less complicated and very suitable for this purpose[224]. The measurement scheme is illustrated in Figure 3. Linearly polarized light from a tunable cw laser is transmitted through a polarizing beam splitter, followed by a half-wave plate that rotates the polarization by 45° and a high numerical aperture microscope objective that focusses the light on the photonic crystal resonator. In this way, the polarization of the electric field of the laser on the sample surface can be adjusted to have a defined angle with respect to the orientation of the cavity modes. The light that is

scattered back from the sample surface is collected through the same objective and directed through the same half wave plate, where its polarization is rotated again by 45° . In the end, the scattered signal passes the polarizing beam splitter and is, depending on the polarization state, directed to the detector. Input light with a wavelength that does not correspond to a cavity resonance will be reflected back by the photonic crystal surface. The reflected light mostly maintains its original polarization state and will therefore be filtered out by the polarizing beam splitter. For illumination at the resonance wavelength, the incident light interacts with the cavity modes leading to a modified polarization state in the reflected light. The reflected signal is then guided through the polarization optics to the detector. The cavity in this setup, therefore, can be regarded as a wavelength selective polarization rotator. Similarly, the SH being resonantly generated in the cavity is collected through the same optics, filtered out by a dichroic mirror and guided through an additional band pass filter onto a detector. In order to monitor the illuminating laser spot on the sample, cameras for FH and SH are included in the beam path through a beam splitter. Generally, this measurement scheme allows for the detection of very weak resonantly scattered signals from the cavity in the presence of a strong coherent background that originates from nonresonant reflections.

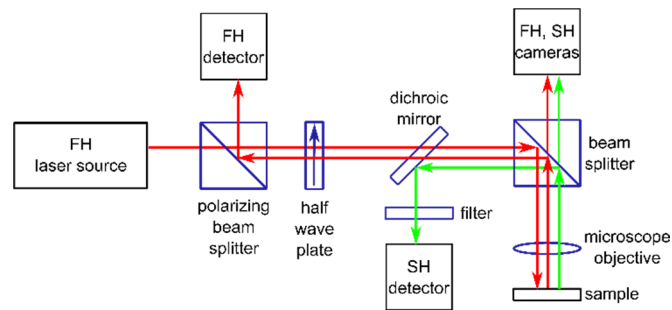


Figure 3: Schematic of the cross polarized scattering microscope with second harmonic detection.

Chapter summary

This chapter introduced the basic concepts and methods used for the investigation of nonlinear optical effects in microstructured LiNbO_3 . LiNbO_3 was presented as a versatile substrate material for nonlinear integrated optical devices. It followed a brief discussion of the physics of nonlinear optics in order to derive methods for the enhancement of nonlinear interaction processes, especially SHG. Waveguides and resonators were identified and explicated as key components to achieve the required enhancement through strong confinement of the interacting optical fields. Moreover, the current state of micro and

nanostructure technology that is relevant for the realization of the designed optical elements in LiNbO₃ was presented. Particularly the patterning of LiNbO₃ by means of IBEE was elaborated in detail. The chapter is concluded with descriptions of experimental techniques for the characterization of the linear and nonlinear optical properties of the fabricated LiNbO₃ structures with high spatial resolution.

3 Patterning of lithium niobate

In this chapter, patterning schemes for LiNbO_3 are elaborated. Particularly, the interaction of hydroxide solutions and ion beam irradiated LiNbO_3 is described in great detail. Conclusions for the applicability in nano and microstructure technology are drawn. Most relevantly, a KOH based IBEE process is developed from these investigations. KOH based IBEE represents the basis for the fabrication of functional optical elements that are a substantial part of the following chapters. In the second part of this chapter, FIB patterning is introduced as a tool for small area prototyping of LiNbO_3 optical elements. The FIB approach is combined with preprocessed membrane substrates such as LNOI or helium ion irradiated LiNbO_3 offering large flexibility and fast fabrication times. In the end of this chapter, additional patterning approaches are described that are complementing the main processes.

3.1 Hydroxide solution assisted ion beam enhanced etching

The basic principle of IBEE has been introduced in section 2.3.4. IBEE relies on the significantly different etch rates of irradiated and pristine LiNbO_3 which makes it a highly selective patterning process. It is common to all of the previously reported studies that the wet etching is based on an HF solution.

Although the HF based process is well-developed and understood[150] it can be disadvantageous in certain cases. One example regards the LNOI substrates consisting of a LiNbO_3 thin film and a SiO_2 layer on a LiNbO_3 substrate[51], [59]. LNOI is a very versatile platform for many kinds of integrated nonlinear optical devices[43], [58], [110], [225] but it is not compatible to HF based IBEE. This is because of the SiO_2 layer that would dissolve in HF and cause the detachment of the top LiNbO_3 layer from the substrate. Another drawback regards the elaborate safety measures when handling HF, because it is toxic, highly corrosive and, upon exposure, immediate medical attention is required.

As an alternative, hydroxide based etching of ion beam irradiated LiNbO_3 is presented in the following. Significant etching of ion beam irradiated LiNbO_3 was first discovered when a patterned silicon irradiation mask was removed by KOH etching from the LiNbO_3 substrate. The KOH did not only remove the silicon but also the irradiated LiNbO_3 . No previously reported work discussed or indicated that other etching solutions than those based on HF are suitable for IBEE. Therefore, to investigate the underlying etching mechanism a series of

experiments was conducted. For these experimental studies LiNbO₃ substrates were irradiated and etched in various hydroxide based solutions under different conditions. In the end, KOH based etching was identified to be the most promising HF substitute. This was confirmed by further experimental studies and a performance comparison with HF. The main results of this section have been published in reference [226].

3.1.1 Experimental conditions

The experimental studies were conducted with commercially available x-cut LiNbO₃ crystals. Similar to the IBEE process introduced before, the LiNbO₃ substrates were irradiated with a series of argon ions having energies of 60, 150, 350 and 600 keV. Energies and fluences were set up to result in a homogeneously damaged layer of 450 nm thickness (see section 2.3.4). Throughout the experiments, the energies were kept constant while the fluences were changed. In previous experiments it was found that a normalized fluence of 0.4 dpa corresponds to a complete amorphization of the LiNbO₃ crystal[27]. Therefore, the fluences here were varied between 0.1 and 0.6 dpa. During the irradiation the samples were masked to create an interface between irradiated and pristine material. Along this interface intermediate height measurements were conducted and recorded as a function of the etch time to determine the etch rate.

The wet etching was done with alkali metal hydroxide solutions of different concentrations, where the maximum concentrations were given by the water solubility of the respective compound. The temperature of the etchants, controlled by a water bath, could be heated up to 70°C. After each etching step, a height profile was measured by means of white light interferometry using an optical microscope with a field of view of $0.6 \times 0.6 \text{ mm}^2$. The images were recorded at different positions and used for a minimum of twenty height profile measurements normal to the interface of etched and un-etched regions. In the end, the average height from every step is plotted as a function of etch time, see for example Figure 4. At first, the etch depth increases linearly proving that the defect concentration from the ion beam irradiation is constant down to the designed depth. When this depth is reached by the etching process, the etching stops. The slope of the linear portion of the plot represents the etch rate that can be calculated by linear regression. This general measurement scheme was used to determine the etch rates during all of the following experiments.

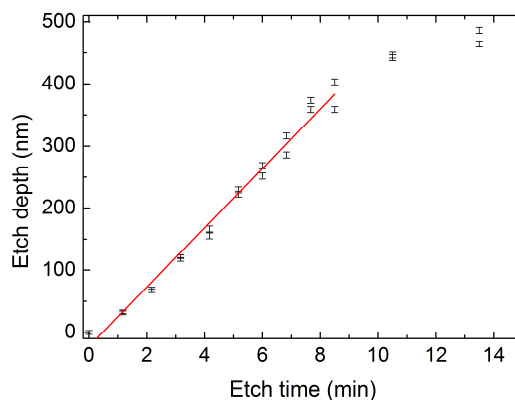


Figure 4: Etch depth as a function of the etch time for a normalized fluence of 0.5 dpa and etching in KOH (50%, 65°C). From the linear slope at the beginning the etch rate can be calculated.

3.1.2 Results and discussion

In order to experimentally study the etching mechanism in hydroxide based IBEE, solutions of different chemicals containing alkali metals were tested: NaOH, KOH, RbOH, CsOH. For all of these etchants a significant etch rate was measured, see Figure 5. When dissolved in water, hydroxides of alkali metals ionize into hydroxide ions and alkali metal ions. To verify the influence of the alkali metal ions, etching tests were done with the aqueous solutions of NaCl and KCl that dissociate into an alkali metal ion and a chlorine ion. No etching was detected in these tests, it can hence be concluded that only the hydroxide ions facilitate the etching process or act as a catalyst.

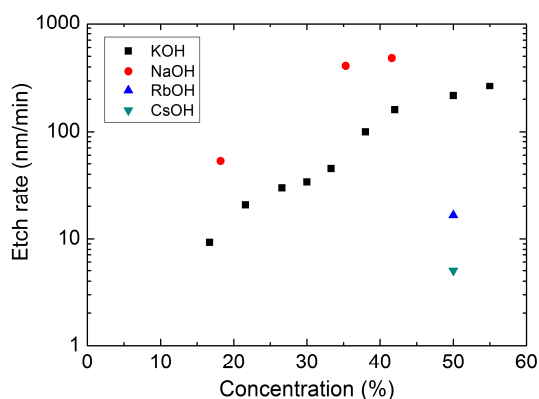


Figure 5: Etch rates as a function of the concentration for several hydroxide solutions measured at a temperature of 65°C, the irradiation of LiNbO₃ was done with a normalized fluence of at least 0.45 dpa.

The etch rates of the tested chemicals are plotted in Figure 5 as function of their concentration (given in percent by weight throughout this work) in aqueous solution at 65°C. The results

show that the etch rates can differ by orders of magnitude from each other. This behavior is supposed to be a result of the water solubility of the reaction products and is illustrated for the case of KOH and NaOH.

The etching of an ion beam irradiated LiNbO_3 sample in NaOH (41.6%, 65°C) for 5 min results in the formation of crystallites on the LiNbO_3 surface, see Figure 6(a). These crystallites are several tens of micrometers large. They were picked up with a micro manipulator needle using the FIB. In this way, the crystallite was transferred to a neutral background for an energy dispersive X-ray (EDX) analysis. The EDX analysis uses the characteristic X-ray emission from a target material that is stimulated by a high-energy electron beam to evaluate its elemental composition. The EDX analysis of the crystallites shows the presence of niobium, sodium and oxygen. This leads to the assumption that the crystallites are made out of NaNbO_3 which is further supported by Na^+ , OH^- , NbO_3^- and Li^+ ions being involved in the reaction. Additional sonication was found to reduce the crystallization by avoiding the local saturation of reactants, see Figure 6(b). Although the reaction appears to be quite similar, no crystallites have been observed in the case of KOH etching, where the formation of KNbO_3 could have been expected.

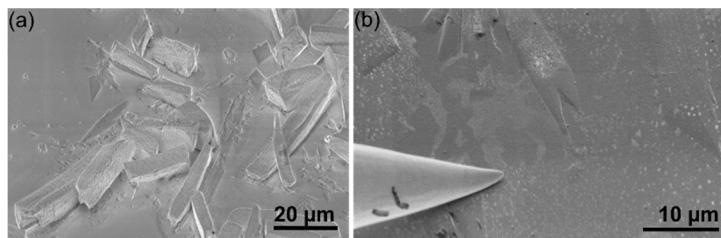


Figure 6: Scanning electron microscope images of ion beam irradiated LiNbO_3 surfaces after etching in NaOH (41.6%, 65°C) (a) without and (b) with sonication. (b) The sharp tipped object is metallic needle that was used to locally dissipate charges.

Another dissimilarity between KOH and NaOH etching are the observed etch rates. The maximum etch rate measured for NaOH is about two times larger than for KOH. The etch rates are a measure for the speed of the chemical reaction taking place at the sample surfaces. The speed of any chemical reaction can be influenced by adding or removing reactants. In the given etching process, a reaction product can be removed because of its low water solubility which would cause it to settle and to form crystallites. The compensation of the resulting imbalance in the reaction consequently leads to its acceleration. This line of argument can be applied to the reaction products of KOH and NaOH etching. They have a water solubility of 0.792 g/l (KNbO_3) and 0.262 g/l (NaNbO_3) at 50°C [227] explaining their different etch rates, eventually.

In conclusion, an experimental study about the performance of several hydroxide solutions in the IBEE process has been presented. A fundamental model for describing the respective chemical reactions still needs to be deduced from these findings as well as from future studies, which is outside the scope of the presented experimental approach. Nonetheless, important implication for the applicability in microstructure technology can be found in the results. NaOH appears to be unsuitable because the surface quality is impaired, even with simultaneous sonication, which could possibly destroy high-aspect ratio structures. RbOH and CsOH are unsuitable as well, mainly because of their small etch rates. It can, hence, be concluded that KOH is the only etchant, out of all the etchants investigated here, which is compatible with the demands of microstructure technology for the fabrication of optical elements in LiNbO₃.

3.1.3 KOH based ion beam enhanced etching

In the following, further experimental results will be presented and discussed to assess the performance and applicability of KOH based IBEE in comparison to the HF based process.

In Figure 7(a) the dependence of the etch rate upon variations of the KOH concentration is plotted again scaled linearly. The samples were irradiated with a normalized fluence of at least 0.45 dpa to ensure that the LiNbO₃ crystal is amorphous[27]. A significant increase of the etch rate from 10 nm/min to 260 nm/min at a concentration of 55% can be observed. The etchant temperature was 65°C for the concentration dependent measurements with 55% being the corresponding maximum KOH concentration that can be dissolved in water.

The temperature dependence of the etch rate for samples irradiated with a normalized fluence of 0.6 dpa and etched in 33% KOH is shown in Figure 7(b). The etch rate rapidly increases in the investigated temperature range by almost four times. From the Arrhenius plot[228] of this data the activation energy can be calculated to be 0.67 eV. Because the etch rates do not depend on whether sonication is used or not, diffusion mediated processes that could possibly influence the etch rate can be ruled out. Therefore, the activation energy exclusively characterizes the chemical reaction at the sample surface. It is in good agreement with the activation energy of HF based IBEE which was found to saturate around 0.6 eV for heavily damaged crystals with normalized fluences above 0.25 dpa[150].

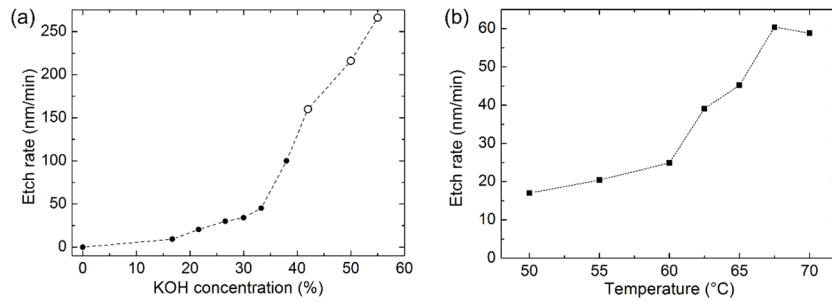


Figure 7: (a) Plot of the etch rate as a function of the concentration of the KOH (65°C) solution. The open circles represent samples irradiated with a normalized fluence of 0.6 dpa, whereas the fluence is 0.45 dpa for the filled squares. These different fluences do not affect the etch rate because the crystal is damaged above the threshold. (b) Etch rate as a function of the temperature of the KOH (33%) solution for samples irradiated with a normalized fluence of 0.6 dpa.

The applicability of an etching process for microstructure technology depends on the selectivity of the process. That means, a large difference of the etch rates in irradiated and non-irradiated areas must be provided. This behavior was tested by measuring the etch rates as a function of different normalized fluences ranging up to 0.6 dpa. Prior to this experiment, the reference etch rate of a non-irradiated sample was measured by partially covering the LiNbO₃ surface with a gold film followed by wet etching for several hours. Taking the tolerances of the height measurement into account, an etch rate below 0.006 nm/min was identified in the end. This etch rate of the non-irradiated and unmasked area is small enough to be neglected which is an important requirement for a large selectivity of the etching process. The dependence of the etch rate on the normalized fluence is shown in Figure 8(a). The etching was done at a moderate temperature of 65°C and a concentration of 33.3%. Normalized fluences below 0.1 dpa result in very small etch rates that rapidly increase between 0.1 and 0.4 dpa, saturating at around 45 nm/min. A very similar behavior was found for HF based IBEE, too. To allow for a quantitative comparison, Figure 8(b) shows a plot of the etch rates of HF and KOH based IBEE. The plotted etch rates are normalized to their respective maximum values in the saturation region (above 0.4 dpa). When fitting the data in the region between high and low etch rate by linear regression, the resulting slope is the normalized etch rate contrast which can be used to compare both processes. The normalized etch rate contrasts amount to $5.2 \pm 0.1 \text{ dpa}^{-1}$ for HF and to $5.6 \pm 0.2 \text{ dpa}^{-1}$ in the case of KOH. These results prove that KOH and HF are indeed similar in terms of selectivity. Therefore, it can be concluded that KOH qualifies to be used as a substitute for HF in the IBEE process. An example of a photonic crystal patterned with KOH etching in a freestanding membrane is shown in Figure 9. With respect to the patterning of complex LiNbO₃ structures during the

course of this work, the presented results are invaluable. From a broad experimental study about the feasibility of hydroxide based etching of ion beam irradiated LiNbO_3 , a process was developed that successfully replaces the potentially dangerous and, in terms of substrate compatibility, limited etchant HF. In chapter 4, examples of LiNbO_3 structures based on LNOI substrates are presented that could not be realized without the modified process.

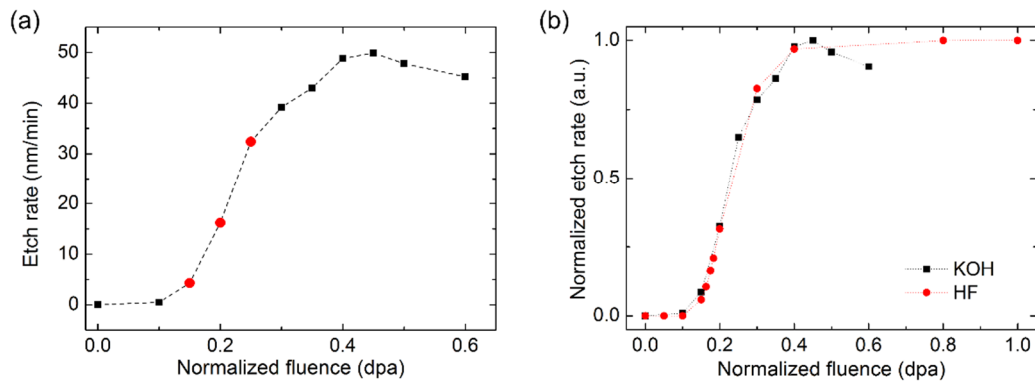


Figure 8: (a) Plot of the etch rate as a function of normalized fluences showing the selectivity of KOH (33.3%, 65°C) assisted ion beam enhanced etching. The etch rate contrast is calculated using the red points. (b) Plot of the etch rates normalized to their respective maximum values as a function of normalized fluences comparing the selectivity of the etchants KOH(33.3%, 65°C) and HF(3.7%, 40°C, from reference [150]).

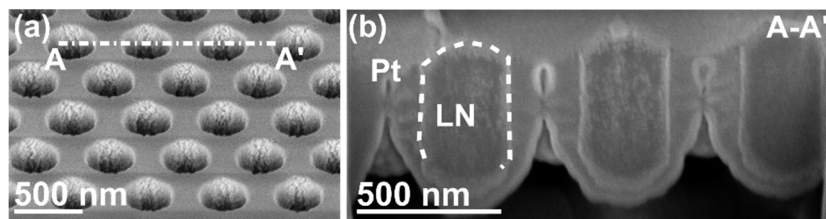


Figure 9: (a) Scanning electron microscope image of a photonic crystal membrane fabricated by KOH-assisted ion beam enhanced etching. A gold layer is deposited on the sample for charge dissipation during imaging. (b) Focused ion beam (FIB) cut cross-section of the membrane. To increase the material contrast and to protect the leading edge during FIB patterning, a layer of platinum is locally deposited.

3.2 Focused ion beam patterning of lithium niobate membrane substrates

Focused ion beam (FIB) patterning has already been introduced as a versatile tool for small area prototyping in section 2.3. Especially regarding the short processing time FIB became indispensable in situations, where the design idea of a single small scale structure, such as a photonic crystal resonator, needs to be tested in an optical characterization experiment. FIB patterning of LiNbO_3 micro and nanostructures was reported already for the fabrication of

photonic crystals in planar waveguides[79], [102]–[105], [107], [109], [111], [112], [117], membranes[56], [110], [113], [115], [116] or the bulk crystal[100] with added electro-optic[79], [108]–[110], [112], acousto-optic[114] and pyro-electric[113] functionality. The approach presented here uses preprocessed membrane substrates, where the membranes act as planar optical waveguides confining the light vertically. The horizontal confinement, amongst other effects, is realized by a suitable structure patterned by FIB. The membrane substrates can be either helium ion irradiated LiNbO₃ or LNOI. The helium ion irradiation is carried out as described in section 2.3. It allows the precise adjustment of the membrane thickness and of the air gap height underneath without the need of any further processing. LNOI substrates are available with fixed film thicknesses that may require additional height adjustments according to the device design. Such an adjustment can be realized by thinning of the membrane with ion beam etching (IBE) which will be elaborated later in this chapter.

3.2.1 Direct patterning of LNOI and helium ion irradiated LiNbO₃ substrates

Our approach is applicable for two different kinds of substrates: LNOI and helium ion irradiated LiNbO₃. The substrates have been diced to a small size of few mm² accounting for their relatively high monetary value. The samples are then glued to a carrier chip for improved handling using double sided adhesive carbon tape. This tape was chosen because it has a good electric conductivity and is resistant against all chemicals involved in the sample processing, especially HF based etchants. Next, the samples are deposited with a conductive layer of gold or carbon that allows for the dissipation of charges during scanning electron microscope (SEM) and FIB operation. The patterning is done in a ZEISS NEON 60 CrossBeam machine. The beam deflection system of the FIB column is connected to the external lithography system RAITH ELPHY Quantum. The FIB column is usually operated with an acceleration voltage of 30 kV. The probe currents are chosen depending on the resolution that is required by the respective layout. The choice of probe current and the corresponding probe diameter is specific to our FIB and represents a compromise between processing time and resolution. For photonic crystals in LiNbO₃ holes of 300 nm diameter and a depth of 500 nm are common, which is typically realized with a probe current of 100 pA. An unwanted effect during FIB patterning is redeposition of sputtered material at the inside of high aspect ratio structures. Especially for very small structures redeposition can prohibit the patterning down to the designed depth. Larger structures, mainly as a result of redeposition, have non-perpendicular sidewalls, cylindrical holes for example will become conical[118],

[119]. In order to reduce this effect, the structures presented here are patterned in at least ten iterations down to the sacrificial material (either helium irradiated LiNbO_3 or SiO_2)[229]. Each of these iterations contains the full pattern with a fraction of the total irradiation dose. The repetitive patterning also leads to a homogeneous distribution of the redeposited material over the entire write field and good uniformity of the final structure.

After the FIB patterning is finalized, the conductive layer is removed and the sample is wet etched. During this etching, the etchant penetrates the sacrificial material through the openings in the surface pattern and from the side faces. Because the etching is selectively removing the sacrificial material a patterned membrane forms as the etch front laterally propagates. Two examples are given in Figure 10. The substrate type being used defines what kind of etchant is needed. In the case of helium ion irradiated LiNbO_3 diluted HF(4%, 40°C) and KOH(50%, 65°C) are suitable. For underetching LNOI a commercially available ammonium fluoride - HF mixture was used to remove the intermediate SiO_2 layer. Because the etch rates are quite similar, the etch time for all etchants is typically around 10 min and depends on the amount of underetching that is required by the respective application.

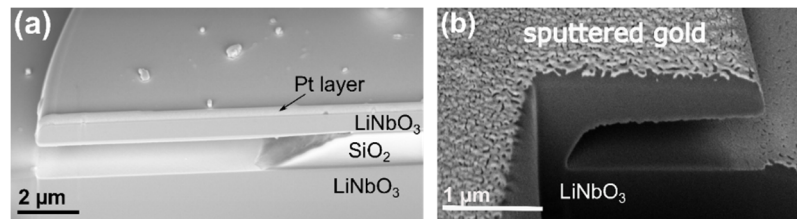


Figure 10: Examples for the underetching of lithium niobate membranes: cross-sections prepared by focused ion beam milling of (a) a microdisk fabricated in lithium niobate on insulator substrate and (b) sample edge of helium ion irradiated lithium niobate substrate after wet etching in HF based solutions.

3.2.2 The effect of gallium contamination

FIB patterning is based on local material sputtering with a focused beam of gallium ions. During the patterning process, gallium ions are implanted everywhere around the areas where material is removed. As a consequence, this gallium ion irradiation leads to a damaged crystal structure that potentially impairs the optical properties and becomes vulnerable to wet etching in a similar way that is used for the IBEE process[200]. In the following, the effect of these gallium contaminations is investigated with emphasis on the dimensional accuracy of the patterning[230].

Using the software SRIM, the ion beam irradiation of LiNbO_3 with 5 keV and 30 keV gallium ions, representing the preset operation conditions of the FIB, was simulated. The resulting

gallium ion distributions in LiNbO_3 are plotted in Figure 11. They can be qualitatively interpreted as the ion-induced defect concentration. Their maxima are located 5.5 nm and 18.7 nm below the surface with half widths of 5 nm and 17 nm. These calculations can be used as an upper estimate for the maximum interaction volume of the gallium ion induced IBEE effect during FIB operation.

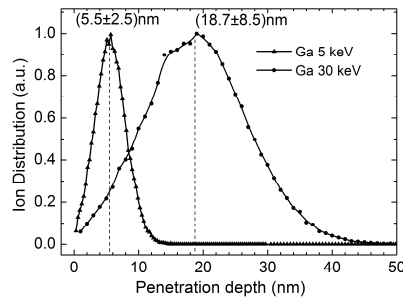


Figure 11: Distribution of gallium ions plotted as a function of penetration depth, from an SRIM simulation of the irradiation of lithium niobate with 5 keV and 30 keV gallium ions.

For the experimental verification of this effect grooves with different widths were milled into a LiNbO_3 substrates with gallium ions of energies 5 keV and 30 keV with a probe current of 100 pA. Subsequently, the samples were etched in diluted HF (4%, 40°C) for 5 min. Before and after the etching the widths of the grooves were measured with the SEM, see Figure 12. The inspected cross-sections were prepared by FIB milling after local deposition of platinum for an increased material contrast. For 30 keV gallium ions this measurement was carried out in 30 different places on the sample. A broadening of the groove of (17 ± 3) nm per side was found. Figure 12 shows the resulting gap to illustrate the effect.

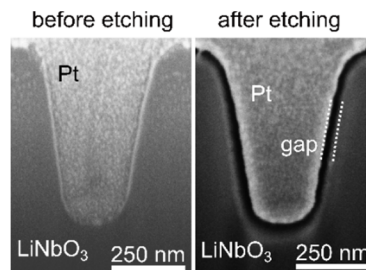


Figure 12: Scanning electron microscope images of grooves cut by focused ion beam milling (30 keV) in lithium niobate before and after HF etching. The 17 nm wide gap results from gallium ion enhanced etching at the interface.

For 5 keV gallium ions the groove widths were measured in four places and a broadening of 10 nm per side was found. Accounting for statistical and measuring errors, both results are in

agreement with the position of the maxima in the gallium ion distribution. The gallium ion induced defect concentration therefore seems to be large enough for wet etching. Further experimental proof is given by an EDX analysis. The resulting EDX spectra in Figure 13 were taken from a line scan with a 15 keV electron beam across an area that was patterned with 30 keV gallium ions. Especially at the edges of milled structures significant amounts of gallium have been found whereas the gallium was completely gone after etching.

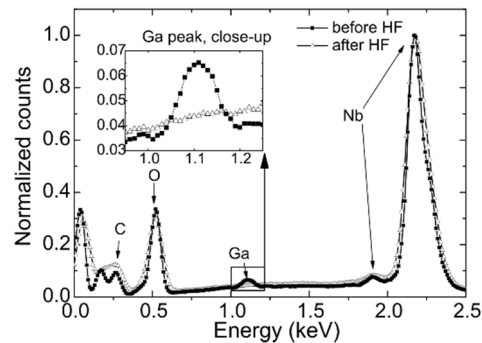


Figure 13: EDX spectra taken from a line scan of a FIB (30 keV) patterned area showing gallium contamination before and after etching in HF.

In conclusion, it was found that the low-energy gallium ion irradiation by FIB has a significant effect on the dimensional accuracy. Apart from that, it is well-known how ion beam irradiation considerably modifies the linear, non-linear and electro-optical properties of LiNbO_3 [78], [231]. For the contaminated areas, it is therefore required to be either removed by etching or, possibly, cured by thermal annealing. From the presented findings, however, the most important conclusion to be drawn is that gallium ion induced modifications need to be taken into account when designing functional sub-micrometer devices in LiNbO_3 .

3.3 Additional patterning approaches

3.3.1 Membrane thinning with ion beam etching

It was introduced before that preprocessed membrane substrates, such as helium ion irradiated LiNbO_3 or LNOI, are very useful for FIB based patterning. In contrast to the fully flexible lateral patterning with FIB, the membrane height is fixed by the chosen substrate. In order to introduce an additional degree of freedom, we use ion beam etching (IBE) for thinning the membrane substrates according to the device design before the FIB patterning. The

established standard IBE process for LiNbO_3 is done by means of argon ion etching at 400 eV and a current density of 0.3 mA/cm^2 with an Oxford Ionfab 300. The etch rate is relatively low (10.5 nm/min) allowing for nanometer precision control of the targeted layer thickness. Figure 14 shows examples of the resulting membranes after etching. Whereas the thinnest membrane realized by IBEE has a thickness of 200 nm [52], the combination of IBEE and dry etching can be used for thicknesses down to 30 nm . Such membranes are very fragile and are affected by any mechanical stress. The maximum area that can be covered with an intact thin membrane is therefore limited to around $100 \mu\text{m}^2$.

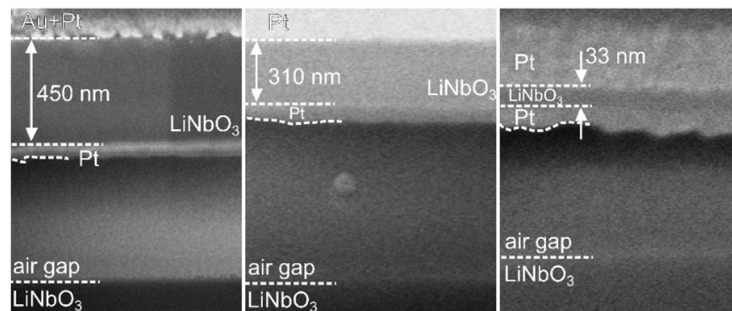


Figure 14: Scanning electron microscope images of lithium niobate membranes with thicknesses being adjusted by ion beam etching. Platinum was deposited for edge protection and enhanced material contrast during focused ion beam milling.

From the planar dry etching of LiNbO_3 an increased surface roughness could be anticipated which would lead to scattering and additional losses in any light-guiding structure. To quantify the influence of IBE, the root mean square roughness of the surface was measured by atomic force microscopy on an area of $10 \mu\text{m}$ by $10 \mu\text{m}$ before and after etching, resulting in very similar values for the roughness of 1.24 nm and 1.13 nm . It can be concluded that IBE maintains the original surface quality and, thus, making it a suitable process for membrane thinning.

3.3.2 Circular saw dicing

Although the main portion of this work is devoted to nano and microscale structures of LiNbO_3 , also macroscopic patterning techniques aside standard chip dicing had to be established as well. This type of patterning is needed to make the microstructures that are typically located on top of a small chip accessible for optical characterization experiments. Instead of using elaborate integrated optical waveguide patterns for the in-plane testing, the structures are addressed individually, for example with a microscope objective or by a tapered

or lensed optical fiber. Circular saw dicing has been reported to be a suitable tool for cutting high aspect ratio ridges[66].

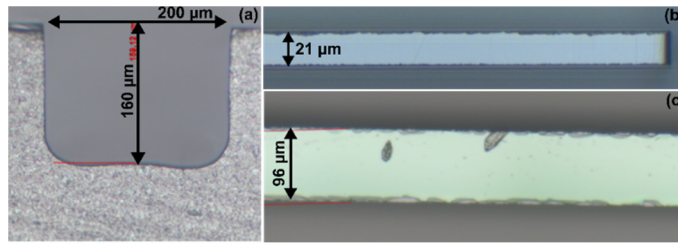


Figure 15: Optical microscope images of (a) a cross-section of a trench produced by a single circular saw cut and the top views of ridges in (b) bulk LiNbO_3 and (c) LNOI.

Similarly, for this work a dicing saw DISCO DAD-320 was set up for cutting relatively large ridges in accordance with the geometry required by the experimental framework. The minimum depth of the cut was required to be $70\ \mu\text{m}$ in order to position a standard $125\ \mu\text{m}$ -diameter optical fiber with its core region aligned parallel with the sample surface. The minimum width of the ridge was set to $50\ \mu\text{m}$ in order to fit the anticipated patterns on the sample surface properly for optical testing from both sides of the ridge. It was found that a saw blade with a thickness of $200\ \mu\text{m}$ and grit 4000 gives best results at 10,000 rpm and a feed rate of $0.3\ \text{mm/s}$. The trenches adjacent to the ridges are composed from repetitive cuts spaced $10\ \mu\text{m}$ apart from each other until the targeted width is reached. Examples of the resulting structures are shown in Figure 15. In conclusion, circular saw dicing has been established successfully becoming a tool for coarse preforming of the respective substrate materials.

3.3.3 Patterned SiN membrane irradiation mask

It was pointed out before that a large amount of patterning for this work is carried out focused on single microscopic structures like photonic crystal resonators. The structures are patterned by FIB on tiny substrate pieces because their acquisition is costly in terms of money and effort. Generally, substrate pieces smaller than $10\ \text{by}\ 10\ \text{mm}^2$ are difficult to process in resist based lithography. As an artifact of the resist spin-on coating, the resist wraps around the edge of a chip and accumulates up to several times of the nominal thickness. The resulting edge bead reaches about $2\ \text{mm}$ on the usable surface leading to significant handling and levelling problems during OL or EBL. In this situation, FIB clearly is an ideal tool for direct maskless patterning. An alternative suitable patterning approach is stencil mask lithography. It combines the advantageous maskless patterning of FIB with quick, large-area patterning of

OL and EBL, and it can be used on small substrate areas[232]–[234]. Ideally, stencil mask patterning can complement IBEE in the following way: Starting point is a SiN layer deposited on a silicon substrate. The thickness of the SiN is big enough to stop the high energy argon ions during the irradiation. Because the silicon substrate can be a full wafer or a sufficiently large chip, nanoscale patterning is done by standard EBL or OL. The resist pattern is then transferred in the SiN layer by dry etching. In the next step the membrane is created: An additional lithography step on the backside of the substrate creates large area openings at the position where the nano patterns are on the front side. The resist pattern is transferred in the silicon substrate by silicon-selective wet etching which stops at the SiN leading to the formation of a large area, freestanding, patterned membrane. To transfer this pattern onto the LiNbO₃ substrate, the resulting chip is flipped face down and positioned on the substrate surface to act as a mask during the ion beam irradiation. In this way it is not just possible to directly pattern small sample areas for immediate optical testing. It is further possible to make preforms of the expected structures for assisting the FIB patterning by reducing the writing times.

In order to establish the described process and to evaluate the feasibility and its limitations, a series of preliminary tests have been run. In these tests, SiN membrane have been used with a thickness of 480 nm that were deposited by means of CVD on a silicon substrate. The deposition process was adjusted to result in a tensile stress of 180 MPa. For the experiment, ready-made membranes substrates, which were opened from the back, have been used. Instead of using OL or EBL, test patterns were cut in the SiN membrane by FIB. To avoid charging effects during FIB patterning, a 20 nm layer of carbon was deposited on the SiN before. The test patterns consisted of large quadratic openings ($5 \times 5 \mu\text{m}^2$), gratings (period 1 μm , different filling factors) and a photonic crystal resonator (hexagonal pattern of holes with diameters of 220 nm, period 560 nm), see Figure 16. The patterned SiN membrane was placed on the surface of an x-cut LiNbO₃ chip. According to the process described in section 2.3.4 a series of argon ions was used for the irradiation followed by wet etching.

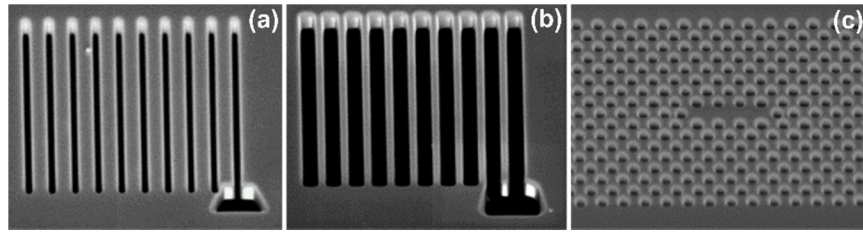


Figure 16: Scanning electron microscope images of irradiation masks fabricated in a 480 nm thick SiN membrane by focused ion beam milling. (a), (b) Gratings with period of 1 μm and different filling factors and (c) photonic crystal L3 resonator with period of 560 nm and hole diameter of 220 nm.

The area of the freestanding patterned membrane was around 1x1 mm². The combination of tensile membrane stresses and the mechanical support of the framing silicon substrate limit the initial bulging to a maximum of 25 nm. This deformation was taken from a white light interferometry measurement across the full membrane areas. A consequence of the ion beam irradiation for patterning is the implantation of argon ions in this masking membrane layer which leads to a volume expansion of the material and a tremendous increase of the membrane deformation to around 20 μm . Thermal annealing of the patterned membrane for 1 h at 500°C almost completely restores the initial bulge and, in principle, enables the re-use of the membrane. Figure 17 shows SEM images of the resulting structures in LiNbO₃ after wet etching in HF. In both cases, the pattern from the membrane was successfully transferred into LiNbO₃. A slight drift of around 100 nm can be observed in the photonic crystal which must be attributed to either the ion beam induced bulging of the masking membrane or mismatched thermal expansion of substrate and mask during the irradiation. To suppress the ion beam induced bulging of the membrane, SiN with larger tensile stresses can be deposited. Also, mechanical support patterns in the silicon substrates that are specific to the respective layout may be used.

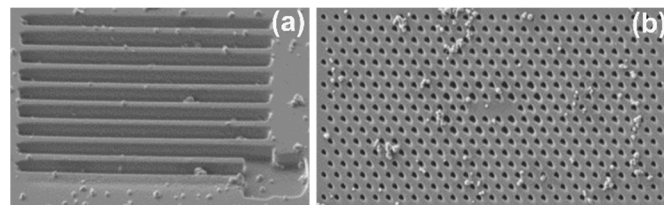


Figure 17: Scanning electron images of (a) a grating with a period of 1 μm and (b) a photonic crystal with period of 560 nm in bulk LiNbO₃ substrate after ion beam enhanced etching through a patterned SiN irradiation mask.

From these experimental findings, it can be concluded that stencil mask lithography is a suitable tool for the transfer of complex nanoscale patterns in small area LiNbO₃ substrates. The presented first proof of principle investigations show the great potential of the approach.

Chapter summary

In this chapter, patterning techniques for the realization of LiNbO_3 micro and nanostructures were presented. Based on our findings from broad experimental studies about IBEE of LiNbO_3 with hydroxide solutions, a new KOH based process was developed. In the course of this work, KOH based IBEE became a necessary complement to the commonly used HF based process especially for patterning tasks that involve LNOI substrates. IBEE is compatible with a lithography based chain of processes for the patterning of large areas. For research purposes though, FIB based direct patterning of single structures can be a valuable alternative. It was hence another objective of this chapter to present FIB patterning of either helium ion irradiated LiNbO_3 or LNOI membrane substrates. In particular, the effect of gallium contamination as a consequence of FIB patterning was investigated. The chapter ends with a set of patterning approaches which are essential additions to IBEE and FIB patterning. In this regard, planar dry etching was studied for thinning membrane substrates to a specific layer height. Circular saw dicing was presented to enable the coarse patterning and pre-forming of the substrates. Eventually, all of the presented approaches have been used for the realization of LiNbO_3 optical elements, which are shown in chapters 4 and 5.

4 Linear and nonlinear optical properties of nanoscale waveguides

Waveguides are the basic building blocks of any integrated optical device. They are particularly useful in applications that use nonlinear optical processes like frequency conversion. Because the propagating light is confined over large distances in a waveguide, the conversion efficiency of the nonlinear interactions is much higher than compared to focusing in a bulk nonlinear medium. It is a further advantage that waveguides can be fabricated with high precision using modern microstructure technology which allows to control the waveguide dispersion for modal phase-matching. Compared to commonly used microstructured waveguides that could be realized by titanium indiffusion for example, the conversion efficiencies of nanostructured waveguides are generally higher. Nonlinear effects can be enhanced even further by using slow light, which could be achieved for example with a photonic crystal waveguide[235].

In the first part of this chapter, the fabrication of nanoscale wire-type waveguides is presented followed by their nonlinear optical characterization. Next, another kind of nanoscale waveguide, a photonic crystal waveguide, is introduced, reporting about the characterization of its linear optical properties. These results represent an important basis and requirement for the realization of nonlinear optical resonators based on photonic crystals which are the subject of chapter 5. Finally, this chapter is concluded by showing how the presented wire-type waveguides can be metalized at the sidewalls resulting in a metal-insulator-metal structure which could be potentially useful to parametrically amplify propagating plasmonic modes.

4.1 Planar optical waveguides

In this section, the optical properties of thin LiNbO_3 membranes for highly efficient cascaded third harmonic generation (THG) will be discussed. Generally, THG is an interesting process that can be valuable, for example, for the realization of compact laser sources in the visible wavelength range[236] or in telecommunication applications[237]. Normally, THG is a result of third-order nonlinear processes. Because of the mostly small magnitude of the cubic material nonlinearities, this process is less efficient than quadratic effects. LiNbO_3 has a dominant quadratic and a weak third-order nonlinearity which makes direct THG very

inefficient. Therefore, a cascaded two-step process is used[238], [239]. First, the second harmonic (SH) is generated from the fundamental harmonic (FH). The SH is then mixed with the FH again in a sum-frequency generation (SFG) process resulting in the third harmonic (TH). Both processes, second harmonic generation (SHG) and SFG, are second-order nonlinear processes that can make the cascaded THG significantly more efficient than THG from a cubic nonlinearity[240]. To achieve maximum efficiency SHG and SFG must be phase-matched simultaneously which could be done for example by quasi-phase-matching in an aperiodically poled structure[241]. Large efficiencies are also possible using modal phase-matching in a thin planar waveguide[242]. In this way, highly efficient THG can be obtained from a 206 nm thick z-cut LiNbO₃ membrane with an optical pump in the NIR wavelength range and light propagation along y-direction[242].

The fabrication of the respective freely suspended planar waveguides is possible using LiNbO₃ membrane structures that have been demonstrated in the previous chapter. The waveguides could be realized based on either helium irradiated LiNbO₃ or LNOI substrates. In any case, the designed waveguide height needs to be met with nanometer precision over the entire sample area which is technologically challenging, yet feasible. Nonetheless, a successful experimental demonstration of the proposed effects has still to be completed. Although the structures are relatively simple to fabricate, a proper optical characterization is challenging. The anticipated results would be moderately interesting and a mere proof of concept at best. More profound in terms of applicability and scientific impact are waveguiding structures that provide also horizontal confinement of the optical modes. Such wire-type waveguides are basic elements of integrated optics and can be conveniently attached to standard fiber optic characterization equipment. The design, fabrication and characterization of these waveguides is discussed in the following sections.

4.2 Freely suspended wire-type waveguides made from bulk LiNbO₃

This section deals with waveguides that are fabricated by IBEE only and that are intended to be used as microscopic light sources or imaging probes for microscopy in biology applications[170]. The waveguides are made in large quantities and transferred into a liquid that can be pipetted onto any target material, such as biological samples. Even though their sizes are at the nanoscale, nanowaveguides can be used for nonlinear frequency conversion acting

as light sources of nonlinear signal. Nanowaveguides from many different materials have been reported including CdS[243], GaAs[244]–[246], AlN[247] and GaP[248]. Being compact light sources, detached nanowaveguides can be precisely positioned and used for nanowire microscopy[249] or local light delivery to excite fluorescent materials[249], [250]. Especially semiconductors have been studied for these applications because of their strong nonlinearity[4], [251] and straightforward chemical synthesis[252]–[254] [27–29]. However, the applicability is limited because most semiconductors have a large absorption in the visible wavelength range. This drawback can be compensated by using LiNbO₃ which has the required transparency, strong optical nonlinearity and bio-compatibility[255]. For the purpose of local light delivery in biological imaging applications LiNbO₃ nanowires usually are chemically synthesized[168], [256]–[258]. In contrast to top-down approaches the shape and crystal orientation cannot be controlled. Such synthesized particles have a broad size distribution making quantitative studies of their optical properties very difficult. Therefore, we developed a deterministic patterning technique that is based on lithography and subsequent IBEE of the LiNbO₃ substrate. In contrast to similar top-down approaches using FIB or other dry-etching techniques[131], [138], [259], IBEE allows for the realization of freely suspended waveguides[250]. These waveguides can be detached from the substrate and brought into a liquid that can be easily pipetted onto any sample surface.

4.2.1 Fabrication by IBEE and process simulation

The sample fabrication starts with a wafer of congruent x-cut LiNbO₃ with a thickness of 1 mm. At first layers of SiO₂ (1000 nm), chromium (80 nm) and resist (300 nm, ZEON ZEP520A) were deposited on the surface (Figure 18(a)). The nanowaveguides are arranged parallel to each other forming a grating-like structure. This pattern is transferred into the resist by means of EBL (Figure 18(b)) and, subsequently, into the masking layers by RIE (Figure 18(c)). The resulting mask defines where the argon ions are irradiated into the LiNbO₃ substrate(Figure 18(d)). The irradiation was performed at energies of 600 keV with a fluence of $7.2 \cdot 10^{14} \text{cm}^{-2}$ and 350, 150, 60 keV with a fluence of $1.38 \cdot 10^{14} \text{cm}^{-2}$. The irradiation is designed to form a homogenous damaged layer from the surface down to 500 nm. Next, the fused silica and chromium layers were removed by wet etching (Figure 18(e)) followed by the helium ion irradiation with an energy of 285 keV and a fluence of $5 \cdot 10^{16} \text{cm}^{-2}$ at a temperature of 100 K (Figure 18(f)). The helium ion irradiation forms a buried damaged layer with a thickness of 450 nm that exactly connects with regions damaged by the preceding argon ion

irradiation. The sample was thermally annealed at 300°C for 30 min and etched in diluted HF (3.7%) at 40°C for 20 min. The etching removes the irradiated portions of the substrate resulting in the final pattern of narrowly spaced freely suspended nanowaveguides (Figure 18(g)). As a last step, the samples was again thermally annealed for 1 hour at 500°C to completely restore the crystalline structure. SEM images of the final structure are shown in Figure 19.

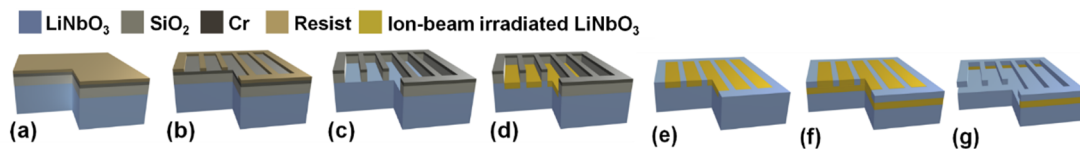


Figure 18: Schematic of nanowaveguide fabrication by ion beam enhanced etching. (Figure from [260]: R. Geiss et al. Nanotechnology 27, 065301 (2016))

The outlined fabrication process suggests that generally any EBL patterned structure can be realized, especially very narrow waveguides. Nevertheless, the shape of the resulting nanowaveguide cross-sections seemed to be limited. A waveguide height above 500 nm was possible only for waveguide width above 200 nm. To identify the limitations of the process a complete simulation of the ion beam irradiation and the wet etching was performed.

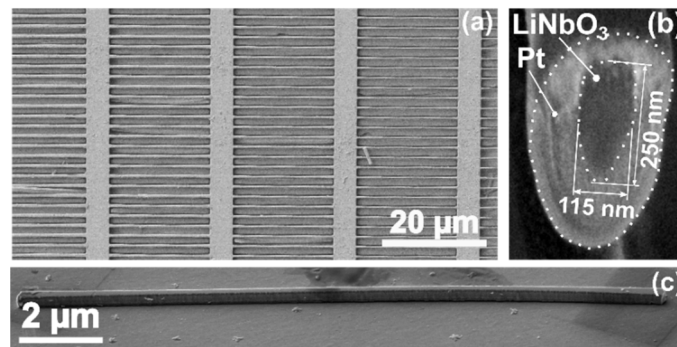


Figure 19: Scanning electron microscope image (a) of 20 μm long self-suspended lithium niobate nanowaveguides with different widths, (b) cross-section image of a nanowaveguide prepared by focused ion beam milling, (c) a typical nanowaveguide deposited on a SiO_2 substrate. (Figure from [260]: R. Geiss et al. Nanotechnology 27, 065301 (2016))

The simulation tool used the defect concentration of the ion beam irradiated LiNbO_3 (obtained from SRIM) along with the experimentally obtained dependence of the etch rate on this defect concentration[27] to compute the final geometry. The simulations are limited to two dimensions because the waveguides properties are defined by their cross-sectional shape only. Figure 20 shows the defect distributions that were calculated for the argon ion irradiation conditions described above and for mask widths of 120 nm, 80 nm and 60 nm. From these defect distributions, the final shape of the waveguide cross-sections, especially their widths

and heights, have been deduced. The inset in Figure 21 shows several waveguide cross-sections for mask widths between 50 nm and 1000 nm. It is clearly noticeable that the waveguide height decreases when its width is smaller than 200 nm. Figure 21 shows the aspect ratio (height/width) of the final nanowaveguide as a function of the mask width. The highest aspect ratio of 4 is obtained at 50 nm width. It decreases as the widths increase. Also, the curve is composed from two different decays (red dashed and green dotted lines) that intersect at the width of 200 nm. The break at 200 nm occurs because the height of the waveguide reaches 500 nm which is the maximum and pre-defined by the helium ion irradiation conditions. Therefore, for widths larger than 200 nm the height is fixed (green dotted line). For widths smaller than 200 nm, the height of the waveguide is additionally affected by the argon ion irradiation (red dashed line), which becomes evident from the spatial defect distribution after the argon irradiation, see Figure 20. Starting from the surface, the damaged regions reach down perpendicularly forming a sharp interface between irradiated and non-irradiated material. At a depth of around 200 nm, the interface regions significantly broaden such that the damaged regions are undercutting the masked areas. This kind of broadening takes place on both sides of the mask. As the mask width is reduced the interface regions overlap and the respective defect concentrations sum up reaching the threshold for etching. At a mask width of around 60 nm, this overlap is complete and the shape of the waveguide is exclusively determined by the argon ion irradiation. This effect, when superimposed by the helium ion irradiation, explains the width limit of 200 nm. These theoretical findings were confirmed experimentally. The SEM image in Figure 19 shows a cross-section of one of the wires confirming good agreement with the predicted shape. So far, nanowaveguides with widths down to 50 nm and with lengths of up to 100 μm have been realized. By further optimizing the irradiation conditions as well as shape and size of the patterned masking layer this limit can be pushed even further. The presented fabrication process in combination with the simulation tool allows to precisely tailor the shape of the waveguides on the nanoscale.

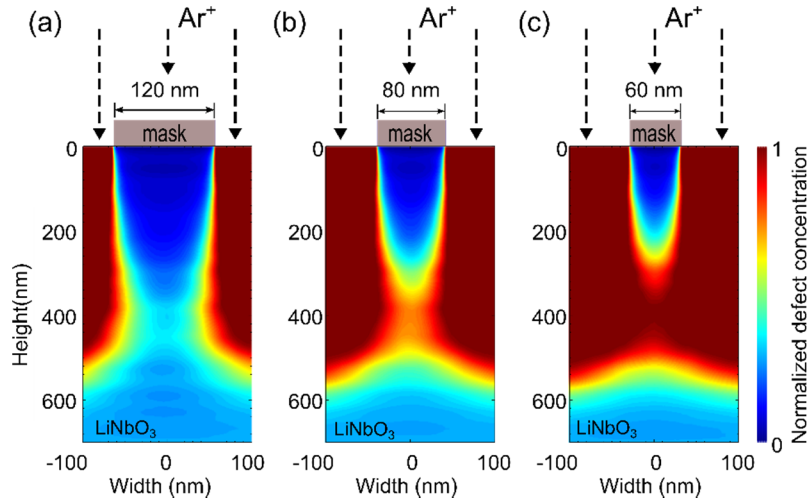


Figure 20: Calculated spatial distributions of the normalized defect concentration induced by the argon ion irradiations with mask widths of 120, 80 and 60 nm. (Figure from [260]: R. Geiss et al. Nanotechnology 27, 065301 (2016))

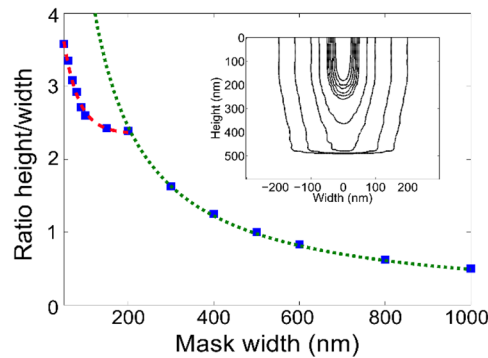


Figure 21: Calculated dependence of the height to width ratio of the nanowaveguides on the irradiation mask width. The height below 200 nm are mostly determined by the argon ion irradiation (red dashed line), while above 200 nm the helium ion irradiation is limiting the height (green dashed line). The height to widths ratios are taken from the cross-sections of the waveguide calculated for different mask widths (inset). (Figure from [260]: R. Geiss et al. Nanotechnology 27, 065301 (2016))

4.2.2 Optical characterization

The optical characterization was performed on single nanowaveguides that have been detached from the patterned chip by sonication in ethanol. A droplet of this nanowaveguide fluid was pipetted onto a transparent substrate where the ethanol is evaporated leaving behind well separated waveguides, see Figure 19. Chips cut from a silica wafer were used as substrates. To allow for charge dissipation during intermediate SEM or FIB inspection a 10 nm thick conductive indium tin oxide layer is deposited on the substrates initially.

To characterize SHG from the wire, an optical transmission microscope was used[245]. The FH pump beam comes from a titanium-sapphire laser with 283 fs pulse duration, 760 nm wavelength and 80 MHz repetition rate. The laser was directed normal to the substrate

surface, perpendicular to the nanowaveguide. The light is focused to a diameter of $5\ \mu\text{m}$ on one end of the nanowaveguide. The generated SH from the other end is imaged onto a very sensitive electron-multiplied charge-coupled device (EMCCD) camera. Polarization control is also included in the setup to match the incident polarization with the crystal orientation of the LiNbO_3 for maximal output signal. Band-pass filters centered at $470\ \text{nm}$ with a bandwidth of $\pm 110\ \text{nm}$ are placed in front of the EMCCD to suppress the pump and any unwanted radiation.

At first, waveguides with widths of $450\ \text{nm}$ to $600\ \text{nm}$ were tested with the pump beam having an average power of $85\ \text{mW}$. Figure 22(a) shows a white light image of the waveguide indicating the input facet. Before inserting the band-pass filter waveguiding of the FH could be observed clearly. Figure 22(b) shows an image of the SH light from the EMCCD. SHG from the propagated FH in the waveguide can be seen at the output facet. The SH signal at the input can be attributed to surface effects from the focused FH in this area. Tuning the FH power and recording the SH signal from the calibrated camera images, a quadratic dependence of SH on the FH power can be obtained, confirming the second order nonlinear effect, see Figure 22(c). For several similarly shaped waveguides under test, the detected SH typically amounts to several nW[261]. The smallest waveguide under test had a cross-section area of approximately $250\ \text{nm}$ by $300\ \text{nm}$ and a length of $30.5\ \mu\text{m}$, see Figure 23. The generated SH with a power of $62.7\ \text{fW}$ is shown in Figure 23 and was recorded at the output facet of the waveguide. The corresponding average pump power at the input facet was $68\ \text{mW}$.

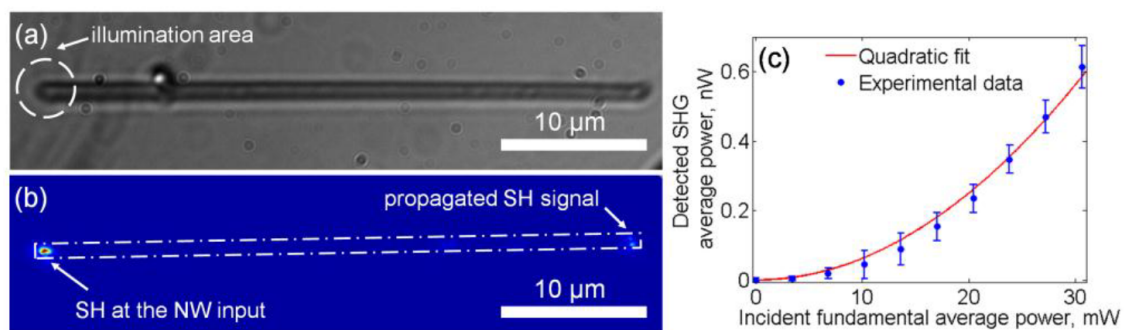


Figure 22: (a) Optical microscope image of a nanowaveguide, the area where the fundamental input field is focused is marked with a circle. (b) Optical microscope image of the SH light generated at the nanowaveguide input and propagated SH light at the output. The dashed line shows the position of the nanowaveguide. (c) SH signal at the NW output is plotted as a function of the incident power. The dots indicate the experimental results, the solid line is a quadratic fit and the error bars correspond to uncertainties when choosing the camera pixels for signal integration. (Figure from [250]: A. Sergeev, R. Geiss et al., *Opt. Express* 21, 19012 (2013))

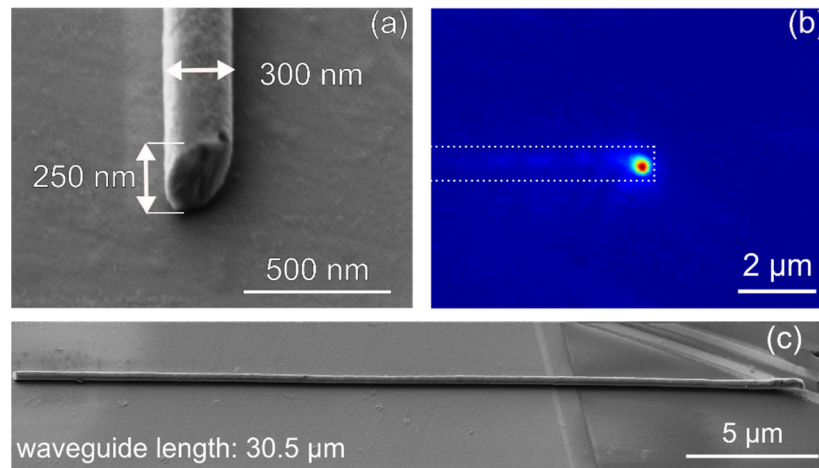


Figure 23: (a), (c) Scanning electron microscope images of a nanowaveguide placed on a neutral SiO_2 substrate. (b) EMCCD image of the nanowaveguide end facet showing the SH signal generated and guided in the waveguide, the dotted line shows the position of the waveguide.

The way this experiment is set up reflects the requirements of the targeted imaging applications in biological samples and does not allow the precise quantification of the waveguide properties. At first, it has to be pointed out that the waveguide facets did not receive any additional treatment and are randomly shaped after being detached by sonication. Therefore, the coupling of the light at the input and output is not deterministic and relies on scattering only. Hence, the measured scattered SH signal, although given quantitatively, should not be understood as a measure for the actual conversion efficiency of the waveguide. Besides these systematic limitations another limiting factor for the efficiency seems to be the surface roughness of the waveguide causing scattering of the SH along the waveguide[247], [262]. In conclusion, however, it was demonstrated that the waveguides indeed show the expected nonlinear properties. The presented waveguides can be seen as deterministic counterparts to chemically synthesized nanowires[168], [243] because of their size, their freely suspended arrangement and their sufficiently large conversion efficiency.

4.3 Wire-type waveguides on LNOI substrates

The waveguides presented in this section are intended for applications in integrated optics for light delivery to functional optical elements or for frequency conversion. In contrast to the preceding section, the waveguides are not meant to be detached and, instead, are required to be located at the substrate surface. Another requirement is a large integration density which makes high index contrast waveguides with cross-sections below $1 \mu\text{m}^2$ and small bending

radii an important component. Also, the efficiency of nonlinear frequency conversions can be significantly enhanced using the modal properties of the nanoscale waveguides[263]–[265].

The most common material platform for nonlinear nanowire waveguides for integrated optics is silicon. Lots of experimental studies have been reported that demonstrated for example parametric amplification by four-wave mixing[266], supercontinuum generation[267], [268] and generation of entangled photon pairs[269], [270]. Owing to larger nonlinear coefficient, materials with second order nonlinearity such as LiNbO_3 would be advantageous. But in contrast to silicon or other semiconductor materials used in integrated optics[271]–[274], the patterning technologies for LiNbO_3 are not as manifold and as far advanced. In this section, the realization of a nanoscale waveguide on LNOI substrate by IBEE is presented. In the past, similar waveguides structures have been presented in LiNbO_3 fabricated by dry etching[57], [59]. Also FIB could be used but is not considered here because it is impractical for the fabrication of millimeter long devices. A general limitation of dry etching LiNbO_3 are the inclined side walls of the patterns[122], [127], [130]. Because of the relatively low etch rates the mask material degrades and shrinks. The shrinkage along with the usually very isotropic etching causes the sidewall inclination. The effect can be avoided and reduced by local alteration of the substrate properties that increases the etch rate locally, for example by proton exchange[125] or ion beam irradiation[25].

Here, a fabrication scheme is presented to realize LiNbO_3 nanoscale waveguides with rectangular cross-sections from an LNOI substrate. To further confine the modal field inside the waveguide, the SiO_2 substrate was partially under-etched. The patterning was done by IBEE where the final wet etching step used KOH to protect the SiO_2 substrate layer[176], [226].

4.3.1 Fabrication by KOH based IBEE

The fabrication is based on LNOI substrates that were diced to a chip size of $10 \times 10 \text{ mm}^2$. A schematic of the process is shown in Figure 24. The top LiNbO_3 layer was etched by ion beam etching to a height of 530 nm corresponding to the final waveguide height and allows good vertical confinement of the interacting modes of FH and SH. As a mask for ion beam irradiation layers of SiO_2 and Cr with $1 \mu\text{m}$ and 80 nm thickness were deposited on the substrate. For EBL, a 300 nm layer of ZEON ZEP520 was spun onto the chip followed by the electron beam exposure. In this way, groups of waveguides with different widths were formed in the resist. This resist pattern was etched into the mask layers by standard dry-etching. The

finalized patterned mask was irradiated with a series of argon ions having energies of 60, 150, 350 keV at a fluence of $0.92 \cdot 10^{14} \text{ cm}^{-2}$ and 700 keV at a fluences of $4.8 \cdot 10^{14} \text{ cm}^{-2}$. This irradiation was designed to homogeneously damage the LiNbO_3 down to 500 nm depth which leaves a thin layer of 30 nm at the interface to the SiO_2 unaffected. As a consequence of the ion beam irradiation the volume of the target material expands. This expansion leads to significant mechanical stresses building up at the interfaces of irradiated and non-irradiated material[158]. Along with the ion beam induced damages, these mechanical stresses lead to a local enhancement of the etch rate[46]. This added effect, in the given waveguide layout, is present along the sidewalls of the waveguides. In the end, the combination of ion beam induced and stress induced etching causes the thin bottom LiNbO_3 layer to be opened down to the SiO_2 along the waveguides. After the ion beam irradiation, the chip was diced to a waveguide length of 1 mm followed by optical grade polishing. The irradiation mask was removed by chemical wet etching. For the SiO_2 a HF based etching solution was used that also partially under-etched the SiO_2 layer between the LiNbO_3 substrate and the LiNbO_3 thin film. This etching affected the entire circumference of the chip and leads to a noticeable semidetached arrangement of the waveguides near the facets. Since the lateral extent of the underetching is only around $1 \mu\text{m}$ the optical functionality of the millimeter long waveguide remains unaffected. The wet etching of the ion beam irradiated areas was done by KOH having a concentration of 50% (percentage by weight) and a temperature of 65°C . The etch rate for these conditions is approximately 200 nm/s, nonetheless an etch time of 15 min was chosen to guarantee complete etching of the sample. Because the selectivity of the KOH based IBEE is very good, a longer etch time does not affect the quality of the sample. The final etching step was a 1 min dip in the HF based silica etching solution which etches the SiO_2 underneath the top LiNbO_3 layer through the openings in the LiNbO_3 film along the waveguides. The final patterns are shown in Figure 25.

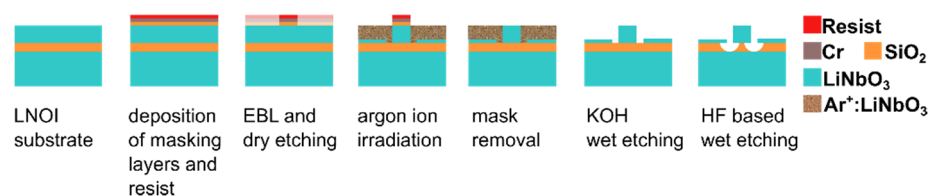


Figure 24: Schematic of the KOH based IBEE process for nanowaveguides on LNOI substrates. (Figure from [176]: R. Geiss et al., Opt. Lett. 40, 2715 (2015))

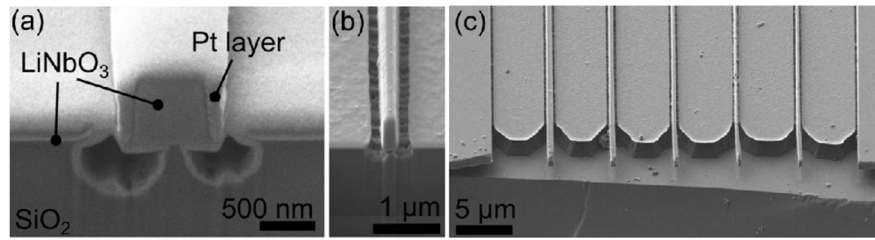


Figure 25: Scanning electron microscope images of waveguides made from LNOI. The waveguides have a height of 530 nm and widths of (a) 570 nm and (b) 220 nm. (c) Group of waveguides with different widths at the sample edge showing the undercutting. (Figure from [176]: R. Geiss et al., *Opt. Lett.* 40, 2715 (2015))

With the presented technique, waveguides with widths down to 220 nm have been realized. According to the findings in the preceding section, see Figure 20, the displacement distributions from the argon ion-irradiations extend under the mask. Given the mask is very narrow, the displacement distributions from both sides overlap causing undercut sidewalls and, after etching, an unwanted complete undercutting and detachment of the waveguide from the substrate. Taking these effects into account, a waveguide width of around 200 nm is the lower limit for these processing conditions. The irradiation conditions could be slightly modified to further decrease the width but the expected improvement would be insignificant.

4.3.2 Optical characterization

For the optical characterization a waveguide was chosen that allows for phase-matched SHG in the telecom wavelength range around 1.5 μm . The tested waveguide had a thickness of 530 nm, a width of 1.2 μm and was 0.9 mm long. A numerical mode analysis revealed that the most efficient SHG occurs between the TE_{00} mode of the FH and TM_{20} mode of the SH. The corresponding effective refractive index is $n_{\text{SH}}=n_{\text{FH}}=1.9439$ with the phase-matching condition fulfilled at $\lambda=1.413 \mu\text{m}$. In this configuration, the SHG is mediated by the d_{31} nonlinear coefficient of LiNbO_3 .

For the experimental characterization a lensed optical fiber was positioned at the front facet of the waveguide. The positioning was done by a piezo stage and monitored through an optical microscope from the top. The FH light came from a fiber coupled cw tunable laser followed by a fiber polarizer. The end facet of the waveguide was imaged on cameras for SH and FH using a microscope objective. The separation of FH and SH beam at the output was done by a dichroic mirror. The FH and SH powers at the output were measured either by integrating the camera images or using power meters. The results are plotted in Figure 26. Figure 26(a) shows the FH wavelength dependence of the normalized SH power. Within the tested

wavelength range of 200 nm width a peak of the SH power can be found at the phase-matching wavelength. To give proof that the measured signal is SHG, the power dependence was tested with the FH set to the phase-matching wavelength of 1.411 μm . The results are shown in Figure 26(b). A quadratic fit of the data points confirms that the generated signal is SHG.

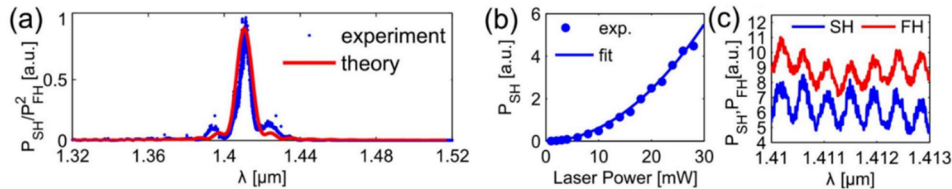


Figure 26: (a) Experimental and calculated SHG efficiency plotted as a function of the FH input wavelength. (b) Plot of the SH power as a function of the FH input power showing a quadratic dependence. (c) Spectra of FH and SH with Fabry Perot fringes for the estimation of the losses. (Figure from [176]: R. Geiss et al., Opt. Lett. 40, 2715 (2015))

Besides the nonlinear properties of the waveguide also the linear properties were tested. The linear losses of the FH mode were calculated from the contrast of the Fabry Perot fringes originating from the reflections at the end facets of the waveguide[275]. Figure 26(c) shows a close up view of the FH and SH signal. The free spectral range of this resonator was around 0.5 nm corresponding to a resonator length of 1 mm which is in good agreement with the actual sample length. The fringes of the SH signal were generated from the FH signal. They were not a resonance effect of the SH for which a four times smaller free spectral range would be expected. For the FH a loss of 61 dB/cm was calculated from the contrast of the fringes. This relatively high loss was attributed to surface roughness and the respective strong interaction of the modes with the sidewalls of the waveguides[274].

To quantify the conversion efficiency of the SHG, FH and SH were measured at the phase-matching wavelength. Taking into account the transmission properties of all involved optical components, the FH power at the input facet amounts to 737 μW . The generated SH is 305 pW, which corresponds to an efficiency of $6.9\% \text{W}^{-1} \text{cm}^{-2}$. Compared to a lossless waveguide of the same dimensions the resulting efficiency is 44 times smaller. The linear loss of the SH mode can be calculated by comparing the maximum theoretical efficiency with the measured efficiency, resulting in a loss of 256 dB/cm. Using all these results, a theoretical SH spectrum was calculated and superimposed with the experimental data, see Figure 26(a). The theoretical curve had to be shifted by -3 nm to perfectly overlap with the measured one. However, good agreement between theoretical and experimental data can be stated. It can, hence, be concluded that the technological approach to fabricate nanoscale waveguides on

LNOI substrates by KOH based IBEE resulted in the realization of devices showing the expected nonlinear properties. The efficiency of the nonlinear frequency conversion is comparable to earlier experimental works[276]. With the presented approach, in contrast to dry-etched waveguides[57], rectangular cross-section can be realized. They enable the controlled positioning of waveguides very close to each other allowing for reliable evanescent coupling which is needed for waveguide couplers in integrated optics or for the realization of complex waveguide arrays[277]. The demonstrated waveguides show the great potential of patterned LNOI substrates for applications in integrated nanooptics.

4.4 Photonic crystal waveguides

Photonic crystals attracted a lot of attention in the past decades because they allowed to control the propagation of light on a very small scale[178]. Especially the combination of photonic crystals with a substrate material that has a large optical nonlinearity gives rise to a large number of interesting phenomena and possible applications[278]. In the beginning, studies in this field were carried out mostly numerically. The first experimental studies were conducted with photonic crystals made from semiconductor materials having third order nonlinearities. More efficient nonlinear effects are expected for second order nonlinear materials such as LiNbO_3 . This was confirmed by both, theoretical[141], [279]–[284] and experimental[56], [70], [102]–[104], [109], [285], [286] studies which demonstrated the great potential of photonic crystal devices based on LiNbO_3 . Nevertheless, in comparison to other optical materials which were extensively studied experimentally in the field of photonic crystals, LiNbO_3 still is underrepresented. Whereas most other materials are compatible with standard semiconductor microstructure technology, LiNbO_3 is chemically very stable requiring adapted fabrication methods like IBEE.

In this section, the fabrication of a photonic crystal waveguide is presented based on a given IBEE based process[60]. It is the intention of this section to give a basic demonstration of the optical functionality of a photonic crystal membrane. In particular, the light propagation in a single-line defect photonic crystal waveguide was studied at NIR wavelengths. The propagation was recorded by a SNOM with subwavelength resolution. The propagation constants of the Bloch modes and thus the band diagram of the photonic crystal were calculated from the measurement data. The results of these measurements were compared to numerical data. Although LiNbO_3 is a nonlinear material, testing of the nonlinear properties is

outside the scope of this section. The focus is on the linear optical properties. The results from this section, however, will be the basis for the design of nonlinear photonic crystal devices presented in chapter 5. The main results of this section have been published in Ref. [287].

4.4.1 Sample layout and fabrication

The realization of a planar photonic crystal structure requires not just an array of air holes that represents the photonic crystal, but also a mechanism for the vertical confinement of the light. The mechanism finds its technological representation in planar waveguides made for example by annealed proton exchange[288], LiNbO₃ thin films from pulsed laser deposition[102] or crystal ion slicing[56]. It is common to these approaches that the refractive index contrast between the LiNbO₃ layer and the remaining substrate is relatively small. Consequently, the confinement of the waveguide mode is weak resulting in an inefficient interaction with the photonic crystal pattern. Therefore, the ideal situation with a maximum refractive index difference is a freely suspended membrane containing the photonic crystal pattern surrounded by air. This type of structure can be fabricated by IBEE in either LiNbO₃[60] or LNOI[110], [289] substrates on wafer scale, which is an important advantage compared to the mostly FIB based approaches reported so far[115], [116].

The waveguide structures were fabricated similar to the process illustrated in Figure 18. The substrate material was a 15 by 15 mm² chip x-cut LiNbO₃. At first, a layer of SiO₂ was deposited by CVD with a thickness of 1 μm, followed by PVD of an 80 nm chromium layer. The photonic crystal pattern was written by EBL in a layer of 300 nm resist (ZEON ZEP520A). After development of the resist, the chromium was patterned through the resist mask by RIE. The patterned chromium was then used as a mask for the dry etching of the SiO₂ by ICP-RIE. The patterned chromium and SiO₂ layers were used as a mask for the subsequent irradiation with argon ions (60, 150, 350 keV at fluences of $0.92 \cdot 10^{14} \text{ cm}^{-2}$ and 700 keV at $4.8 \cdot 10^{14} \text{ cm}^{-2}$). The energy and fluences of this ion-irradiation were set up to result in a homogeneous damage of the LiNbO₃ substrate from the surface down to the targeted membrane thickness. The next ion-irradiation was carried out using helium ions (285 keV and a fluence of $5 \cdot 10^{16} \text{ cm}^{-2}$), after the patterned masking layer was removed by chemical wet etching. The helium irradiation lead to a buried damaged layer in the LiNbO₃ that is connected to the damaged regions from the previous argon irradiation. During the helium irradiation, the substrate was cooled to 100 K to avoid bubble formation and cracking of the surface. In order to further sharpen the depth profile of the induced defects after the

helium irradiation, the sample was thermally annealed at 300°C for 30 min. Before the final wet etching, the sample facets were polished. To protect the sample edges from cracking during the polishing, a 4 μm thick layer of SiO_2 was deposited on the sample surface. In this way, the sample edge was elevated and possible cracks were forming in the SiO_2 layer, while the edge of the LiNbO_3 sample is covered and intact. After polishing, the SiO_2 layer was removed by selective wet etching. It followed the final wet etching of the amorphous LiNbO_3 in diluted HF (4%, 40°C). At first the holes were etched and then, through the holes, the membrane underneath. The extent of underetching is controlled by the etch time, whereas the height of the air gap is given by the helium irradiation. In the end, the sample was thermally annealed for 1 h at 500°C to remove any residual damage and to achieve complete restoration of the crystal structure.

The final structure was a so-called W1 photonic crystal waveguide consisting of an array of hexagonally arranged air holes, where at the position of one row in the ΓK direction no holes were etched. The period of the photonic crystal was 620 nm with a hole diameter of 310 nm. The orientation of the waveguide axis was along the crystal z-axis. The membrane height was 450 nm and the height of the air gap between substrate and membrane was 500 nm. An SEM image of the photonic crystal waveguide is shown in Figure 27.

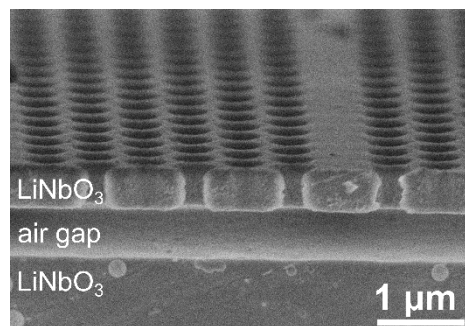


Figure 27: Scanning electron microscopy image of a W1 photonic crystal waveguide in a LiNbO_3 membrane. The polished sample edge is shown.

4.4.2 Optical characterization by SNOM

In order to map the field distribution in the waveguide and the surface topography at the same time, a SNOM was used in collection mode. Light from a broadly tunable cw laser source (1260 to 1630 nm, 2 mW) was coupled to the waveguide using a lensed optical fiber. The photonic crystal waveguide had a photonic bandgap for TE polarization only. Hence, a fiber coupled polarization control was added between the laser and the lensed fiber tip to control the input light's polarization. In order to collect the optical near-field from the sample surface,

a dielectric SNOM tip was placed few nanometers above the sample surface using shear force detection. The surface of the waveguide was scanned approximately 100 μm away from the front facet to avoid any scattering effects from the coupling region that would possibly disturb the measurement. The signals from the SNOM tip were recorded by a fiber coupled InGaAs detector while the sample topography was recorded at the same time using the shear force regulation of the SNOM. Figure 28 shows the resulting images for the wavelengths 1400 nm and 1550 nm. The images clearly show the localization of light along the line defect and a significant wavelength dependence of the field distributions. The recorded fields, according to [208], originate from the interference of several waveguide modes, which leads to the periodicity in the fields. The field that is collected by the SNOM above the surface, along the waveguide axis can be described as[290]:

$$E(x, y, z) = B + \sum_m u_m(x, y) \exp[i(\beta + mK)z]. \quad (14)$$

The coordinate system was defined according to the crystallographic system. The surface normal is oriented along x , while y and z are in the photonic crystal plane with z parallel to the waveguide axis. $m = 0; \pm 1; \pm 2; \dots$, B is the background signal, $K = 2\pi / a$ is the z component of the reciprocal lattice vector with the period a . β is the propagation constant of the Bloch mode with amplitude u_m . The observed field distribution is an interference caused by the SNOM detection of small signals that form a quasihomogenous background B [291]. The SNOM fiber collects plane-wave components of the near-field. The contribution to the collected signal depends on the magnitude of the projection of the wavevector on the surface plane[291]. The efficiency is particularly small for large magnitudes of the projected wavevector[292]. The resulting SNOM images, especially those of photonic crystal waveguide modes with a large effective index, are therefore significantly influenced even by weak scattered light signals. This influence is coherent and strong for fields with small wavevector projections resulting in an interference pattern that is superimposed on the actual waveguide mode. The irregularity of the resulting interference pattern is a result of the different participating plane-wave components that should approximately resemble an optical field propagating away from the surface with zero wavevector projection and, thus, constituting the homogeneous coherent background[291].

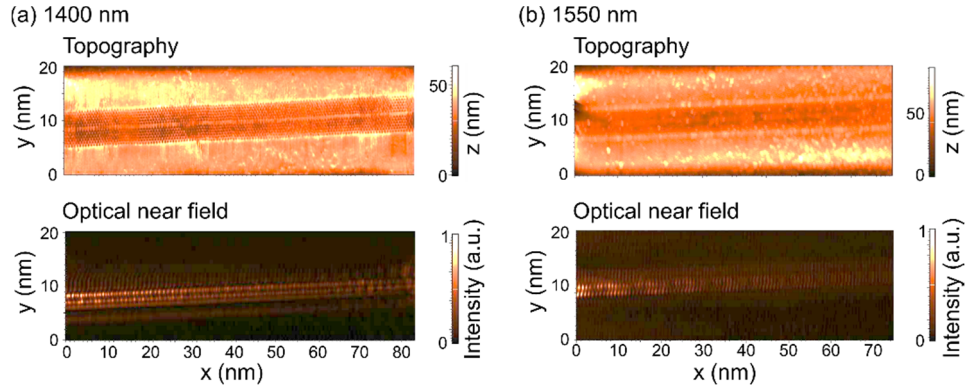


Figure 28: Topography and optical near-field of W1 photonic crystal waveguide obtained by SNOM for excitation wavelengths of (a) 1400 nm and (b) 1550 nm.

The intensity of the optical near-field that is collected by the SNOM mainly consists of the spatial frequency components β and $(K - \beta)$. For a waveguide that supports several Bloch modes with propagation constants β_1 , β_2 , and β_3 the signal harmonics are expected to be dominant at β_1 , β_2 , β_3 , $(K - \beta_1)$, $(K - \beta_2)$, and $(K - \beta_3)$. Information about the occurrence of these spatial frequencies in the waveguide can be extracted from the SNOM images that were recorded for different excitation wavelengths. A one-dimensional Fourier transformation was performed along the line defect that revealed the spatial frequencies clearly. Figure 29 shows the respective spectra for two excitation wavelengths. Figure 29(a) shows the spectrum for a wavelength of 1400 nm with a small number of peaks which corresponds to a single Bloch mode supported by the waveguide. A greater number of peaks corresponding to multiple Bloch modes was found for a wavelength of 1550 nm, see Figure 29(b). It is common to all the acquired spatial frequency spectra to have a characteristic peak at the frequency K representing the lattice vector. Peaks labelled with an asterisk could not be identified clearly and are omitted from the evaluation. They originated probably from cladding modes being excited by the input field that was not properly mode-matched to the waveguide. According to [293], the peaks with frequencies $2\beta_1$ and $(K - 2\beta_2)$ are attributed to backward propagating waves. The spatial frequencies obtained from these peaks have been related to Bloch modes by comparing them with a calculated band diagram (Figure 30). The band diagram was computed for TE-polarization using the 3D finite-element method (FEM). In the plot in Figure 30, the black squares represent the fundamental mode β_1 , red dots and blue triangles represent the higher order modes β_2 and β_3 . The error bars were estimated from the scan size of the SNOM image and the diameter of the tip apex. From the plot in Figure 30 it can be concluded, that the modes predicted from the band diagram have been excited in the experiment.

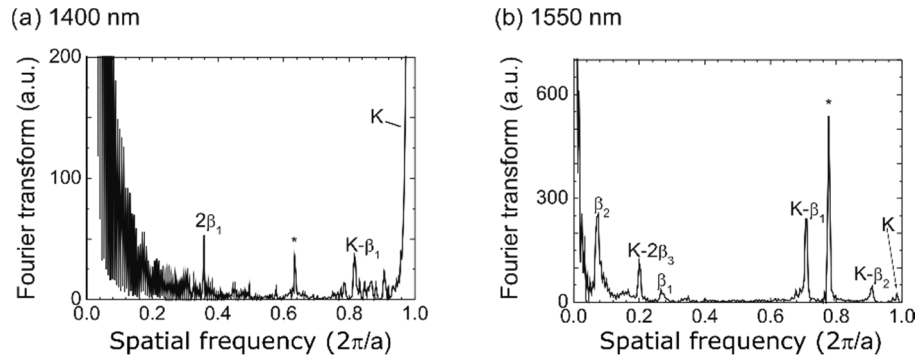


Figure 29: Fourier transforms of the optical near-field intensity along the line defect at (a) 1400 nm and (b) 1550 nm.

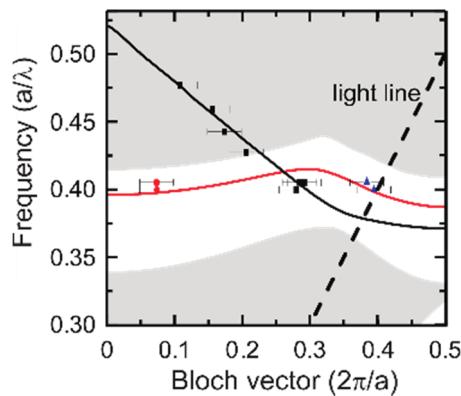


Figure 30: Band diagram calculated for TE-polarization of a W1 photonic crystal waveguide. Black curve: fundamental waveguide mode, red curve: higher order mode, shaded area: continuum of modes, black square correspond to the spatial frequency β_1 , red circles to β_2 and blue triangles to β_3 . (Figure from [287]: R. Geiss et al., Appl. Phys. Lett. 97, 131109 (2010))

Although not ideally suited, the SNOM setup was also used to measure a transmission spectrum of the photonic crystal waveguide. To record the transmitted light, the SNOM tip scanned an area of $4 \times 4 \mu\text{m}^2$ located on the line defect and $100 \mu\text{m}$ away from the input. The measured intensity was continuously accumulated while the wavelength at the input was tuned from 1260 to 1630 nm. The resulting transmission spectrum is plotted in Figure 31. The comparison with a calculated spectrum (3D FDTD) shows good agreement between theoretical and experimental results, where the minor deviations are due to imperfections of the photonic crystal.

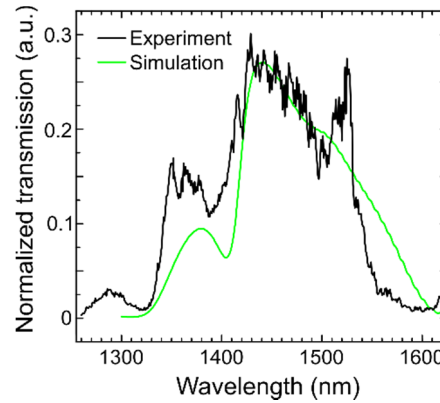


Figure 31: Measured and calculated transmission spectra of a W1 photonic crystal waveguide. The spectrum was recorded 100 μm away from the waveguide input. Both spectra have been normalized for comparison.

In summary, light guiding and confinement was experimentally demonstrated in a free-standing LiNbO_3 membrane comprising a photonic crystal waveguide. It was further shown that the band diagram and the transmission spectrum agree well with the calculations. In this way, it was proved that the numerical methods and the material parameters used therein are suitable for the modelling of complex photonic structures in LiNbO_3 . This result is an important requirement for the further development of even more involved patterns. Such patterns include for example photonic crystal resonators, which will be the focus of chapter 5.

4.5 Plasmonic nanowaveguides - design considerations and fabrication

In this section, a brief introduction of the physics of plasmonic waveguides will be given along with results of numerical modelling (taken from [294]) and the resulting implications for a specific device design. Based on the wire-type waveguides on LNOI substrates presented in section 4.3 a fabrication process was developed that is capable to realize plasmonic waveguides according to the designed parameters.

Plasmonics is an important research area since many years. By using localized plasmonic resonances of metallic nanostructures, an electromagnetic field can be strongly confined to a very small volume. In this way, light can be localized far below the classical diffraction limit enabling nanoscale integration of future optical devices[295]. In addition to that, the confinement can also be used to enhance nonlinear optical effects[296], [297]. Especially plasmonic waveguides with a nonlinear dielectric core can be used to exploit this enhancement. Using LiNbO_3 for this kind of application always poses the problem of phase-

matching of the nonlinear conversion processes. Phase-matching can be done either by QPM or, more efficiently, by exploiting the modal dispersion of the interacting waveguide modes in the same way as it was introduced in the previous chapter[21], [242], [298]. A well-established representation of such a structure is the metallic slot waveguide[299] with the slot filled with LiNbO_3 . An experimental realization of this waveguide could have great potential for the parametric amplification of a weak low frequency mode using a strong high-frequency signal at the SH. In this way, the usually short propagation lengths of plasmonic waveguides can be further extended, although the damping may not be fully compensated.

A theoretical study of the described metallic slot waveguides operated at NIR wavelengths around $1.55 \mu\text{m}$ was reported for silver and LiNbO_3 [294]. The technological most relevant configuration is where the fundamental mode of the FH interacts with the second order mode of the SH. The phase-matching condition in this configuration is quite tolerant against variations of the slot size. Furthermore, it was found that LiNbO_3 waveguides with widths of 150 to 200 nm and a height of 400 to 500 nm would be sufficient to show the expected effects. The thickness of the metal at each side of the waveguide should exceed the skin depth of the optical field and, consequently, be several tenths of nanometers.

It was outlined in the previous sections how nanowaveguides can be fabricated from LNOI substrates. Starting from these waveguides, which constitute the dielectric core of the final structure, a patterning scheme for the realization of nonlinear plasmonic slot waveguides was developed. The plasmonic properties were added to the dielectric ridge waveguide by metallization of the waveguide side walls. To allow for the fast development of a suitable structuring process, the patterning was done with ridge waveguides that were prototyped using FIB. Furthermore and also without loss of generality, the metallization was done with gold instead of silver for the first set of samples.

The sample preparation started with the evaporation of a 50 nm thick layer of carbon on a LNOI sample for charge dissipation during FIB milling. Using FIB patterning, a set of trenches was milled in the top LiNbO_3 layer, where the remaining LiNbO_3 ridges between the trenches form the waveguides. In terms of precision and the achievable minimum width, the previously presented approach using IBEE would have been superior. FIB patterning results in rounding of the leading edges of the structure, which are the top edges of the ridge in the given structure. This effect can be reduced by deposition of a sacrificial material with low sputtering yield, such as carbon, on top of the actual structure. The waveguides under investigation had widths of ~ 300 nm. The metal deposition was done by directional sputtering

under oblique incident. The incidence angle was determined by the geometry of the trenches adjacent to the LiNbO_3 ridge and amounted to 10° . In this way, 50 nm thick layers of gold were deposited on each sidewall. Because of the inclined deposition a closed gold film with a thickness below 10 nm covered the entire sample. This remaining gold film was subsequently removed by IBE. Here again, the carbon film proved to be beneficial, because it acted as an etching stop. In this way, the carbon layer prevented over-etching and surface corrugations in the LiNbO_3 ridge. Eventually, the carbon layer was removed by oxygen plasma etching, thus, concluding the processing. The resulting structure is shown in Figure 32.

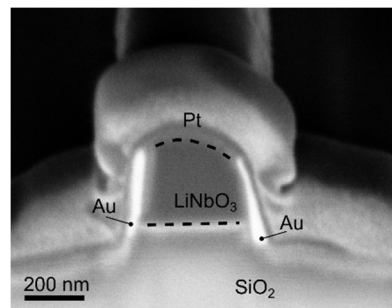


Figure 32: Scanning electron microscope image of the cross-section of a LiNbO_3 nanowaveguide with metalized side walls.

In order to evaluate the structure for optical characterization experiments, the plasmonic slot waveguides were fabricated on top of a larger mesa ridge cut in the LNOI substrates by circular saw dicing. These large ridges can be as narrow as $20\ \mu\text{m}$ and enable a direct transmission measurement through the waveguide, in principle. Generally though, it is outside of the scope of this section to provide further evidence for the optical functionality of the presented structures. The test setup to be used for this purpose has to be very elaborate. Furthermore, the results from such an experiment are foreseeably demanding to interpret without strong theoretical support. Nonetheless, the potential for further utilization of LiNbO_3 nanowaveguides in the ever growing field of plasmonics became evident from the presented results.

Chapter summary

In this chapter, the fabrication and optical characterization of different types of LiNbO_3 waveguides is presented. All of these waveguides were designed to confine the propagating optical modes to sub- μm size, which is beneficial for efficient modally phase-matched SHG and for a highly integrated optical devices. For local light delivery in biological imaging

applications, freestanding waveguides with width down to 50 nm were realized by IBEE in bulk LiNbO_3 substrates. Also, small ridge waveguides, which can be used for nonlinear integrated optics, were patterned by KOH based IBEE at the LNOI substrate surface. Both waveguide types were optically characterized and showed efficient SHG. Furthermore, a conceptually different type of nanoscale waveguide, which is based on photonic crystals, was presented. The fabricated structure was a W1 photonic crystal waveguide patterned by IBEE in bulk LiNbO_3 substrates. The waveguide underwent an extensive characterization of its linear optical properties. Using optical near-field imaging, the Bloch wave vectors and the transmission spectrum of such a waveguide was investigated. The experimental data showed good agreement with elaborate simulations, which is a basic prerequisite for designing more complex photonic crystal structures like the resonators presented in chapter 5. The last waveguide type presented in this chapter can be considered a continuation of the initial ridge waveguide study with the addition of metallized sidewalls. In this way, a metallic slot waveguide with nonlinear core was generated that could be used to parametrically amplify propagating plasmonic waveguide modes. In summary, this chapter demonstrated the successful implementation of different methods for the nanoscale confinement of propagating optical modes in LiNbO_3 , as well as the verification of their basic optical properties.

5 Linear and nonlinear optical properties of microsized resonators

Microsized optical resonators can be used for the concentration of light to a very small mode volume where nonlinear optical effects can be enhanced significantly. In this chapter, several resonator configurations will be presented. In the beginning, comparatively large microdisk resonators will be shown followed by photonic crystal based resonator designs which allow for a mode field confinement on the order of a single wavelength.

5.1 Microdisk resonators

In this section, the realization of microdisk resonators based on LNOI substrates and their initial optical testing will be discussed. In general, microdisk resonators can have very high Q factors and, consequently, can be used for a broad range of applications[300], [301].

With the focus on the enhancement of nonlinear optical processes many different materials, such as diamond[302], GaN[303], GaAs[304], Si[305], SiN[306], SiO₂[307] have been used as a substrate for microdisk resonators successfully. It has already been discussed that, for certain applications, the optical properties of LiNbO₃ make it superior to other materials and also a suitable choice for the realization of microdisk resonators. Of particular interest for this work are only such structures that have been fabricated by planar microstructuring technologies, which particularly excludes polished LiNbO₃ microdisk resonators[61].

It is the aim of this section to demonstrate high-Q factor LiNbO₃ microdisk resonators based on LNOI substrates. The presented structures were fabricated by means of FIB writing. A possibly more suitable approach in terms of resolution and pattern quality would be EBL with subsequent IBEE. However, FIB was chosen because the minimum sample size required for resist coating for EBL is much larger than the area needed for single microdisk resonators. In addition to that, pre-patterned substrates, such as diced platforms, can be patterned directly using FIB. In this way, the process is simplified, turnaround times are short and the substrate material is economically used. Nonetheless, the process can be easily adapted to EBL and IBEE patterning.

The realization of microdisk resonators is illustrated in Figure 33. The top LiNbO₃ layer of z-cut LNOI substrate had a thickness of 510 nm. Using circular dicing a chip of 1 mm by 2 mm

has been cut. The chip had a diced ridge with a width of approximately $100\ \mu\text{m}$. The ridge was formed by successive dicing of narrowly spaced trenches until all material around it was removed. For charge compensation during FIB milling, a layer of carbon was evaporated on the sample. Subsequently, the substrate was patterned with the FIB (Zeiss, CrossBeam NEON60) in connection with the lithography system (Raith ELPHY Quantum). The patterned layout consisted of a ring with a line width of $1\ \mu\text{m}$ and diameter of $39.5\ \mu\text{m}$, where the area enclosed by the ring became the microdisk in the end. The area outside the ring was dissected by cutting trenches in the top LiNbO_3 layer of the substrate. The resulting surface pieces are small enough to be completely underetched and washed away by the etchant during the following wet etching. The patterns were cut down to the SiO_2 layer so that it was selectively removed by the SiO_2 etching solution (ammonium fluoride – HF mixture). The etch time was 10 min during which the etchant container was placed in a water bath with a temperature of 50°C . The final process step was oxygen plasma cleaning for 15 min to remove the conductive carbon layer from the sample surface. A SEM image of the resulting disk is shown in Figure 33.

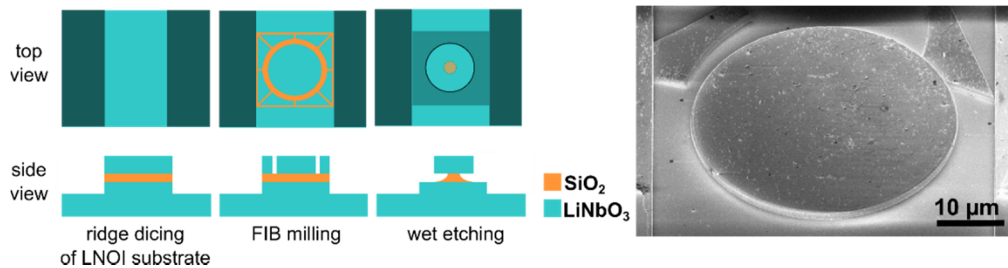


Figure 33: Schematic of the fabrication of LiNbO_3 microdisk resonators in LNOI substrate and scanning electron microscope image of the resulting disk with remaining detached LiNbO_3 pieces.

The following optical characterization was done using a tapered optical fiber. The tapered fiber was produced from a SMF 28 fiber with an outer diameter of $125\ \mu\text{m}$ and a core diameter of $9\ \mu\text{m}$ by heating and pulling until a thickness of around $1\ \mu\text{m}$ was reached. Since a tapered fiber bent into a U-shape was still available, it has been used throughout these experiments. Nonetheless, the geometry of the sample chip having a ridge with the microdisk on top was intended for the use of a straight tapered fiber that could be positioned orthogonal to this ridge and close to the microdisk. The positioning of the bent fiber taper close to the disk was monitored by a microscope from the top to ensure good coupling. The coupling efficiency between the resonator mode and the guided cladding mode of the tapered fiber depends on the spatial mode overlap controlled by the positioning. It also depends on the resonance condition of the resonator modes, which is controlled by tuning the wavelength of

the incoupled light. To this end, the tapered fiber was connected to a tunable cw, NIR laser source. The laser wavelength was continuously tuned between 1520 and 1570 nm. The signal that is transmitted through the fiber was recorded using a photodetector. A section of the resulting spectrum is presented in Figure 34(a). It shows a large number of resonance peaks that correspond to various whispering-gallery modes.

The position of these modes in the spectrum can be theoretically verified using an analytical model. The membrane that is used for patterning the microdisk is thin enough to be a single mode planar waveguide. The modes, therefore, can be described in a two-dimensional approximation using an effective refractive index of the planar waveguide[289]. The resonator supports modes of $TE_{n,m}$ and $TM_{n,m}$ polarization, which are characterized by a radial n and azimuthal m mode number. The numbers correspond to the number of nodes of the field along radial and azimuthal direction. The resonance positions for the first four radial modes have been calculated in the experimentally tested wavelength range and are indicated in the plot in Figure 34(a) by dashed lines. Good agreement was found for the TE modes, while some of the TM modes could not be reproduced. Also, a number of other resonance peaks are present that could be attributed to higher order membrane modes which have not been considered in the calculation. The missing TM modes are due to the imperfectly matched coupling of the tapered fiber to the disk. In conclusion, however, it can be stated that the presented resonator shows a spectral response that can be well described by commonly used theoretical methods.

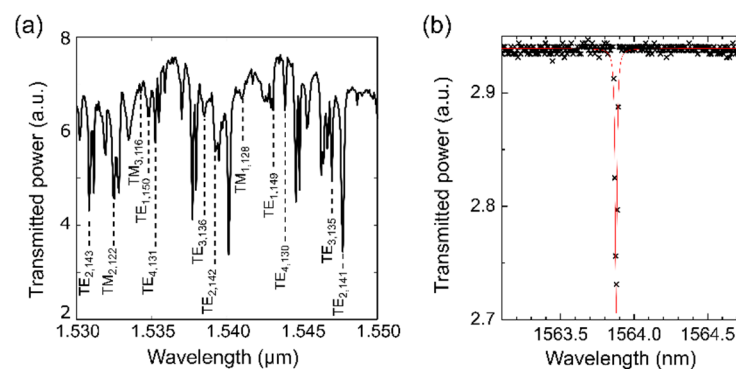


Figure 34: (a) Transmission spectrum of a LiNbO_3 microdisk with a diameter of $39.5 \mu\text{m}$. (b) Resonance peak of a microdisk with a diameter of $19 \mu\text{m}$ having a Q factor of 105,000.

In order to use microdisk resonators for enhancement of nonlinear effects, high Q factors are usually needed. Using another microdisk having a diameter of $19 \mu\text{m}$ and a height of 520 nm , we found a resonance located at 1563.9 nm with a Q factor of 105,000, see Figure 34(b). To exploit the nonlinear optical properties of the microdisk resonator, further numerical

modelling was conducted. It was found that modal phase-matching for SHG can be achieved for a disk thickness of 520 nm and diameter of 23.4 μm . In this configuration, a TE mode at 1550 nm and the corresponding TM mode at 775 nm are spectrally overlapping and are possessing the same effective refractive index. The spatial overlap, on the other hand, is not optimized and might limit the conversion efficiency since the interacting modes differ by two radial mode orders. The experimental characterization of SHG in the disk is challenging, because the tapered fiber coupling is not optimized for the SHG wavelength. Therefore, in an initial attempt, it was not possible to reliably detect SHG from the disk through the tapered fiber. However, it was reported for a similar microdisk setup that SH generated from an NIR source has been measured through the same fiber[42].

Nonetheless, it can be concluded positively that the linear optical properties of the fabricated microdisk resonators are at least as well as the ones reported recently[42], [71], [160]. Taking into account the result from the previous chapter 4 about nanoscale ridge waveguides fabricated from LNOI substrates, it can further be concluded that the microdisk geometry can be easily transferred to a lithography based patterning approach. The successful experimental characterization of microdisk resonator along with IBEE patterning gives rise to the realization of much more evolved integrated optical circuit designs.

5.2 Photonic crystal waveguide cavities

In this section, the realization of a microsized resonator based on a photonic crystal is introduced. The sample layout and the approach for optical characterization can be regarded as a continuation of the investigation of photonic crystal line defects[287] which have been reported in the previous chapter 4.

Microcavities in a nonlinear medium such as LiNbO_3 can be used for different optical devices allowing for SHG or optical parametric oscillation. The basis for the resonator presented here was a theoretical study about a microsized optical parametric oscillator based on a photonic crystal waveguide patterned in a freely suspended LiNbO_3 membrane[280]. The structure combines a two-dimensional photonic bandgap with waveguiding in vertical direction provided by the membrane. In this way, a confinement of the optical modes in three dimensions can be reached. In order to realize high-Q resonators in photonic crystal slabs, even in low-refractive index substrates such as LiNbO_3 , a design rule was proposed[308]. The shape of the electric field distribution inside the cavity should slowly vary, ideally resembling

a Gaussian function. In this way, out-of-plane losses could be minimized. According to these findings, a photonic crystal waveguide was modified by adiabatically changing the diameter of the holes in the rows adjacent to the line defect. The actual point defect that was enclosed by the modified holes had lengths of $N=4$ to 6 periods. A schematic of the structure is shown in Figure 35.

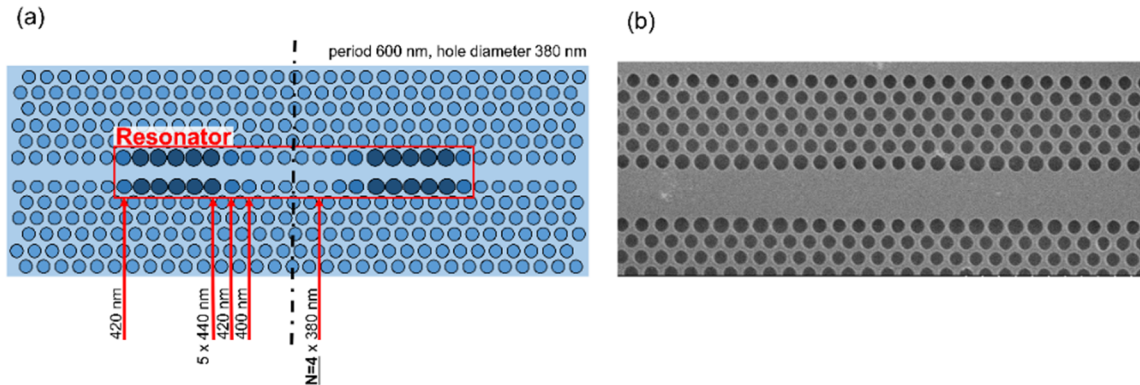


Figure 35: (a) Schematic of a W1 photonic crystal waveguide resonator. (b) Scanning electron microscope image of a LiNbO₃ membrane with a W3 photonic crystal waveguide resonator having a length of $N=4$ and a period of 600 nm.

The initial design proposal for this type of structure was aiming for a resonance located around 1550 nm with a relatively high Q . According to first theoretical estimations for a W1 photonic crystal waveguide resonator with dimensions according to Figure 35, a Q of ~ 800 is expected. In the case of a W3 waveguide resonator of similar layout a Q of ~ 280 is expected. The photonic crystal resonator structures have been fabricated by the same process used for the unperturbed photonic crystal waveguides described in the previous chapter and illustrated in Figure 18. A chip of 15x15 mm x-cut LiNbO₃ has been diced and layers of SiO₂ (1 μm) and chromium (80 nm) have been deposited. During the following EBL the photonic crystal patterns have been written in a layer of resist. The pattern was transferred first into the Cr and then through the chromium into the SiO₂ by standard dry etching. The resulting patterned layer acted as a mask during the subsequent irradiations with argon ions ion (60, 150, 350 keV at fluences of $0.92 \cdot 10^{14} \text{ cm}^{-2}$ and 700 keV at $4.8 \cdot 10^{14} \text{ cm}^{-2}$). The energies and fluences of the argon ion irradiations were adjusted to homogeneously damage the LiNbO₃ crystal to a depth of 450 nm. Starting at this depth, a layer of 500 nm thickness was damaged by a helium ion irradiation (285 keV and a fluence of $5 \cdot 10^{16} \text{ cm}^{-2}$ at 100 K). Prior the helium ion irradiation, the masking layer was removed. The sample was then heated at 300°C for 30 min and etched in HF (4%, 40°C) until the patterned membrane was formed. In the end,

the sample was thermally annealed at 500°C for 1 h to completely restore the original crystalline structure. An SEM image of the final structure is shown in Figure 35.

For the experimental characterization of the resonators, the most obvious scheme, where light is coupled in and out of the waveguide, could not be used. The waveguides are intrinsically lossy which made efficient light delivery to the resonant structure in the waveguide a limiting factor. This problem could be avoided by substantial shortening of the waveguide. At the time, when the presented structures were investigated, a suitable dicing technology was not available. Therefore, the initial optical characterization was approached differently by using the same tapered fiber coupling setup that was used for the microdisk resonator characterization. Since the tested structures were not elevated with respect to the surrounding sample surface, a straight tapered fiber that was oriented parallel to this surface could not be used. Instead, a fiber loop was employed. The looped fiber acted as a microscopic probe that can be positioned across the sample surface. It was fabricated by heating and pulling the fiber to form a tapered region of $\sim 1.3 \mu\text{m}$ diameter. After the fiber was pulled, one end of the fiber was rotated which caused a twisting in the tapered region and the formation of a loop with a diameter below 1 mm. The apex of the loop was aligned to be in close proximity to or in contact with the position of the resonator structure in the waveguide. The alignment was controlled by a microscope from the top. The fiber was connected to a cw laser source that was continuously tuned in the NIR wavelength range. The reflected and the transmitted optical signals at each end of the tapered fiber were recorded. Although the polarization in the fiber could be controlled by the respective fiber optic components, the actual polarization state at the resonant structure remained undefined. The polarization was adjusted such that a clear resonance peak was observed. An example of a recorded spectrum from a W3 waveguide resonator with $N=4$ is given in Figure 36. A very broad resonance ($Q=111$) was observed near the anticipated spectral position at 1542 nm. A similar behavior was expected for the W1 waveguide resonator, but it could not be verified experimentally. Generally, the characterization with a tapered fiber is not precise enough leading to an undefined coupling between tapered fiber and resonator. This is possibly caused by the inaccurate positioning of the fiber loop (distance from the surface, orientation along the waveguide) and, consequently, insufficient phase-matching between the resonators and fibers optical modes. Therefore, another approach was chosen to complement the findings, particularly for the W1 waveguide resonator. Light was coupled in the waveguide through a lensed fiber at the polished input facet. Similar to the characterization of the plain photonic crystal waveguide, a SNOM

recorded the optical near-field around the resonator for different wavelengths. The dielectric SNOM tip was then used to locally collect light scattered from the resonator while the wavelength of the incoupled light was tuned. In this way, transmission spectra (see Figure 26) of the resonator were recorded for a W1 waveguide with $N=6$. A resonance at 1529 nm with a Q factor of 380 was found. From the theoretical and experimental findings it can be concluded that the proposed waveguide resonator design, although functioning, has certain systematic drawbacks that may impede a complete characterization of the linear and nonlinear optical properties. These drawbacks are especially related to the undefined or inefficient coupling of the various “optical probes” to the resonator mode: the coupling between tapered fiber and waveguide was not well-defined, the vertical light emission for the inspection from the top was inefficient and the originally intended measurement through the photonic crystal waveguide was complicated by its inherently high losses. Based on these findings, a continued theoretical study to find further optimized geometries seemed unnecessary. Instead, a new resonator design was used, which accounted for the solution of the aforementioned shortcomings and which is the subject of the following section.

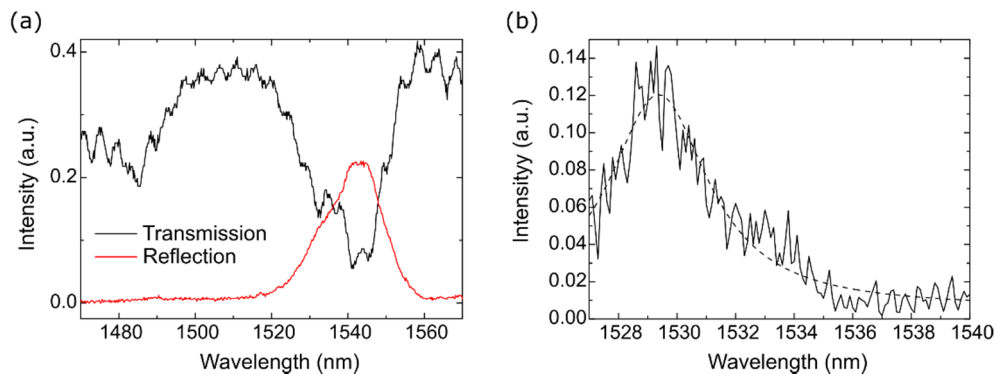


Figure 36: (a) Transmission and reflection spectra from a looped tapered optical fiber placed on a W3 photonic crystal waveguide resonator ($N=4$), the resonance is located at 1542 nm with a Q factor of 111. (b) Spectrum of scattered light from a W1 photonic crystal waveguide resonator ($N=6$) collected through a dielectric SNOM tip, the resonance is located at 1529 nm with a Q factor of 380 (solid line: experimental data, dashed line: Lorentzian fit).

5.3 Photonic crystal L3 cavities

In this section, the design, fabrication and characterization of L3 photonic crystals is presented. The sample layout was developed based on the findings from the previous section. It has been optimized for simplified experimental characterization of the optical function. The respective samples were fabricated by FIB milling in both, LNOI substrates and helium ion

irradiated LiNbO₃. The final optical characterization was done using cross polarized resonant scattering and second harmonic generation detection.

5.3.1 Design considerations

The general design idea is to have a small volume structure that strongly confines an optical mode with a large Q factor[308]. This can be achieved, for example, by a point like defect in a 2D photonic crystal patterned in a slab with a thickness in the order of the wavelength. In such a configuration, the light is confined in the vertical direction by waveguiding in the slab and horizontally by the 2D photonic bandgap[309], [310]. In an hexagonal lattice, this can be done by omitting few holes along the Γ K-direction. In this work, usually three holes are omitted constituting an L3 cavity. In order to make such a cavity suitable for practical applications it needs a high Q factor and, at the same time, some means to efficiently couple light in and out. The fulfilment of both requirements demands certain modifications in the original layout which will be introduced in the following.

In order to increase the Q factor of the cavity, the losses need to be reduced. Considering the loss mechanisms in more detail, one finds that the spatial variation of the field distribution at the edges of the cavity requires a smooth transition instead of a sudden jump. It has been demonstrated that a Gaussian field profile centered at the defect will drastically suppress radiation losses[308]. This can be achieved by modifying the layout of the photonic crystal areas next to the defect. The holes at the extremities of the defect are slightly shrunken and shifted away from the defect[308]. In this way, the condition for the Bragg reflection from the cavity edge is altered. This reflection is a result of many partial reflections from all interacting surfaces. When the position of these surfaces is changed, the partially reflected fields are slightly out of phase. The resulting electric field profile inside the cavity transitions smoothly into the surrounding photonic crystal resembling the required Gaussian shape[311]. The second requirement that needs to be fulfilled regards the efficient coupling of light in and out of the cavity. As was pointed out in the previous section, this is a difficult task because the modal field distribution of the cavity is strongly confined and does not sufficiently match with modes in optical fibers, test waveguides or even free space. It is therefore necessary to modify the photonic crystal structure to confine the cavity's radiation in the vertical direction in order to allow for efficient extraction with a microscope objective, for example. The respective modification can be deduced by examining how the near-field of the cavity mode in the reciprocal lattice is connected to its far field. Generally, radiation losses occur mostly for

fields having wavevectors that are situated above the light line. The far field emission, therefore, is governed by any near-field remnants above the light line. A photonic crystal cavity optimized for vertical emission requires a near-field distribution that is as close as possible to the border of the Brillouin zone, $k_x = \pi/a$ where a is the period. By adding a pattern with twice the period of the original structure to the given photonic crystal, the near-field distribution is folded back with respect to $k_x = \pi/2a$. In this way, the original near-field is replicated at $k_x = 0$ leading to an enhanced vertical emission from the structure[311]. A schematic of the final structure is shown in Figure 37.

5.3.2 Photonic crystal L3 cavities from bulk LiNbO₃

Photonic crystal L3 cavities were fabricated from bulk LiNbO₃ by combining IBEE and FIB patterning. The process can be briefly summarized as follows. First, the LiNbO₃ substrates were irradiated by helium ions forming a damaged buried layer. Next, FIB is used to define a pattern at the LiNbO₃ surface reaching down to connect to the buried layer. In the final HF wet etching step, the ion-irradiation damaged layer is selectively removed through the patterned surface areas resulting in the formation of a freely suspended patterned membrane.

Implementation of an optimized cavity design for enhanced vertical emission

In order to allow for simple optical coupling to the fields inside an L3 cavity, the photonic crystal design needed to be optimized to attain predominant emission of light from the structure in the vertical direction. In the following, two cavity designs with [312] and without second lattice are presented. Both patterns will be compared regarding Q factor, field distribution and vertical emission.

The tested structure was an L3 cavity having its defect line oriented perpendicular to the z-axis of the x-cut LiNbO₃ substrate. The hexagonal air hole lattice had a period of 559 nm with hole radii of 165 nm. The Q factor of the fundamental cavity mode was increased by modifying the two holes at the extremity of the cavity. They were shifted away from the defect by 129 nm and their radii were reduced to 150 nm. The second lattice was introduced by enlarging the radius of the holes to 210 nm in the primary lattice at twice the period around the defect, see Figure 37 for an illustration and Figure 38 for an SEM image. The photonic crystal patterns were fabricated in a LiNbO₃ membrane of 425 nm thickness that was suspended 590 nm above the LiNbO₃ substrate. The patterning was done by FIB (Zeiss, CrossBeam NEON60) in connection with the lithography system (Raith ELPHY Quantum).

The photonic crystal pattern is surrounded by a U-shape frame which is necessary to reduce the mechanical stresses in the membrane after the final wet etching. The stresses originate from a volume expansion that was caused by the helium ion irradiation. When the irradiated layer is etched, partially damaged material remains at the bottom of the membrane causing mechanical stresses and bending, see Figure 38 (c). These stresses, however, can be completely removed by thermal annealing in the end.

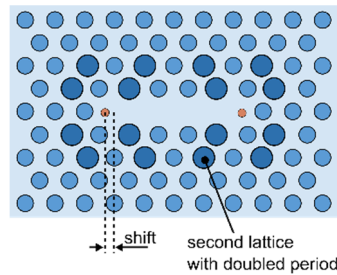


Figure 37: Schematic of L3 cavity with second lattice and shrunken, shifted holes in line with the defect.

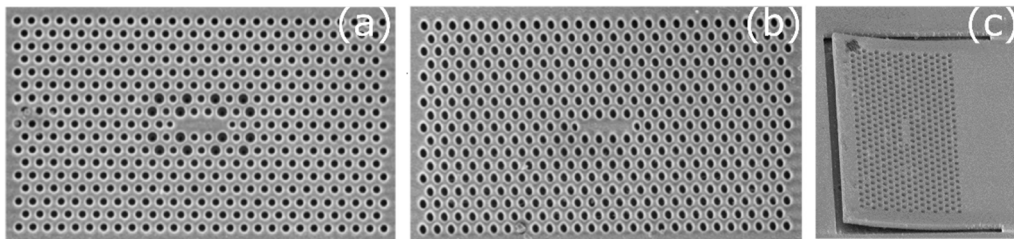


Figure 38: Scanning electron microscope images of an L3 cavity patterned in a helium ion irradiated LiNbO_3 substrate (a) with and (b) without second lattice. (c) Tilted view showing the framing structure around the deformed cavity directly after wet etching. (a)-(c) The period of the photonic crystals is 559 nm.

For two types of cavities (with and without second lattice), numerical simulations were conducted using the FDTD software MEEP[313] to find Q factors, resonance frequencies and field distributions of the first four TE-like cavity modes. The simulations included the three-dimensional geometry and the material anisotropy. The results are summarized in the following table together with the results from the experimental characterization of the cavities.

Mode number	Without second lattice			With second lattice		
	Resonance wavelength (μm)	Q -factor	Label	Resonance wavelength (μm)	Q -factor	Label
	calculated <i>measured</i>	calculated <i>measured</i>		calculated <i>measured</i>	calculated <i>measured</i>	
1	1.4407	1550	A	1.4052	775	a
	---	---		1.3906	535	
2	1.3684	130	B	1.3555	510	b
	1.3648	104		---	---	
3	1.3470	235	C	1.3415	125	c
	---	---		1.3440	122	
4	1.3376	143	D	1.3091	145	d
	---	---		1.3000	138	

The cavities were optically characterized by the cross-polarized resonant scattering method, as introduced in section 2.4.3 [314]. Polarized light from a tunable laser source was focused on the cavity by a microscope objective with a numerical aperture (NA) of 0.65. The polarization direction of the incident light was set up to be 45° with respect to the crystallographic y -axis of LiNbO_3 . The optical signal emitted back from the surface was collected by the same objective and recorded by an InGaAs detector as a function of the wavelength of the in-coupled light. The resulting spectra are shown in Figure 39, where each resonance peak was fitted with a Lorentzian function. In contrast to the simulation which was predicting at least four cavity modes with reasonable Q factor in the investigated spectral range, the experiment showed fewer resonances. This behavior is especially expected for the cavity without second lattice that is not optimized for enhanced vertical emission. To fully understand the experimental findings, the collection efficiency of the experimental setup was included in the simulation. The efficiency is limited by the NA of the microscope objective and translates to a maximum acceptance angle for the detection. By Fourier transformation of the electric and magnetic fields of the cavities calculated several nanometers above the surface, the angular dependencies of the radiated powers were quantified. These calculations also took into account the acceptance angle for detection which is determined by the overlap of the far field radiation of the cavity and the Gaussian field profile of the microscope objective. Figure 39 illustrates the results and shows the power that radiates into an angle that corresponds to the NA of the microscope objective for all considered modes. All the modes marked in the upper half of the plot were detected experimentally. The other modes with normalized radiation powers below 10% could not be measured because of insufficient sensitivity of the detection combined with inefficient in- and outcoupling of radiation. From these findings it can be concluded that small modifications of the geometry of the photonic crystal cavity are crucial for the Q factor and the vertical emission of the modes. In accordance with the preceding explanations about the means to enhance vertical emission, it was experimentally verified that adding a second lattice indeed leads to an improved coupling of light from the top to the fundamental cavity mode and to higher order cavity modes. This behavior was further supported by numerical results that agree well with the experimental results. A more elaborate comparison of the two cavities with and without second lattice considering especially the band folding effect and giving further details about computational results is presented in [315] and is outside the scope of this work.

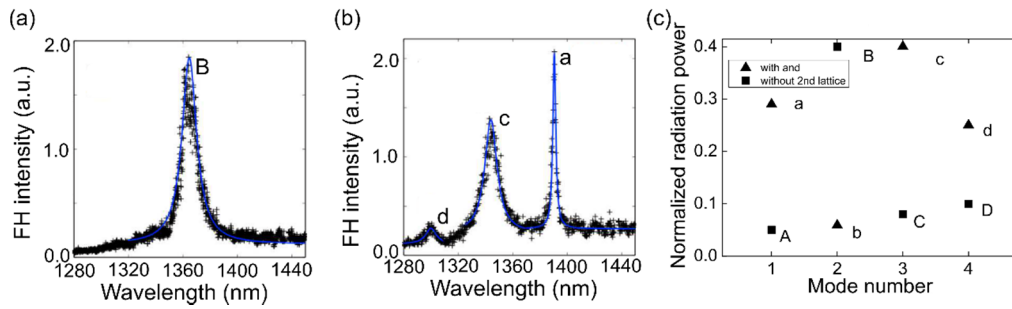


Figure 39: Reflected scattered FH intensity spectra measured with crossed polarizations for L3 cavities (a) with and (b) without second lattice. The blue lines are the Lorentzian functions fitted to the experimental data. (c) Calculated power radiating from the L3 cavity in an angle corresponding to an NA of 0.65. All peaks are labelled according to the table.

Characterization of nonlinear optical properties

In this section, experiments are discussed that probe the nonlinear optical properties of the previously introduced L3 cavity with the second lattice. All of the following experiments were done with the fundamental cavity mode (label a) only. According to the simulation results summarized in the preceding table, the resonance wavelength of the fundamental mode of this cavity should be at 1405.2 nm with a Q factor of 775, while the measured resonance peak was slightly different having a resonance wavelength of 1390.6 nm and a Q factor of 535. These minor differences can be explained by imperfections of the fabrication process. The influence of the second lattice can be observed from the calculated radiation intensity[309] shown in Figure 40. In the plot in Figure 40, the field distribution is normalized to the total radiation intensity in the upper and lower half spaces. The second lattice caused a concentration of the radiated fields in the center of the angular spectrum which corresponds to a vertical emission into a quite narrow cone. According to the calculations, a cone with an opening angle of 47° collected about 25% of the power radiated into the upper half space. The experimental characterization of the cavity was done using cross-polarized resonant scattering microscopy with a microscope objective having an NA of 0.65. The corresponding coupling efficiency to the mode inside the cavity can be calculated to be 29% for this configuration. From measuring the input signal, the cross-polarized reflected signal and considering the transmission of the optical setup, a coupling efficiency of 20% was estimated. The difference between both efficiency values can be attributed to imperfect overlap between the modes of the collection optics and the far field of the cavity.

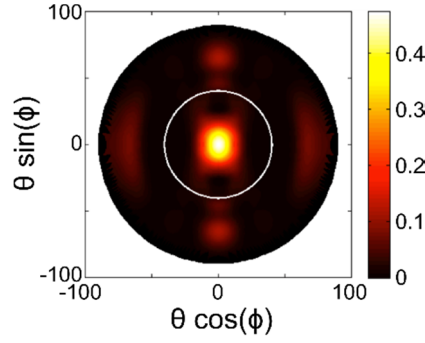


Figure 40: Calculated angular radiation intensity pattern $\kappa(\phi, \theta)$ of an L3 cavity with second lattice at the fundamental mode frequency. ϕ and θ are the azimuthal and polar angles, respectively. The white circle represents the maximum collection angle of a microscope objective with an NA of 0.65. (Figure from [316]: S. Diziain, R. Geiss et al., Appl. Phys. Lett. 103, 51117 (2013))

In order to study the nonlinear properties of the cavity, a dichroic mirror was inserted in the path of the back reflected light. The mirror reflected the SH signal and directed it to a silicon avalanche photodiode. To suppress any remaining FH signal, an additional filter was inserted in front of the detector. Spectra of the SH signals were recorded with the input field tuned around the FH fundamental mode resonance of the cavity and for three different polarization angles of the incident field (polarization parallel to y-axis with $\alpha=0^\circ$, parallel to x-axis with $\alpha=90^\circ$, and $\alpha=54^\circ$). The spectra are shown in Figure 41, they were normalized to the maximum photon count. The data was fitted with squared Lorentzian functions resulting in Q factors of ~ 480 for all measured peaks which is in good correspondence to the linear spectrum's Q factor. The SHG efficiencies, i.e. the measured peak intensity, showed a strong dependency on the polarization direction of the incident FH light. The SHG process is most efficient for a polarization parallel to the z-axis of LiNbO₃ (0°). The SH intensity can be expressed as follows

$$I_{\text{SH}} \sim (P_{\text{NL},x}^2 + P_{\text{NL},y}^2) (A \cos \alpha + B \sin \alpha)^4 \quad (15)$$

with $P_{\text{NL},x} = 2\varepsilon_0 d_{22} E_x^2 + 4\varepsilon_0 d_{31} E_x E_y$ and $P_{\text{NL},y} = 2\varepsilon_0 d_{31} E_x^2 + 4\varepsilon_0 d_{33} E_y^2$. The SH intensity is proportional to the polarization angle α and the squared second order nonlinear polarization. The nonlinear polarizations depend on the electric fields of the FH fundamental cavity mode, which are plotted in Figure 42. Although the x and y components of the electric field have a similar field strength, their emission behavior into the upper half space is very different. Both field distributions with the corresponding radiation patterns are plotted in Figure 42. The white circle indicates the microscope objectives' NA of 0.65. From these plots, it can be concluded that using this objective, 60% of the radiation from the upper half space having a y-

polarized electric field and only 8% having an x-polarized electric field can be detected. This relation eventually explains the strong polarization dependence of the measured SH signal.

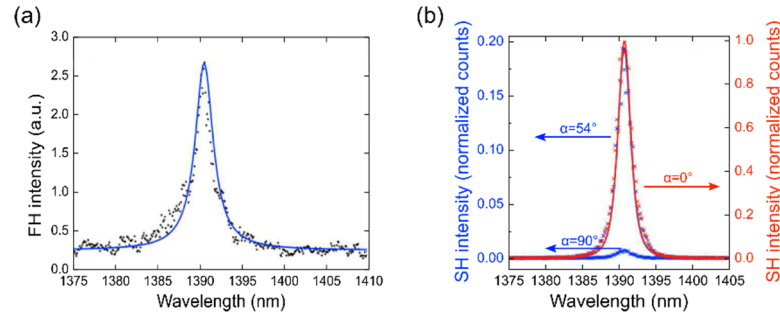


Figure 41: (a) Reflected scattered FH intensity spectra measured with crossed polarizations. (b) Generated SH as a function of the FH wavelength for different polarizations. The SH spectra are normalized to the maximum of the SH measured for $\alpha=0^\circ$ (parallel to the crystallographic y-axis of LiNbO_3). The solid lines are the Lorentzian and squared Lorentzian functions fitted to the experimental data.

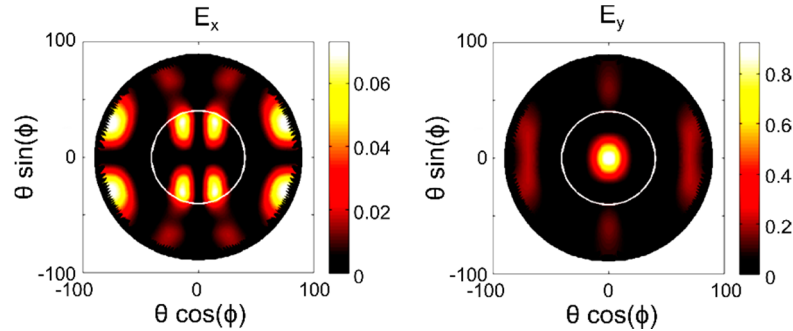


Figure 42: Angular radiation patterns of the x and y components of the electric field of the fundamental mode of an L3 cavity with a second lattice. The white circle represents the maximum collection angle of a microscope objective with an NA of 0.65. (Figure from [316]: S. Diziain, R. Geiss et al., *Appl. Phys. Lett.* 103, 51117 (2013))

The dependence of the SH signal on different polarization angles of the incident light was also tested. The results are plotted in Figure 43, where the data were fitted with the quartic term in (15). Furthermore, the dependence of the SH power on the FH power was tested at the resonance frequency of the cavity (1390.6 nm). The results are plotted in Figure 43, where the data was fitted with a quadratic function. The good correspondence between the fit function and the data proved that a nonlinear effect of second order has been observed.

The conversion efficiency of this process is defined as the ratio of SH power to coupled FH power. At a FH power of $53 \mu\text{W}$, the efficiency amounts to $6.4 \cdot 10^{-9}$, which should be considered a lower estimate since a significant amount of radiated SH was not collected by the microscope objective. Comparing to L3 photonic crystal cavities that were reported for other materials, the conversion efficiency found in this work seems reasonable. For example, a cavity made from GaP with a Q factor of 6,000 showed a conversion efficiency of $5 \cdot 10^{-5}$ at a

FH power of $11 \mu\text{W}$ [317], whereas a cavity from InP with a Q factor of 3,800 had a conversion efficiency of just $1 \cdot 10^{-13}$ at $300 \mu\text{W}$ coupled FH power [318]. The semiconductor substrates used in those works do not only have a higher refractive index than LiNbO_3 , which leads to better modal confinement and, therefore, higher Q factors, they also have larger second order susceptibilities. Any conclusion drawn from a quantitative comparison of the reported numbers therefore requires a careful interpretation.

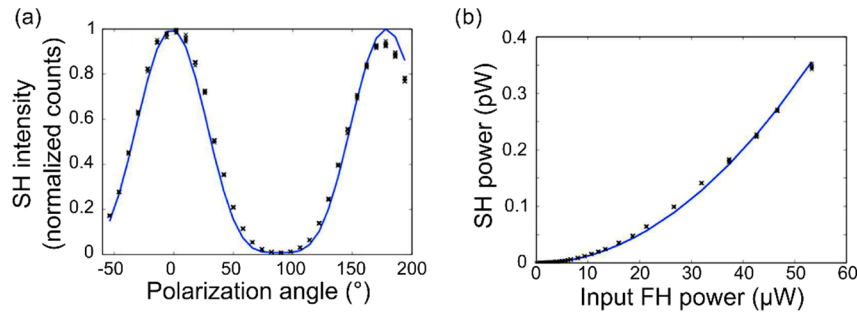


Figure 43: Generated SH at the fundamental mode resonance wavelengths plotted (a) as a function of the polarization angle of the input FH field and (b) as a function of the input FH power.

However, it can be concluded that SHG with ultra-low pump power was demonstrated in an L3 photonic crystal cavity patterned in a free-standing LiNbO_3 membrane. It was shown that a Q factor of 535 is already sufficient to allow for the enhancement of the SHG process. In order to improve the performance of the cavity, especially the conversion efficiency of the SHG, the photonic crystal design could be further optimized. Nonetheless, the presented results are, to the best of our knowledge, the first experimental demonstration of SHG in a LiNbO_3 photonic crystal resonator. This work clearly shows the great potential of microstructured devices fabricated on the basis of LiNbO_3 thin films for applications in non-linear optics.

5.3.3 Photonic crystal L3 cavities from LNOI substrates

The realization of L3 cavities in LNOI substrates follows the fabrication process that was used for microdisk resonators before. The LiNbO_3 layer at the top of a piece of z-cut LNOI substrate was thinned down to a thickness of 370 nm by means of IBE. It followed the patterning of the photonic crystal structure by FIB milling and selective wet etching of the SiO_2 underneath the LiNbO_3 layer at the top. In this way, similar to the helium ion irradiated substrates, free-standing patterned membranes were realized.

The defect of the L3 cavity was oriented along the crystallographic y -axis of LiNbO_3 . The lattice period was 530 nm with hole radii of 148 nm. To increase the Q factor, the holes at both ends of the defect were shrunk to a radius of 143 nm and shifted out by 122 nm. The vertical emission of the structure was enhanced by superimposing a second lattice with larger holes of 175 nm and twice the period. In this way, it was ensured that the TE-polarized fundamental cavity mode can be efficiently excited at normal incidence from the far field. A SEM image of the cavity is shown in Figure 44.

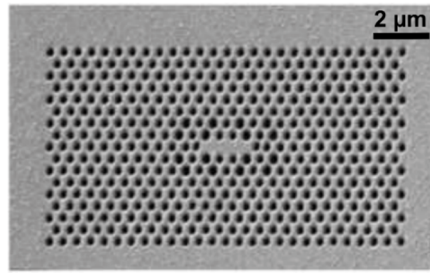


Figure 44: Scanning electron microscope image of an L3 cavity fabricated in z -cut LNOI substrate, the defect is oriented parallel to the crystallographic y -axis.

The optical properties of the cavity were characterized by cross-polarized resonant scattering microscopy. The setup allowed for detection of back-reflected light from the sample surface at FH and SH frequencies. Spectra that were recorded in the NIR wavelength range with an incident polarization of 45° with respect to the crystallographic axis are shown in Figure 45. A clear resonance peak was observed. Fitting the data with a Lorentzian function, the resonance wavelength was found to be 1356.0 nm with a width at half maximum of 2.0 nm corresponding to a Q factor of 678. These findings were compared with 3D-FDTD calculations that predict resonance wavelength of the fundamental cavity mode at 1362.8 nm with a Q factor of 1550.

In principle, the free standing geometry of the presented structures is not necessary for planar light confinement because the refractive index contrast between the SiO_2 layer and the LiNbO_3 membrane allows for sufficient guiding. For comparison, calculations were made for the presented structure where the SiO_2 film was still present resulting in a Q factor of only 245. The free standing geometry therefore is crucial to improve the mode confinement inside the photonic crystal defect and to increase the Q factor.

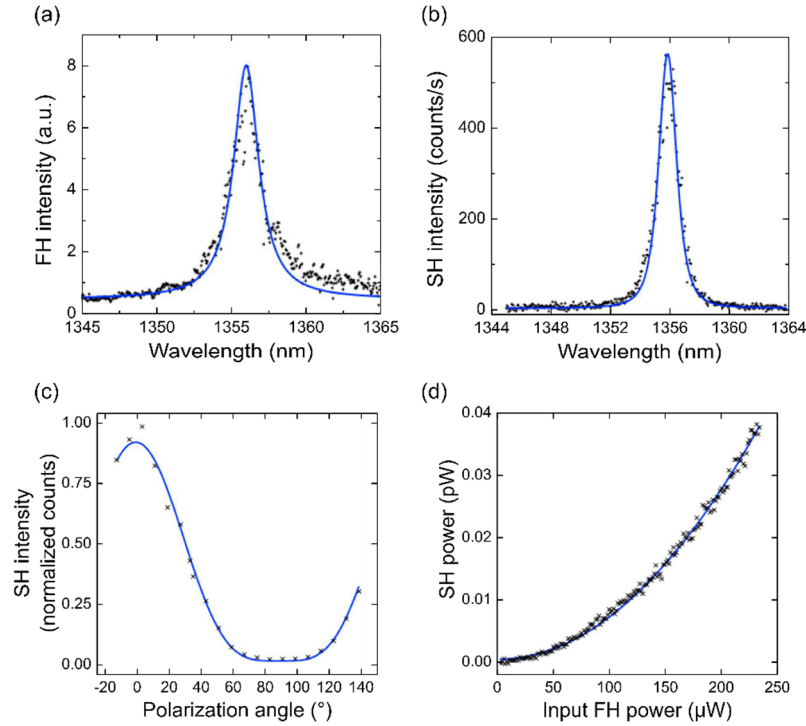


Figure 45: Optical characterization of L3 cavity fabricated from LNOI substrates. (a) Reflected scattered FH intensity spectra measured with crossed polarizations. (b) Generated SH as a function of the FH wavelength. (c, d) Generated SH at the fundamental mode resonance wavelength plotted (c) as a function of the polarization angle of the input FH field and (d) as a function of the input FH field power. Solid line: fit with (a) Lorentzian, (b) squared Lorentzian, (c) $\cos^4\alpha$ and (d) quadratic function. Crosses: (a-d) experimental data.

To study the nonlinear optical properties, the SH signal was recorded simultaneously with the linear signal at an incident polarization angle of 45° . The resulting spectra are shown in Figure 45(a, b). Fitting the data with a squared Lorentzian function yielded a resonance wavelength of 678 nm and a Q factor of 640 which is in good correspondence with the resonance properties of the FH fundamental cavity mode. The SH signal was further recorded as a function of the direction of the incidence polarization, see Figure 45(c). The data was well fitted with a $\cos^4\alpha$ function which is in good agreement with the anticipated radiation properties of the fundamental cavity resonance (see previous section). To give final proof that the observed SH signal originated from a second order nonlinear effect, the power dependence of the SH signal was measured. The data is presented in Figure 45(d). The expected quadratic increase of the SH signal as a function of the FH signal is clearly visible and confirmed by fitting a quadratic function. The conversion efficiency of the SHG from a z-cut LNOI membrane was lower than for membranes from bulk x-cut LiNbO_3 because the interaction of the electric field of the fundamental cavity mode could not be matched to the dominant components of the nonlinear susceptibility in the given crystal orientation of the LiNbO_3 substrate.

In summary, the linear and nonlinear optical properties of L3 photonic crystal cavities made from z-cut LNOI substrates have been studied. The results are in good agreement with the theoretical modelling. The performance of the fabricated structure is generally comparable to the structure fabricated from bulk LiNbO₃ substrates.

5.3.4 Concluding comparison of bulk LiNbO₃ and LNOI substrates for photonic crystal structures

In the last two sections, the design and fabrication of L3 resonators in membranes made from helium ion irradiated LiNbO₃ and LNOI substrates were presented. The optical properties of both structures were found to be comparable. Also in terms of patterning technology, both types of substrates have to be treated similarly. Nonetheless, LNOI offers certain advantages compared to helium ion irradiated samples. When using LNOI substrates, the height of the air gap between the LiNbO₃ layer at the top and substrate is governed by the thickness of the SiO₂ film. LNOI substrates are sold with SiO₂ thicknesses above 1 μm which is already enough to almost fully suppress losses that originate from coupling of light guided in the top LiNbO₃ layer to the substrate[180]. In case of the helium ion irradiated substrates, the height of the air gap is determined by the maximum energies supplied by the ion beam irradiation facility and is limited to about ~500 nm for this work. Although this air gap height is still sufficient to realize the proposed device functionalities, it always presents a source of additional losses[180]. The influence of the substrate therefore needs to be accounted for in the numerical modelling which further complicates the design process.

Another advantage of using LNOI substrates is the absence of mechanical stresses in the membranes. Patterned membranes that are fabricated in helium ion irradiated substrates have a tendency to bend because of the remaining irradiated material that was not removed by wet etching, which causes a slight volume expansion at the bottom of the membrane. Although these stresses can be removed from the crystal by thermal annealing, they need to be considered in the pattern layout otherwise the membrane will crack and destroy the structure. In the case of LNOI substrates, such measures are unnecessary which makes their patterning less complicated.

5.4 Nanobeam cavities

Nanobeam cavities are a conceptual continuation of the topic of nanoscale waveguides with the waveguides being periodically patterned along the propagation direction. Such a pattern can be regarded as a one-dimensional photonic crystal and it can be designed to allow for various optical functionalities, including optomechanics[319], single quantum dot coupling[320], lasing[321] and sensing[322]. Especially interesting in the context of this work is the interaction of the one-dimensional periodic pattern with the optical nonlinearity of LiNbO_3 which could be used, for example, to design the phase-matching condition of a nonlinear interaction. The introduction of a defect into these periodic patterns leads to the localization of light, representing a cavity[323]. A typical design is a suspended waveguide with a height of 475 nm and width of 710 nm. Along the waveguide, holes with a radius of 166 nm are arranged with a period of 593 nm, see Figure 46. The central hole is omitted and forms the defect. Similar to the two-dimensional design consideration discussed for the L3 cavity, the transition of the electric field of the cavity mode needs to be rather smooth in order to increase the Q factor[324]. It is also possible to superimpose a second lattice for enhanced vertical emission, although this may not be required for this type of cavity. These cavities could be conveniently integrated in ridge waveguides allowing simple access through standard fiber coupling techniques.

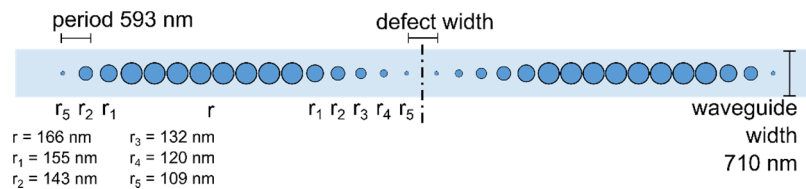


Figure 46: Schematic of nanobeam cavity for fabrication in a LiNbO_3 ridge.

During this work, an initial design for nanobeam cavities has been developed. According to this design, a set of samples was fabricated from bulk LiNbO_3 and LNOI substrates using direct FIB milling and subsequent wet etching. An SEM image of such a structure is shown in Figure 47. The dimensional accuracy is very good and the designed optical properties can be expected. However, the optical characterization of these samples has not been performed, yet.

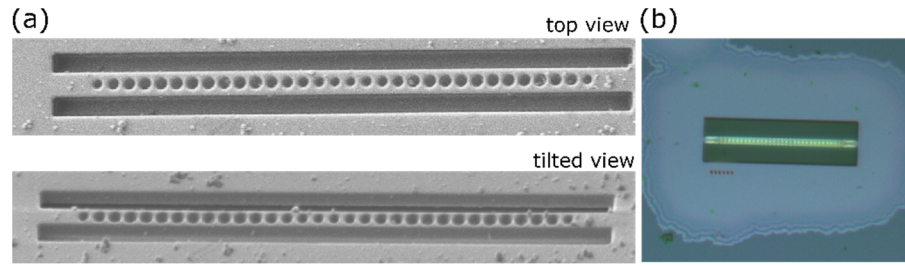


Figure 47: (a) Scanning electron and (b) optical microscope images of a LiNbO₃ nanobeam cavity made from LNOI substrates, the period is 593 nm. (b) The bright line in the center is the nanobeam cavity with the rectangular openings next to it, the underetched area is notably brighter than the unetched parts.

Chapter summary

In this chapter, several implementations of microsized optical resonators were presented including general design considerations, fabrication and optical characterization. While most parts of this chapter were dedicated to the study of photonic crystal based resonators, the chapter started with the introduction of the comparatively large microdisk resonators having diameters in the order of tens of micrometer. These microdisks were directly patterned by FIB in LNOI substrates. The optical characterization revealed Q factors as large as 100,000. Being the continuation of the photonic crystal waveguide structures presented in chapter 4, a waveguide resonator design was realized by IBEE in bulk LiNbO₃ substrates followed by the characterization of its linear optical properties. Subsequently, the photonic crystal design was further advanced to an L3 type of cavity which is optimized for higher Q factors and enhanced vertical emission to simplify the optical characterization. The respective patterning was done directly by FIB in LNOI and helium ion irradiated LiNbO₃ substrates. The resonators were optically characterized and showed efficient SHG. In the following section of this chapter, nanobeam cavities were presented. They consisted of a one-dimensional photonic crystal along a nanoscale ridge waveguide and were fabricated by FIB in LNOI substrates. In contrast to L3 cavities, their advantageous design generally allows for the direct integration in planar optical circuitry. It is common to all presented resonator configurations that a high dimensional accuracy is required in order to achieve high Q factors. In this chapter, an overview of several different implementations of microsized resonators along with their individual advantages and limitations was given, where particularly the performance of the L3 photonic crystal cavities was most promising. The results of the optical characterizations prove that the required accuracy has been achieved. This will be the basis for the design and

realization of more complex optical structures to strongly confine optical fields to small volumes for a highly efficient enhancement of nonlinear interaction processes.

6 Summary and conclusions

The intention of this thesis was the realization of micro and nanoscale optical elements made from LiNbO_3 for applications in integrated nonlinear optics. LiNbO_3 was chosen as substrate material because it is already well-established and widely used in this area. Following a trend of miniaturization, patterning techniques for LiNbO_3 are wanted that are compatible with modern micro and nanofabrication technologies. This condition is rather demanding because LiNbO_3 is chemically very stable and cannot be patterned by means of standard dry etching with sufficient quality.

In this regard, extensive studies about general ion beam irradiation induced effects in LiNbO_3 and particularly about structuring of LiNbO_3 by ion beam enhanced etching (IBEE) have been conducted at the Institute of Applied Physics of the University Jena by others, before this thesis work was commenced. It was the aim of this thesis to resume and further advance these studies and to apply the results to the patterning of LiNbO_3 . For this purpose, basic optical elements were identified and designed for fabrication and optical characterization. It is common to all these elements that they rely on planar waveguiding structures with a lateral pattern being specific to the respective optical function. The planar waveguiding can be realized using LiNbO_3 membranes from either helium ion irradiated bulk LiNbO_3 substrates or commercially available lithium-niobate on insulator (LNOI) substrates. Generally, LNOI offers many advantages compared to the helium ion irradiated substrates which makes it a convenient basis for many targeted application. Nonetheless, because LNOI contains a SiO_2 layer, it is not fully compatible with the established HF based IBEE process. A large portion of this thesis therefore was devoted to the study of the etching of ion beam irradiated LiNbO_3 in different wet etching solutions. The experimental investigation of the underlying etching mechanism eventually led to the development of new processes suitable for the patterning of LiNbO_3 and LNOI. Amongst other hydroxide based etchants, KOH was found to be the most suitable alternative for HF in the IBEE process. Especially the dependence of the etch rate on the normalized fluence of the ion irradiation showed a selectivity which is similar to the HF based IBEE and which makes the effect applicable to nano and microfabrication.

IBEE based processing is generally useful for lithography based patterning tasks. In situations where short processing times are needed and large area patterning is unnecessary, focused ion beam (FIB) milling is a valuable tool. Lots of the patterning tasks that are covered by IBEE could be transferred to or combined with direct FIB patterning. In this way, predefined

membrane substrates (LNOI or helium ion irradiated LiNbO_3) have been patterned at the surface by FIB and subsequently underetched by a suitable etchant. For the patterning tasks involved in this thesis, a gallium ion FIB process was developed. Particularly the influence of gallium ion contaminations in LiNbO_3 after FIB milling on the dimensional accuracy of the structures was investigated and considered in the final process.

It can be summarized that the experimental studies about ion beam induced effects on LiNbO_3 etching, which represent an essential part of this thesis, resulted in the development of a set of novel, well adapted patterning processes. The remaining part of this thesis is based on these processes which enable the realization of the targeted nano and micro sized integrated optical elements. These elements were designed to strongly confine either propagating optical modes in waveguides or resonator modes in optical cavities. Conceptually, the efficiency of nonlinear interaction processes in waveguides and in resonators can be significantly enhanced compared to bulk processes which is beneficial for their general usability.

In order to experimentally verify the anticipated enhancement in the beginning, wire-type LiNbO_3 waveguides were designed and fabricated. The dimensions of the waveguides were chosen to enable phase-matching using the modal dispersion of the propagating fundamental harmonic (FH) and second harmonic (SH) fields. To this end, two different kind of wire-type waveguides were fabricated.

The first kind of waveguide was freely suspended and completely underetched. A large number of these waveguide types was patterned by electron-beam lithography (EBL) and was transferred into the bulk LiNbO_3 substrate by HF based IBEE. The IBEE process included a helium ion irradiation which was responsible for the formation of an air gap underneath the final wire-type waveguides. The resulting waveguides were several micrometer long with widths down to 50 nm. A complete simulation of the ion irradiation and etching processes enabled the prediction of the final cross-sectional shape of the waveguide, which added a new degree of freedom to the optical design. For the optical characterization, the waveguides were detached from the LiNbO_3 substrate by sonication in a fluid and pipetted on a neutral glass substrate. The optical characterization of the waveguides showed efficient second harmonic generation (SHG) from a FH pump with ~ 800 nm wavelength. Because the fabrication process is based on EBL, it allowed for the patterning of very large areas of well-defined waveguides. When the waveguides are suspended in a liquid they can be considered a deterministic counterpart of chemically synthesized LiNbO_3 nanowires. Such chemically synthesized nanowires have been used already for imaging applications in biology for local

light conversion and delivery. The fabricated deterministic wire-type waveguides can be potentially used in a similar way. The SHG intensity of the waveguides was sufficient for fluorescence excitation of dyes with FH intensities below the cell damage threshold, which is required for the successful application in biology. In summary, the waveguide's fabrication and optical functionality were investigated, showing the expected nonlinear optical properties. The freestanding geometry through the helium ion irradiation was necessary to achieve planar light guiding. The arrangement and handling of the waveguides proved to be beneficial particularly for the potential exploitation of applications in biology. Nonetheless, with respect to integrated optics further ridge waveguide designs incorporating LNOI were advanced additionally.

This second type of waveguides was also fabricated by EBL and KOH based IBEE on LNOI substrates. In contrast to the previous design, the LNOI waveguides remained attached to the substrate surface. The planar waveguiding was accomplished by the refractive index contrast between the patterned top LiNbO_3 layer and the underlying SiO_2 layer. In this way, waveguides with width down to 200 nm were realized and optically characterized, showing efficient phase-matched SHG.

In order to add more degrees of freedom to the relatively simple ridge waveguide, photonic crystal based waveguide designs have been investigated for potential improvements and future applications like slow light enhancement of nonlinear effects or light localization. In particular, a W1 photonic crystal waveguide was fabricated by EBL and HF based IBEE in a freestanding LiNbO_3 membrane. From the experimentally obtained optical near-field images of the waveguide, Bloch wave vectors were identified and a transmission spectrum was retrieved. The experimentally studied linear properties of these waveguides corresponded well to numerical results which is promising for the development of more advanced photonic crystal based structures, such as resonators.

Consequently, based on a W1 photonic crystal waveguide, a resonator was designed by adiabatically changing the hole diameters adjacent to the line defect. The resonator was fabricated by EBL and HF based IBEE. The optical characterization confirmed the designed linear optical properties. Nonetheless, the general device geometry led to inherently high losses which complicated the optical characterization as well as the potential integration of the resonator in an integrated optical circuit. Therefore, a photonic crystal L3 cavity was designed having a higher quality factor and an enhanced vertical emission. In this way, the light scattered from the cavity is confined in a narrow cone which can be collected efficiently from

the top using a microscope objective. These optimized L3 cavities were fabricated using FIB in both, helium ion irradiated LiNbO₃ and LNOI. The optical characterization using a cross polarized scattering microscope demonstrated efficient SHG at the cavities resonance frequency. Furthermore, numerical studies of the linear modal properties were conducted and experimentally verified. In summary, the presented L3 cavities proved to be useful resonator structures for the investigation of nonlinear optical effects. With respect to applications in integrated optics, the cavity design could be further advanced by patterning a one-dimensional photonic crystal in a wire type waveguide, forming a nanobeam cavity. Compared to other designs, significantly higher quality factors are expected from these structures. An initial design was realized by FIB in an LNOI substrate in order to prove the general feasibility of the proposed nanobeam cavity. These cavities will be further investigated experimentally and theoretically in the future. Aside from photonic crystal based resonators, also a more established resonator design was realized in this thesis. Microdisk resonators with diameters of several tens of micrometers were patterned in LNOI substrates by FIB. Their optical characterization yielded quality factors that are comparable to the reported state of the art.

In conclusion, a number of nano and microstructured optical elements in LiNbO₃ have been realized. While some of these elements were merely proving concepts of preliminary theoretical work, most of the elements underwent a full optical characterization that verified their designed optical properties. The presented structures provide numerous functionalities that are beneficial for their use as basic building blocks in future nonlinear integrated optical circuits. In the course of this thesis, a comprehensive investigation of the individual elements was conducted. It is the task of ongoing research to combine these elements with each other or to identify means to integrate them in commonly used photonic platforms such as silicon. With respect to the patterning of LiNbO₃, the important field of domain engineering of the LiNbO₃ crystal has not yet been incorporated in the presented processes. Since the presented optical elements have typical dimensions of only few micrometers, classical electric field poling of coarse domain patterns with dimensions down to 10 μm and poling depths of several 100 μm should be replaced by processes suitable for sub- μm domain sizes. Future research shall hence be devoted to the investigation of process like direct surface poling of LiNbO₃ membrane substrates to add another degree of freedom to the design process and the overall functionality of future devices.

List of abbreviations

AFM	Atomic force microscope
APE	Annealed proton exchange
CVD	Chemical vapor deposition
cw	continuous wave
EBL	Electron beam lithography
EDX	Energy dispersive X-ray spectroscopy
EMCCD	Electron-multiplied charge-coupled device
FDTD	Finite-difference time-domain
FH	Fundamental harmonic
FIB	Focused ion beam
HIM	Helium ion microscope
IAP	Institute of Applied Physics
IBE	Ion beam etching
IBEE	Ion beam enhanced etching
ICP	Inductively coupled plasma
LNOI	Lithium niobate on insulator
NIR	Near infrared
OL	Optical lithography
PECVD	Plasma-enhanced chemical vapor deposition
PVD	Physical vapor deposition
RIBE	Reactive ion beam etching
RIE	Reactive ion etching
SEM	Scanning electron microscope
SFG	Sum frequency generation
SH	Second harmonic
SHG	Second harmonic generation
SNOM	Scanning near-field optical microscope
TE	Transverse electric
THG	Third harmonic generation
TM	Transverse magnetic

Zusammenfassung

Ziel der Arbeit war die Herstellung mikro- und nanostrukturierter optischer Elemente aus LiNbO_3 für Anwendungen in der integrierten nichtlinearen Optik. Die zur Strukturierung angewandten Prozesse sollten dabei mit etablierten Mikrostrukturtechnologien kompatibel sein, was dadurch erschwert wurde, dass LiNbO_3 mit üblichen Trockenätzverfahren nur ungenügend gut strukturiert werden kann. Ionenstrahlverstärktes Ätzen (IBEE) von LiNbO_3 ist ein Strukturierungsverfahren, das diese Einschränkungen nicht besitzt und für die Herstellung von Mikrostrukturen mit vertikalen Seitenwänden und hohem Aspektverhältnis gut geeignet ist. Zum IBEE Verfahren gab es wesentliche Vorarbeiten, die im Rahmen dieser Arbeit fortgeführt und zur Herstellung verschiedener optischer Elemente angewandt wurden. Die Auswahl der optischen Elemente beschränkte sich auf Wellenleiter und Resonatoren, die auf Basis einer wellenleitenden Schicht oder Membran ausgeführt waren. Die Membranen wurden durch Heliumionenbestrahlung von LiNbO_3 mit anschließendem Nassätzen oder aus LiNbO_3 -Dünnschichtsubstraten (LNOI) gewonnen.

Im ersten Teil der Arbeit wurde das Ätzverhalten von ionenbestrahltem LiNbO_3 in verschiedenen Hydroxidlösungen untersucht, was schließlich zur Entwicklung eines IBEE Prozesses auf Basis von KOH führte. Im Vergleich zum ursprünglich HF basierten IBEE Prozess ist KOH mit LNOI Substraten kompatibel, da KOH die SiO_2 Zwischenschicht des LNOI Substrats nicht angreift. Insbesondere der Zusammenhang zwischen der Ätzrate von ionenbestrahltem LiNbO_3 in KOH und der normierten Fluenz der Ionenbestrahlung zeigte eine hohe Selektivität, die mit dem HF basierten IBEE Prozess vergleichbar und in der Mikrostrukturtechnik anwendbar ist. Während der IBEE Prozess in Verbindung mit Lithographie für die Strukturierung größerer Flächen geeignet ist, ist die direkte Strukturierung von LiNbO_3 mit einem fokussierten Ionenstrahl (FIB) zur Prototypenentwicklung auf kleinen Flächen weit verbreitet. In dieser Arbeit wurde deshalb ebenfalls untersucht, wie LiNbO_3 Membranen mittels FIB strukturiert werden konnten. Dabei wurde herausgefunden, dass Verunreinigungen durch Galliumionen die Maßhaltigkeit des Prozesses beeinträchtigen.

Im zweiten Teil der Arbeit wurden die beschriebenen Strukturierungsmethoden für die Herstellung verschiedener Wellenleiter und Resonatoren angewendet. Ziel dabei war es, Strukturen zu realisieren, die Licht zur Verstärkung optisch nichtlinearer Wechselwirkungen in Resonator- oder Wellenleitermoden auf sehr kleine Wechselwirkungsbereiche

konzentrieren. Dies wurde experimentell durch nanoskalige Rippenwellenleiter umgesetzt, deren Querschnittsfläche so gewählt war, dass eine zweite Harmonische (SHG) phasenangepasst durch Ausnutzung der Wellenleitermodendispersion erzeugt werden konnte. Die Wellenleiter wurden sowohl freischwebend, in Flüssigkeit verteilt und mit dem Substrat verbunden hergestellt. Die Untersuchung der linearen und nichtlinearen optischen Eigenschaften belegte insbesondere, dass SHG phasenangepasst und effizient erzeugt werden konnte. Als weitere Variante eines Wellenleiters mit kompaktem Modenfelddurchmesser wurde ein W1 Wellenleiter als Liniendefekt eines photonischen Kristalls in einer freischwebenden LiNbO_3 Membran mittels IBEE hergestellt. Mit Hilfe optischer Rasternahfeldmikroskopie konnten Bandstruktur und Transmissionsspektrum dieses Wellenleiters ermittelt werden. Es zeigte sich gute Übereinstimmung mit Simulationsrechnungen, die eine konzeptionelle Weiterentwicklung hin zu Wellenleiterresonatoren ermöglichte. Durch graduelle Veränderungen der Lochdurchmesser entlang des Liniendefekts konnte hierbei die Lokalisierung des optischen Feldes in einer resonanten Struktur erreicht werden. Die erwarteten linearen optischen Eigenschaften wurden experimentell bestätigt. Durch die intrinsisch hohe Wellenleiterdämpfung war ein Nachweis nichtlinearer Effekte im Wellenleiterresonator nicht möglich, weshalb der Übergang zu Punktdefekten erfolgte. Mittels FIB wurden verschiedene L3 Resonatoren aus photonischen Kristallen hergestellt und optisch charakterisiert. Die Resonatoren wurden dabei so entworfen, dass sie vorrangig vertikal abstrahlten, um die SHG Messung zu ermöglichen. Weitere Resonatorgeometrien, die im Rahmen dieser Arbeit untersucht wurden, waren Nanobeam- und Mikrodiskresonatoren. Insgesamt wurde eine Reihe nano- und mikrostrukturierter optischer Elemente aus LiNbO_3 untersucht. Während einige Strukturen lediglich konzeptionelle Vorarbeiten für weiterführende Untersuchungen waren, wurde die Mehrzahl der untersuchten Elemente vollständig optisch charakterisiert und eine gute Übereinstimmung mit den erwarteten optischen Eigenschaften erzielt. Die untersuchten Elemente können als Grundbausteine zukünftiger nichtlinearer, integrierter-optischer Systeme erachtet werden, die auf Basis der präsentierten Verfahren zur Mikrostrukturierung von LiNbO_3 stetig weiterentwickelt werden.

Bibliography

- [1] T. H. MAIMAN, “Stimulated Optical Radiation in Ruby,” *Nature*, vol. 187, no. 4736, pp. 493–494, Aug. 1960.
- [2] P. Franken, A. Hill, C. Peters, and G. Weinreich, “Generation of Optical Harmonics,” *Phys. Rev. Lett.*, vol. 7, no. 4, pp. 118–119, Aug. 1961.
- [3] J. A. Armstrong, N. Bloembergen, J. Ducuing, and P. S. Pershan, “Interactions between Light Waves in a Nonlinear Dielectric,” *Phys. Rev.*, vol. 127, no. 6, pp. 1918–1939, Sep. 1962.
- [4] R. W. Boyd, *Nonlinear Optics*. Academic Press, 2008.
- [5] K. Nassau, H. J. J. Levinstein, and G. M. M. Loiacono, “Ferroelectric lithium niobate. 1. Growth, domain structure, dislocations and etching,” *J. Phys. Chem. Solids*, vol. 27, no. 6–7, pp. 983–988, Jun. 1966.
- [6] K. Nassau, H. J. Levinstein, and G. M. Loiacono, “Ferroelectric lithium niobate. 2. Preparation of single domain crystals,” *J. Phys. Chem. Solids*, vol. 27, no. 6, pp. 989–996, 1966.
- [7] S. C. Abrahams, J. M. Reddy, and J. L. Bernstein, “Ferroelectric lithium niobate. 3. Single crystal X-ray diffraction study at 24°C,” *J. Phys. Chem. Solids*, vol. 27, no. 6, pp. 997–1012, 1966.
- [8] S. C. Abrahams, W. C. Hamilton, and J. M. Reddy, “Ferroelectric lithium niobate. 4. Single crystal neutron diffraction study at 24°C,” *J. Phys. Chem. Solids*, vol. 27, no. 6, pp. 1013–1018, 1966.
- [9] S. C. Abrahams, H. J. Levinstein, and J. M. Reddy, “Ferroelectric lithium niobate. 5. Polycrystal X-ray diffraction study between 24° and 1200°C,” *J. Phys. Chem. Solids*, vol. 27, no. 6, pp. 1019–1026, 1966.
- [10] R. Schiek and T. Pertsch, “Absolute measurement of the quadratic nonlinear susceptibility of lithium niobate in waveguides,” *Opt. Mater. Express*, vol. 2, no. 2, p. 126, Jan. 2012.
- [11] R. S. Weis and T. K. Gaylord, “Lithium niobate: Summary of physical properties and crystal structure,” *Appl. Phys. A Solids Surfaces*, vol. 37, no. 4, pp. 191–203, Aug. 1985.
- [12] L. Arizmendi, “Photonic applications of lithium niobate crystals,” *Phys. status solidi*, vol. 201, no. 2, pp. 253–283, Jan. 2004.
- [13] H. Jin, F. M. Liu, P. Xu, J. L. Xia, M. L. Zhong, Y. Yuan, J. W. Zhou, Y. X. Gong, W. Wang, and S. N. Zhu, “On-chip generation and manipulation of entangled photons based on reconfigurable lithium-niobate waveguide circuits,” *Phys. Rev. Lett.*, vol. 113, no. 10, p. 103601, Sep. 2014.
- [14] Y.-S. Lee, T. Meade, V. Perlin, H. Winful, T. B. Norris, and A. Galvanauskas, “Generation of narrow-band terahertz radiation via optical rectification of femtosecond pulses in periodically poled lithium niobate,” *Appl. Phys. Lett.*, vol. 76, no. 18, p. 2505, May 2000.
- [15] X. Chen, M. A. Mohammad, J. Conway, B. Liu, Y. Yang, and T.-L. Ren, “High performance lithium niobate surface acoustic wave transducers in the 4–12 GHz super high frequency range,” *J. Vac. Sci. Technol. B, Nanotechnol. Microelectron. Mater. Process. Meas. Phenom.*, vol. 33, no. 6, p. 06F401, 2015.

- [16] S. Fathpour, "Emerging heterogeneous integrated photonic platforms on silicon," *Nanophotonics*, vol. 4, no. 1, Jan. 2015.
- [17] A. Kost, *Nonlinear Optics in Semiconductors I*, vol. 58. Elsevier, 1998.
- [18] K. Ogusu, J. Yamasaki, S. Maeda, M. Kitao, and M. Minakata, "Linear and nonlinear optical properties of Ag As Se chalcogenide glasses for all-optical switching," *Opt. Lett.*, vol. 29, no. 3, p. 265, Feb. 2004.
- [19] A. Zakery and S. . Elliott, "Optical properties and applications of chalcogenide glasses: a review," *J. Non. Cryst. Solids*, vol. 330, no. 1–3, pp. 1–12, Nov. 2003.
- [20] T. Skauli, P. S. Kuo, K. L. Vodopyanov, T. J. Pinguet, O. Levi, L. A. Eyres, J. S. Harris, M. M. Fejer, B. Gerard, L. Becouarn, and E. Lallier, "Improved dispersion relations for GaAs and applications to nonlinear optics," *J. Appl. Phys.*, vol. 94, no. 10, p. 6447, Oct. 2003.
- [21] A. Fiore, V. Berger, E. Rosencher, P. Bravetti, and J. Nagle, "Phase matching using an isotropic nonlinear optical material," vol. 391, no. 6666, pp. 463–466, Jan. 1998.
- [22] S. Grilli, P. Ferraro, L. Sansone, M. Paturzo, and P. De Natale, "Fabrication of sub-micron period surface structures in LiNbO₃," *Ferroelectrics*, vol. 352, pp. 320–325, 2007.
- [23] T.-J. Wang, C.-F. Huang, W.-S. Wang, and P.-K. Wei, "A novel wet-etching method using electric-field-assisted proton exchange in LiNbO₃," *J. Light. Technol.*, vol. 22, pp. 1764–1771, 2004.
- [24] R.-S. Cheng, T.-J. Wang, and W.-S. Wang, "Wet-etched ridge waveguides in y-cut lithium niobate," *J. Light. Technol.*, vol. 15, no. 10, pp. 1880–1887, 1997.
- [25] M. Kawabe, S. Hirata, and S. Namba, "Ridge Waveguides and Electra-Optical Switches in LiNbO₃, Fabricated by Ion- Bombardment-Enhanced Etching," *Circuits Syst. IEEE Trans.*, vol. m, no. 7, pp. 1109–1113, 1979.
- [26] C. I. H. Ashby, G. W. Arnold, and P. J. Brannon, "Ion-bombardment-enhanced etching of LiNbO₃ using damage profile tailoring," *J. Appl. Phys.*, vol. 65, p. 93, 1989.
- [27] F. Schrempel, T. Gischkat, H. Hartung, E.-B. Kley, and W. Wesch, "Ion beam enhanced etching of LiNbO₃," *Nucl. Instruments Methods Phys. Res. Sect. B Beam Interact. with Mater. Atoms*, vol. 250, no. 1–2, pp. 164–168, Sep. 2006.
- [28] B. E. A. Saleh and M. C. Teich, *Fundamentals of Photonics*. Wiley, 2013.
- [29] N. Bloembergen, "NONLINEAR OPTICAL PROPERTIES OF PERIODIC LAMINAR STRUCTURES," *Appl. Phys. Lett.*, vol. 17, no. 11, p. 483, Oct. 1970.
- [30] L. E. Myers, R. C. Eckardt, M. M. Fejer, R. L. Byer, W. R. Bosenberg, and J. W. Pierce, "Quasi-phase-matched optical parametric oscillators in bulk periodically poled LiNbO₃," *J. Opt. Soc. Am. B*, vol. 12, no. 11, pp. 2102–2116, 1995.
- [31] K. Moutzouris, S. Venugopal Rao, M. Ebrahimzadeh, A. De Rossi, M. Calligaro, V. Ortiz, and V. Berger, "Second-harmonic generation through optimized modal phase matching in semiconductor waveguides," *Appl. Phys. Lett.*, vol. 83, no. 4, p. 620, Jul. 2003.
- [32] K. Mizuuchi, T. Sugita, K. Yamamoto, T. Kawaguchi, T. Yoshino, and M. Imaeda, "Efficient 340-nm light generation by a ridge-type waveguide in a first-order periodically poled MgO:LiNbO₃," *Opt. Lett.*, vol. 28, no. 15, pp. 1344–1346, 2003.
- [33] S. Jette-Charbonneau, N. Lahoud, R. Charbonneau, G. Mattiussi, and P. Berini, "End-Facet Polishing of Surface Plasmon Waveguides in Lithium Niobate," *Adv. Packag. IEEE Trans.*, vol. 31, no. 3, pp. 479–483, 2008.

- [34] G. Mattiussi, N. Lahoud, R. Charbonneau, and P. Berini, "Fabrication of long-range surface plasmon-polariton waveguides in lithium niobate on silicon," *J. Vac. Sci. Technol. A Vacuum, Surfaces, Film.*, vol. 25, no. 4, pp. 692–700, 2007.
- [35] P. Berini, R. Charbonneau, S. Jetté-Charbonneau, N. Lahoud, and G. Mattiussi, "Long-range surface plasmon-polariton waveguides and devices in lithium niobate," *J. Appl. Phys.*, vol. 101, no. 11, p. 113114, 2007.
- [36] S. Jeong, H. Lee, H. Cho, S. Lee, H. Kim, S. Kim, J. Park, and H. Jeong, "Effect of Additives for Higher Removal Rate in Lithium Niobate Chemical Mechanical Planarization," *Appl. Surf. Sci.*, vol. In Press, , no. 6, p. -, Jan. 2009.
- [37] M. Levy, J. R. M. Osgood, R. Liu, L. E. Cross, G. S. Cargill III, A. Kumar, and H. Bakhru, "Fabrication of single-crystal lithium niobate films by crystal ion slicing," *Appl. Phys. Lett.*, vol. 73, no. 16, pp. 2293–2295, 1998.
- [38] I. Szafraniak, I. Radu, R. Scholz, M. Alexe, and U. Gösele, "Single-Crystalline Ferroelectric Thin Films by Ion Implantation and Direct Wafer Bonding," *Integr. Ferroelectr.*, vol. 55, no. 1, pp. 983–990, May 2003.
- [39] P. Rabiei and W. H. Steier, "Lithium niobate ridge waveguides and modulators fabricated using smart guide," *Appl. Phys. Lett.*, vol. 86, no. 16, p. 161115, 2005.
- [40] K. Diest, M. J. Archer, J. A. Dionne, Y.-B. Park, M. J. Czubakowski, and H. A. Atwater, "Silver diffusion bonding and layer transfer of lithium niobate to silicon," *Appl. Phys. Lett.*, vol. 93, no. 9, p. 92906, 2008.
- [41] L. Chen, M. G. Wood, and R. M. Reano, "12.5 pm/V hybrid silicon and lithium niobate optical microring resonator with integrated electrodes.," *Opt. Express*, vol. 21, no. 22, pp. 27003–10, Nov. 2013.
- [42] C. Wang, M. J. Burek, Z. Lin, H. A. Atikian, V. Venkataraman, I.-C. Huang, P. Stark, and M. Lončar, "Integrated high quality factor lithium niobate microdisk resonators.," *Opt. Express*, vol. 22, no. 25, pp. 30924–33, Dec. 2014.
- [43] A. Rao, A. Patil, J. Chiles, M. Malinowski, S. Novak, K. Richardson, P. Rabiei, and S. Fathpour, "Heterogeneous Microring and Mach-Zehnder Lithium Niobate Electro-Optical Modulators on Silicon," in *CLEO: 2015*, 2015, p. STu2F.4.
- [44] D. Djukic, G. Cerda-Pons, R. M. Roth, J. Richard M. Osgood, S. Bakhru, and H. Bakhru, "Electro-optically tunable second-harmonic-generation gratings in ion-exfoliated thin films of periodically poled lithium niobate," *Appl. Phys. Lett.*, vol. 90, no. 17, p. 171116, 2007.
- [45] O. Gaathon, A. Ofan, D. Djukic, J. I. Dadap, R. M. Osgood, S. Bakhru, and H. Bakhru, "Second harmonic generation in single-crystal thin membranes of LiNbO₃ fabricated by patterned He⁺ ion implantation," *2008 Conf. Lasers Electro-Optics*, pp. 1–2, May 2008.
- [46] R. M. Roth, D. Djukic, Y. S. Lee, R. M. Osgood, S. Bakhru, B. Laulicht, K. Dunn, H. Bakhru, L. Wu, M. Huang, and J. Richard M. Osgood, "Compositional and structural changes in LiNbO₃ following deep He⁺ ion implantation for film exfoliation," *Appl. Phys. Lett.*, vol. 89, no. 11, pp. 112906–1129063, Sep. 2006.
- [47] D. Djukic, R. Roth, J. Yardley, J. Richard Osgood, S. Bakhru, and H. Bakhru, "Low-voltage planar-waveguide electrooptic prism scanner in Crystal-Ion-Sliced thin-film LiNbO₃," *Opt. Express*, vol. 12, no. 25, pp. 6159–6164, 2004.
- [48] P. Rabiei and P. Gunter, "Optical and electro-optical properties of submicrometer lithium niobate slab waveguides prepared by crystal ion slicing and wafer bonding," *Appl. Phys. Lett.*, vol. 85, no. 20, pp. 4603–4605, 2004.

- [49] T. A. Ramadan, M. Levy, and J. R. M. Osgood, "Electro-optic modulation in crystal-ion-sliced z-cut LiNbO₃ thin films," *Appl. Phys. Lett.*, vol. 76, no. 11, pp. 1407–1409, 2000.
- [50] A. M. Radojevic, M. Levy, H. Kwak, and J. R. M. Osgood, "Strong nonlinear optical response in epitaxial liftoff single-crystal LiNbO₃ films," *Appl. Phys. Lett.*, vol. 75, no. 19, pp. 2888–2890, 1999.
- [51] G. Poberaj, H. Hu, W. Sohler, and P. Günter, "Lithium niobate on insulator (LNOI) for micro-phonic devices," *Laser Photon. Rev.*, vol. 6, no. 4, pp. 488–503, Jul. 2012.
- [52] F. Schrempel, T. Gischkat, H. Hartung, T. Höche, E.-B. Kley, A. Tünnermann, and W. Wesch, "Ultrathin membranes in x-cut lithium niobate," *Opt. Lett.*, vol. 34, no. 9, p. 1426, Apr. 2009.
- [53] D. Burdeaux, P. Townsend, J. Carr, and P. Garrou, "Benzocyclobutene (BCB) dielectrics for the fabrication of high density, thin film multichip modules," *J. Electron. Mater.*, vol. 19, no. 12, pp. 1357–1366, Dec. 1990.
- [54] A. Guarino, G. Poberaj, D. Rezzonico, R. Degl'Innocenti, and P. Günter, "Electro--optically tunable microring resonators in lithium niobate," *Nat. Photonics*, vol. 1, no. 7, pp. 407–410, 2007.
- [55] G. Poberaj, M. Koechlin, F. Sulser, A. Guarino, J. Hajfler, and P. Günter, "Ion-sliced lithium niobate thin films for active photonic devices," *Opt. Mater. (Amst.)*, vol. 31, no. 7, pp. 1054–1058, May 2009.
- [56] F. Sulser, G. Poberaj, M. Koechlin, and P. Günter, "Photonic crystal structures in ion-sliced lithium niobate thin films," *Opt. Express*, vol. 17, no. 22, p. 20291, Oct. 2009.
- [57] H. Hu, R. Ricken, and W. Sohler, "Lithium niobate photonic wires," *Opt. Express*, vol. 17, no. 26, pp. 24261–24268, Dec. 2009.
- [58] H. Hu, D. Buchter, L. Gui, H. Suche, V. Quiring, R. Ricken, H. Herrmann, and W. Sohler, "Lithium niobate photonic wires," in *2010 IEEE Photonic Society's 23rd Annual Meeting*, 2010, vol. 17, pp. 254–255.
- [59] H. Hu, J. Yang, L. Gui, and W. Sohler, "Lithium niobate-on-insulator (LNOI): status and perspectives," in *SPIE Photonics Europe*, 2012, p. 84311D–84311D–8.
- [60] H. Hartung, E.-B. Kley, T. Gischkat, F. Schrempel, W. Wesch, and A. Tünnermann, "Ultra thin high index contrast photonic crystal slabs in lithium niobate," *Opt. Mater. (Amst.)*, vol. 33, no. 1, pp. 19–21, Nov. 2010.
- [61] J. U. Fürst, D. V. Strelakov, D. Elser, M. Lassen, U. L. Andersen, C. Marquardt, and G. Leuchs, "Naturally phase-matched second-harmonic generation in a whispering-gallery-mode resonator," *Phys. Rev. Lett.*, vol. 104, no. 15, pp. 1–4, Apr. 2010.
- [62] M. Förtsch, G. Schunk, J. U. Fürst, D. Strelakov, T. Gerrits, M. J. Stevens, F. Sedlmeir, H. G. L. Schwefel, S. W. Nam, G. Leuchs, and C. Marquardt, "Highly efficient generation of single-mode photon pairs from a crystalline whispering-gallery-mode resonator source," *Phys. Rev. A*, vol. 91, no. 2, pp. 1–5, Feb. 2015.
- [63] G. Ulliac, B. Guichardaz, J.-Y. Rauch, S. Queste, S. Benchabane, and N. Courjal, "Ultra-smooth LiNbO₃ micro and nano structures for photonic applications," *Microelectron. Eng.*, vol. 88, no. 8, pp. 2417–2419, Aug. 2011.
- [64] T. Nishikawa, A. Ozawa, Y. Nishida, M. Asobe, F.-L. Hong, and T. W. Hänsch, "Efficient 494 mW sum-frequency generation of sodium resonance radiation at 589 nm by using a periodically poled Zn:LiNbO₃ ridge waveguide," *Opt. Express*, vol. 17, no. 20, p. 17792, Sep. 2009.

- [65] J. Sun, Y. Gan, and C. Xu, "Efficient green-light generation by proton-exchanged periodically poled MgO:LiNbO₃ ridge waveguide," *Opt. Lett.*, vol. 36, no. 4, p. 549, Feb. 2011.
- [66] N. Courjal, B. Guichardaz, G. Ulliac, J.-Y. Rauch, B. Sadani, H.-H. Lu, and M.-P. Bernal, "High aspect ratio lithium niobate ridge waveguides fabricated by optical grade dicing," *J. Phys. D. Appl. Phys.*, vol. 44, no. 30, p. 305101, Aug. 2011.
- [67] Y. Takeuchi, Y. Sakaida, K. Sawada, and T. Sata, "Development of a 5-Axis Control Ultraprecision Milling Machine for Micromachining Based on Non-Friction Servomechanisms," *CIRP Ann. - Manuf. Technol.*, vol. 49, no. 1, pp. 295–298, Jan. 2000.
- [68] R. Takigawa, E. Higurashi, T. Kawanishi, and T. Asano, "Lithium niobate ridged waveguides with smooth vertical sidewalls fabricated by an ultra-precision cutting method," *Opt. Express*, vol. 22, no. 22, p. 27733, Oct. 2014.
- [69] J. Kondo, A. Kondo, K. Aoki, M. Imaeda, T. Mori, Y. Mizuno, S. Takatsuji, Y. Kozuka, O. Mitomi, and M. Minakata, "40-Gb/s X-cut LiNbO₃ optical modulator with two-step back-slot structure," *J. Light. Technol.*, vol. 20, no. 12, pp. 2110–2114, Dec. 2002.
- [70] M. Ishikawa and M. Iwanaga, "In-Plane Second Harmonic Generations in Photonic Crystal Slabs of LiNbO₃," *Appl. Phys. Express*, vol. 1, no. 8, p. 82101, 2008.
- [71] J. Lin, Y. Xu, Z. Fang, M. Wang, J. Song, N. Wang, L. Qiao, W. Fang, and Y. Cheng, "Fabrication of high-Q lithium niobate microresonators using femtosecond laser micromachining," *Sci. Rep.*, vol. 5, p. 8072, Jan. 2015.
- [72] J. Burghoff, C. Grebing, S. Nolte, and A. Tünnermann, "Efficient frequency doubling in femtosecond laser-written waveguides in lithium niobate," *Appl. Phys. Lett.*, vol. 89, no. 8, p. 081108, Aug. 2006.
- [73] A. Rodenas, G. Zhou, D. Jaque, and M. Gu, "Rare-Earth Spontaneous Emission Control in Three-Dimensional Lithium Niobate Photonic Crystals," *Adv. Mater.*, 2009.
- [74] M. Fukuma, J. Noda, and H. Iwasaki, "Optical properties in titanium-diffused LiNbO₃ strip waveguides," *J. Appl. Phys.*, vol. 49, no. 7, p. 3693, Aug. 1978.
- [75] I. P. Kaminow and L. W. Stulz, "Loss in cleaved Ti-diffused LiNbO₃ waveguides," *Appl. Phys. Lett.*, vol. 33, no. 1, p. 62, Aug. 1978.
- [76] A. Loni, R. M. De La Rue, and J. M. Winfield, "Proton-exchanged, lithium niobate planar-optical waveguides: Chemical and optical properties and room-temperature hydrogen isotopic exchange reactions," *J. Appl. Phys.*, vol. 61, no. 1, p. 64, 1987.
- [77] J. Burghoff, H. Hartung, S. Nolte, and A. Tünnermann, "Structural properties of femtosecond laser-induced modifications in LiNbO₃," *Appl. Phys. A*, vol. 86, no. 2, pp. 165–170, Nov. 2006.
- [78] F. Chen, "Photonic guiding structures in lithium niobate crystals produced by energetic ion beams," *J. Appl. Phys.*, vol. 106, no. 8, p. 081101, Oct. 2009.
- [79] J. Amet, G. Ulliac, F. I. Baida, and M.-P. Bernal, "Experimental evidence of enhanced electro-optic control on a lithium niobate photonic crystal superprism," *Appl. Phys. Lett.*, vol. 96, no. 10, p. 103111, 2010.
- [80] E. J. Lim, M. M. Fejer, and R. L. Byer, "Second-harmonic generation of green light in periodically poled planar lithium niobate waveguide," *Electron. Lett.*, vol. 25, no. 3, p. 174, 1989.
- [81] M. Yamada, N. Nada, M. Saitoh, and K. Watanabe, "First-order quasi-phase matched

- LiNbO₃ waveguide periodically poled by applying an external field for efficient blue second-harmonic generation,” *Appl. Phys. Lett.*, vol. 62, no. 5, p. 435, Feb. 1993.
- [82] Y.-H. Chen, W.-K. Chang, H.-P. Chung, and P.-Y. Chou, “2D Quadratic Nonlinear Photonic Crystal for Pulsed Orange Generation in a Dual-Wavelength Nd:YVO₄ Laser,” in *CLEO: 2015*, 2015, p. JTU5A.36.
- [83] A. C. Busacca, C. L. Sones, V. Apostolopoulos, R. W. Eason, and S. Mailis, “Surface domain engineering in congruent lithium niobate single crystals: A route to submicron periodic poling,” *Appl. Phys. Lett.*, vol. 81, no. 26, p. 4946, Dec. 2002.
- [84] L. S. Kokhanchik, R. V. Gainutdinov, S. D. Lavrov, E. D. Mishina, and T. R. Volk, “E-Beam Recording of Domain Structures on the Nonpolar Surface of LiNbO₃ Crystals at Different SEM Voltages and Their Investigation by PFM and SHG Microscopy,” *Ferroelectrics*, vol. 480, no. 1, pp. 49–57, Jul. 2015.
- [85] L. S. Kokhanchik, R. V. Gainutdinov, S. D. Lavrov, and T. R. Volk, “Characteristics of microdomains and microdomain patterns recorded by electron beam irradiation on Y-cut LiNbO₃ crystals,” *J. Appl. Phys.*, vol. 118, no. 7, p. 072001, Aug. 2015.
- [86] C. Restoin, C. Darraud-Taupiac, J.-L. Decossas, J.-C. Vareille, V. Couderc, A. Barthélémy, A. Martinez, and J. Hauden, “Electron-Beam Poling on Ti:LiNbO₃,” *Appl. Opt.*, vol. 40, no. 33, p. 6056, Nov. 2001.
- [87] C. Restoin, S. Massy, C. Darraud-Taupiac, and A. Barthelemy, “Fabrication of 1D and 2D structures at submicrometer scale on lithium niobate by electron beam bombardment,” *Opt. Mater. (Amst.)*, vol. 22, no. 3, pp. 193–199, May 2003.
- [88] X. Li, K. Terabe, H. Hatano, and K. Kitamura, “Domain patterning in LiNbO₃ and LiTaO₃ by focused electron beam,” *J. Cryst. Growth*, vol. 292, no. 2, pp. 324–327, Jul. 2006.
- [89] J. He, S. H. Tang, Y. Q. Qin, P. Dong, H. Z. Zhang, C. H. Kang, W. X. Sun, and Z. X. Shen, “Two-dimensional structures of ferroelectric domain inversion in LiNbO₃ by direct electron beam lithography,” *J. Appl. Phys.*, vol. 93, no. 12, p. 9943, May 2003.
- [90] C. Restoin, C. Darraud-Taupiac, J. L. Decossas, J. C. Vareille, J. Hauden, and A. Martinez, “Ferroelectric domain inversion by electron beam on LiNbO₃ and Ti:LiNbO₃,” *J. Appl. Phys.*, vol. 88, no. 11, p. 6665, Dec. 2000.
- [91] X. Li, K. Terabe, H. Hatano, H. Zeng, and K. Kitamura, “Domain patterning thin crystalline ferroelectric film with focused ion beam for nonlinear photonic integrated circuits,” *J. Appl. Phys.*, vol. 100, no. 10, p. 106103, Nov. 2006.
- [92] M. Mohageg, D. V. Strelakov, A. A. Savchenkov, A. B. Matsko, V. S. Ilchenko, and L. Maleki, “Calligraphic poling of Lithium Niobate,” *Opt. Express*, vol. 13, no. 9, p. 3408, 2005.
- [93] D. Yudistira, A. Boes, A. R. Rezk, L. Y. Yeo, J. R. Friend, and A. Mitchell, “UV Direct Write Metal Enhanced Redox (MER) Domain Engineering for Realization of Surface Acoustic Devices on Lithium Niobate,” *Adv. Mater. Interfaces*, vol. 1, no. 4, p. n/a–n/a, Jul. 2014.
- [94] A. Boes, V. Sivan, G. Ren, D. Yudistira, S. Mailis, E. Soergel, and A. Mitchell, “Precise, reproducible nano-domain engineering in lithium niobate crystals,” *Appl. Phys. Lett.*, vol. 107, no. 2, p. 022901, Jul. 2015.
- [95] V. Sivan, A. Mitchell, L. Bui, A. Holland, S. Bhargava, and T. Priest, “Etching of lithium niobate using standard Ti indiffusion technique,” *Appl. Phys. Lett.*, vol. 91, no. 23, p. 231921, Dec. 2007.
- [96] V. Sivan, A. Holland, A. P. O’Mullane, and A. Mitchell, “Investigation of the physical

- origins of etching LiNbO₃ during Ti in-diffusion,” *Appl. Phys. Lett.*, vol. 96, no. 12, p. 121913, Mar. 2010.
- [97] L. Cai, S. L. H. Han, and H. Hu, “Waveguides in single-crystal lithium niobate thin film by proton exchange,” *Opt. Express*, vol. 23, no. 2, pp. 1240–8, Jan. 2015.
- [98] C.-C. Lai, C.-Y. Chang, Y.-Y. Wei, and W.-S. Wang, “Gamma-Ray Irradiation-Enhanced Wet-Etching of Proton-Exchanged Lithium Niobate,” *IEEE Photonics Technol. Lett.*, vol. 20, pp. 682–684, 2008.
- [99] T.-L. Ting, L.-Y. Chen, and W.-S. Wang, “A novel wet-etching method using joint proton source in LiNbO₃,” *IEEE Photonics Technol. Lett.*, vol. 18, pp. 568–570, 2006.
- [100] M. Sridhar, D. K. Maurya, J. R. Friend, and L. Y. Yeo, “Focused ion beam milling of microchannels in lithium niobate,” *Biomicrofluidics*, vol. 6, no. 1, pp. 12819–1281911, Mar. 2012.
- [101] C.-H. Hou, M.-P. Bernal, C.-C. Chen, R. Salut, C. Sada, N. Argiolas, M. Bazzan, and M. V Ciampolillo, “Purcell effect observation in erbium doped lithium niobate photonic crystal structures,” *Opt. Commun.*, vol. 281, no. 15–16, pp. 4151–4154, 2008.
- [102] S. Diziain, S. Harada, R. Salut, P. Muralt, and M.-P. Bernal, “Strong improvement in the photonic stop-band edge sharpness of a lithium niobate photonic crystal slab,” *Appl. Phys. Lett.*, vol. 95, no. 10, p. 101103, Sep. 2009.
- [103] M. Roussey, M.-P. Bernal, N. N. Courjal, and F. I. Baida, “Experimental and theoretical characterization of a lithium niobate photonic crystal,” *Appl. Phys. Lett.*, vol. 87, no. 24, p. 241101, Dec. 2005.
- [104] M.-P. Bernal, N. Courjal, J. Amet, M. Roussey, and C. H. H. Hou, “Lithium niobate photonic crystal waveguides: Far field and near field characterisation,” *Opt. Commun.*, vol. 265, no. 1, pp. 180–186, Sep. 2006.
- [105] S. Diziain, J. Amet, F. I. Baida, M.-P. P. Bernal, S. S. Diziain, J. Amet, F. I. Baida, and M.-P. P. Bernal, “Optical far-field and near-field observations of the strong angular dispersion in a lithium niobate photonic crystal superprism designed for double (passive and active) demultiplexer applications,” *Appl. Phys. Lett.*, vol. 93, no. 26, p. 261103, Dec. 2008.
- [106] M.-P. Bernal, M. Roussey, and F. I. Baida, “Near- and far-field verification of electro-optic effect enhancement on a tunable lithium niobate photonic crystal,” *J. Microsc.*, vol. 229, no. Pt 2, pp. 264–9, Feb. 2008.
- [107] M. Roussey, F. I. Baida, and M.-P. Bernal, “Experimental and theoretical observations of the slow-light effect on a tunable photonic crystal,” *J. Opt. Soc. Am. B*, vol. 24, no. 6, pp. 1416–1422, 2007.
- [108] M. Roussey, M.-P. Bernal, N. Courjal, D. Van Labeke, F. I. Baida, and R. Salut, “Electro-optic effect exaltation on lithium niobate photonic crystals due to slow photons,” *Appl. Phys. Lett.*, vol. 89, no. 24, p. 241110, Dec. 2006.
- [109] H. Lu, F. Issam Baida, G. Ulliac, N. Courjal, M. Collet, and M.-P. Bernal, “Lithium niobate photonic crystal wire cavity: Realization of a compact electro-optically tunable filter,” *Appl. Phys. Lett.*, vol. 101, no. 15, p. 151117, Oct. 2012.
- [110] H. Lu, B. Sadani, N. Courjal, G. Ulliac, N. Smith, V. Stenger, M. Collet, F. I. Baida, and M.-P. Bernal, “Enhanced electro-optical lithium niobate photonic crystal wire waveguide on a smart-cut thin film,” *Opt. Express*, vol. 20, no. 3, pp. 2974–81, Jan. 2012.
- [111] J. Dahdah, M. Pilar-Bernal, N. Courjal, G. Ulliac, and F. Baida, “Near-field observations of light confinement in a two dimensional lithium niobate photonic crystal

- cavity,” *J. Appl. Phys.*, vol. 110, no. 7, p. 74318, 2011.
- [112] H. Lu, B. Sadani, G. Ulliac, N. Courjal, C. Guyot, J.-M. Merolla, M. Collet, F. I. Baida, and M.-P. Bernal, “6-micron interaction length electro-optic modulation based on lithium niobate photonic crystal cavity,” *Opt. Express*, vol. 20, no. 19, pp. 20884–93, Sep. 2012.
- [113] H. Lu, B. Sadani, G. Ulliac, C. Guyot, N. Courjal, M. Collet, F. I. Baida, and M.-P. Bernal, “Integrated temperature sensor based on an enhanced pyroelectric photonic crystal,” *Opt. Express*, vol. 21, no. 14, pp. 16311–8, Jul. 2013.
- [114] N. Courjal, S. Benchabane, J. Dahdah, G. Ulliac, Y. Gruson, and V. Laude, “Acousto-optically tunable lithium niobate photonic crystal,” *Appl. Phys. Lett.*, vol. 96, no. 13, p. 131103, 2010.
- [115] G. Si, E. J. Teo, A. A. Bettioli, J. Teng, and A. J. Danner, “Suspended slab and photonic crystal waveguides in lithium niobate,” *J. Vac. Sci. Technol. B Microelectron. Nanom. Struct.*, vol. 28, no. 2, pp. 316–320, 2010.
- [116] M. R. Beghoul, B. Fougere, A. Boudrioua, C. Darraud, S. Latreche, R. Kremer, P. Moretti, and J. C. Vareille, “Photonic band gap grating in He⁺-implanted lithium niobate waveguides,” *Opt. Quantum Electron.*, vol. 39, no. 4–6, pp. 333–340, Jun. 2007.
- [117] N. Courjal, J. Dahdah, G. Ulliac, P. Sevillano, B. Guichardaz, and F. Baida, “Optimization of LiNbO₃ photonic crystals: toward 3D LiNbO₃ micro-components,” *Opt. Express*, vol. 19, no. 23, pp. 23008–23016, Nov. 2011.
- [118] O. Yavuzcetin, B. Ozturk, D. Xiao, and S. Sridhar, “Conicity and depth effects on the optical transmission of lithium niobate photonic crystals patterned by focused ion beam,” *Opt. Mater. Express*, vol. 1, no. 7, p. 1262, Oct. 2011.
- [119] G. W. Burr, S. Diziain, and M.-P. Bernal, “The impact of finite-depth cylindrical and conical holes in lithium niobate photonic crystals,” *Opt. Express*, vol. 16, no. 9, pp. 6302–6316, 2008.
- [120] X. Xu, S. Yan, J. Xue, Y. Wang, K. Wang, and X. Wang, “Investigation of etching two-dimensional microhole lattice array on lithium niobate with focused ion beam for fabricating photonic crystals,” *J. Vac. Sci. Technol. B Microelectron. Nanom. Struct.*, vol. 27, no. 4, p. 1851, Jun. 2009.
- [121] G. Si, A. J. Danner, S. L. Teo, E. J. Teo, J. Teng, and A. A. Bettioli, “Photonic crystal structures with ultrahigh aspect ratio in lithium niobate fabricated by focused ion beam milling,” *J. Vac. Sci. Technol. B Microelectron. Nanom. Struct.*, vol. 29, no. 2, p. 021205, Mar. 2011.
- [122] S. Benchabane, L. Robert, J.-Y. Rauch, A. Khelif, and V. Laude, “Highly selective electroplated nickel mask for lithium niobate dry etching,” *J. Appl. Phys.*, vol. 105, no. 9, p. 094109, May 2009.
- [123] A. Lecestre, S. Benchabane, L. Robert, R. Salut, G. Ulliac, and P. Blind, “Electroplated Ni mask for plasma etching of submicron-sized features in LiNbO₃,” *Microelectron. Eng.*, vol. 105, no. null, pp. 95–98, May 2013.
- [124] J. L. Jackel, “Reactive ion etching of LiNbO₃,” *Appl. Phys. Lett.*, vol. 38, no. 11, p. 907, Jun. 1981.
- [125] G. Ulliac, N. Courjal, H. M. H. Chong, and R. M. D. La Rue, “Batch process for the fabrication of LiNbO₃ photonic crystals using proton exchange followed by CHF₃ reactive ion etching,” *Opt. Mater. (Amst.)*, vol. 31, no. 2, pp. 196–200, Oct. 2008.
- [126] D. Jun, J. Wei, C. Eng Png, S. Guangyuan, J. Son, H. Yang, and A. J. Danner, “Deep

- anisotropic LiNbO₃ etching with SF₆/Ar inductively coupled plasmas,” *J. Vac. Sci. Technol. B Microelectron. Nanom. Struct.*, vol. 30, no. 1, p. 011208, 2012.
- [127] Z. Ren, P. J. Heard, J. M. Marshall, P. A. Thomas, and S. Yu, “Etching characteristics of LiNbO₃ in reactive ion etching and inductively coupled plasma,” *J. Appl. Phys.*, vol. 103, no. 3, p. 034109, Feb. 2008.
- [128] G. Ulliac, B. Guichardaz, J.-Y. Rauch, S. Queste, S. Benchabane, and N. Courjal, “Ultra-smooth LiNbO₃ micro and nano structures for photonic applications,” *Microelectron. Eng.*, vol. 88, no. 8, pp. 2417–2419, Aug. 2011.
- [129] C. Dubs, J.-P. Ruske, J. Kräußlich, and A. Tünnermann, “Rib waveguides based on Zn-substituted LiNbO₃ films grown by liquid phase epitaxy,” *Opt. Mater. (Amst.)*, vol. 31, no. 11, pp. 1650–1657, Sep. 2009.
- [130] D. S. Hines and K. E. Williams, “Patterning of wave guides in LiNbO₃ using ion beam etching and reactive ion beam etching,” *J. Vac. Sci. Technol. A Vacuum, Surfaces, Film.*, vol. 20, no. 3, p. 1072, May 2002.
- [131] W. J. Park, W. S. Yang, W. K. Kim, H. Y. Lee, J.-W. Lim, M. Isshiki, and D. H. Yoon, “Ridge structure etching of LiNbO₃ crystal for optical waveguide applications,” *Opt. Mater. (Amst.)*, vol. 28, no. 3, pp. 216–220, Feb. 2006.
- [132] J.-H. Zhao, X.-H. Liu, Q. Huang, P. Liu, and W. X.-L. Wang, “Lithium Niobate Ridge Waveguides Fabricated by Ion Implantation Followed by Ion Beam Etching,” *J. Light. Technol.*, vol. 28, no. 13, pp. 1913–1916, Jul. 2010.
- [133] H. Hu, A. P. Milenin, R. B. Wehrspohn, H. Hermann, and W. Sohler, “Plasma etching of proton-exchanged lithium niobate,” *J. Vac. Sci. Technol. A Vacuum, Surfaces, Film.*, vol. 24, no. 4, pp. 1012–1015, 2006.
- [134] E. Barakat, M.-P. Bernal, and F. I. Baida, “Doubly resonant Ag–LiNbO₃ embedded coaxial nanostructure for high second-order nonlinear conversion,” *J. Opt. Soc. Am. B*, vol. 30, no. 7, p. 1975, Jun. 2013.
- [135] E. H. Barakat, M.-P. Bernal, and F. I. Baida, “Second Harmonic Generation enhancement by use of annular aperture arrays embedded into silver and filled by lithium Niobate,” *Opt. Express*, vol. 18, no. 7, pp. 6530–6536, 2010.
- [136] E. Barakat, M.-P. Bernal, and F. I. Baida, “Theoretical analysis of enhanced nonlinear conversion from metallo-dielectric nano-structures,” *Opt. Express*, vol. 20, no. 15, p. 16258, Jul. 2012.
- [137] Z. Zhou, X. Huang, R. R. Vanga, and Z. Wu, “Enhanced photonic bandgap in ion-implanted lithium niobate waveguides by improving index contrast,” *J. Opt. Soc. Am. B*, vol. 27, no. 7, pp. 1425–1429, 2010.
- [138] F. Lacour, N. Courjal, M.-P. Bernal, A. Sabac, C. Bainier, and M. Spajer, “Nanostructuring lithium niobate substrates by focused ion beam milling,” *Opt. Mater. (Amst.)*, vol. 27, no. 8, pp. 1421–1425, May 2005.
- [139] O. Yavuzcetin, H. P. Novikov, R. L. Dally, S. T. Malley, N. R. Perry, B. Ozturk, and S. Sridhar, “Photonic crystal fabrication in lithium niobate via pattern transfer through wet and dry etched chromium mask,” *J. Appl. Phys.*, vol. 112, no. 7, p. 074303, Oct. 2012.
- [140] A. Majkic, M. Koechlin, G. Poberaj, and P. Günter, “Optical microring resonators in fluorine-implanted lithium niobate,” *Opt. Express*, vol. 16, no. 12, pp. 8769–8779, 2008.
- [141] Y. Li, C. Wang, and M. Loncar, “Design of nano-groove photonic crystal cavities in lithium niobate,” *Opt. Lett.*, vol. 40, no. 12, pp. 2902–5, Jun. 2015.

- [142] S. Jetschke, H. Karge, and K. Hehl, "Anisotropic Effects in N⁺-Implanted LiNbO₃," *Phys. Status Solidi*, vol. 77, no. 1, pp. 207–214, May 1983.
- [143] G. W. Arnold, "Light element redistribution and property changes in insulators due to ion bombardment and chemical processing," *Nucl. Instruments Methods Phys. Res. Sect. B Beam Interact. with Mater. Atoms*, vol. 39, no. 1–4, pp. 708–715, Mar. 1989.
- [144] B. Canut, R. Brenier, A. Meftah, P. Moretti, S. Ould Salem, S. M. M. Ramos, P. Thevenard, and M. Toulemonde, "Damage induced in LiNbO₃ single crystals by GeV gadolinium ions," *Nucl. Instruments Methods Phys. Res. Sect. B Beam Interact. with Mater. Atoms*, vol. 91, no. 1–4, pp. 312–316, Jun. 1994.
- [145] M. Bianconi, N. Argiolas, M. Bazzan, G. G. Bentini, M. Chiarini, A. Cerutti, P. Mazzoldi, G. Pennestri, and C. Sada, "Nuclear and electronic energy loss synergy in the process of damage growth in ion implanted LiNbO₃," *Nucl. Instruments Methods Phys. Res. Sect. B Beam Interact. with Mater. Atoms*, vol. 249, no. 1–2, pp. 122–125, Aug. 2006.
- [146] M. Bianconi, N. Argiolas, M. Bazzan, G. G. Bentini, A. Cerutti, M. Chiarini, G. Pennestri, P. Mazzoldi, and C. Sada, "Quantification of nuclear damage in high energy ion implanted lithium niobate," *Nucl. Instruments Methods Phys. Res. Sect. B Beam Interact. with Mater. Atoms*, vol. 257, no. 1–2, pp. 597–600, Apr. 2007.
- [147] A. Garcia-Navarro, F. Agullo-Lopez, M. Bianconi, J. Olivares, and G. Garcia, "Kinetics of ion-beam damage in lithium niobate," *J. Appl. Phys.*, vol. 101, no. 8, p. 83506, 2007.
- [148] T. Steinbach, F. Schrempel, T. Gischkat, and W. Wesch, "Influence of ion energy and ion species on ion channeling in LiNbO₃," *Phys. Rev. B*, vol. 78, no. 18, p. 184106, Nov. 2008.
- [149] T. Gischkat, F. Schrempel, and W. Wesch, "Ion-beam induced effects at 15K in LiNbO₃," *Nucl. Instruments Methods Phys. Res. Sect. B Beam Interact. with Mater. Atoms*, vol. 266, no. 12–13, pp. 2906–2909, Jun. 2008.
- [150] J. Reinisch, F. Schrempel, T. Gischkat, and W. Wesch, "Etching of Ion Irradiated LiNbO₃ in Aqueous Hydrofluoric Solutions," *J. Electrochem. Soc.*, vol. 155, no. 4, p. D298, Apr. 2008.
- [151] A. Ofan, O. Gaathon, L. Vanamurthy, S. Bakhru, H. Bakhru, K. Evans-Lutterodt, and J. Richard M. Osgood, "Origin of highly spatially selective etching in deeply implanted complex oxides," *Appl. Phys. Lett.*, vol. 93, no. 18, p. 181906, 2008.
- [152] T. Gischkat, F. Schrempel, T. Höche, and W. Wesch, "Annealing behavior of lithium niobate irradiated with He-ions at 100K," *Nucl. Instruments Methods Phys. Res. Sect. B Beam Interact. with Mater. Atoms*, vol. 267, no. 8–9, pp. 1492–1495, May 2009.
- [153] M. Bianconi, G. G. Bentini, M. Chiarini, P. De Nicola, G. B. Montanari, A. Nubile, and S. Sugliani, "Defect engineering and micromachining of Lithium Niobate by ion implantation," *Nucl. Instruments Methods Phys. Res. Sect. B Beam Interact. with Mater. Atoms*, vol. 267, no. 17, pp. 2839–2845, Sep. 2009.
- [154] T. Gischkat, H. Hartung, F. Schrempel, E. B. Kley, A. Tünnermann, and W. Wesch, "Patterning of LiNbO₃ by means of ion irradiation using the electronic energy deposition and wet etching," *Microelectron. Eng.*, vol. 86, no. 4–6, pp. 910–912, Apr. 2009.
- [155] J. Olivares, M. L. Crespillo, O. Caballero-Calero, M. D. Ynsa, A. Garcia-Cabañes, M. Toulemonde, C. Trautmann, and F. Agulló-López, "Thick optical waveguides in lithium niobate induced by swift heavy ions (~10 MeV/amu) at ultralow fluences," *Opt. Express*, vol. 17, no. 26, pp. 24175–24182, 2009.

- [156] S.-M. Zhang, K.-M. Wang, X. X.-H. Liu, and Z. Bi, "Planar and ridge waveguides formed in LiNbO₃ by proton exchange combined with oxygen ion implantation.," *Opt. Express*, vol. 18, no. 15, pp. 15609–17, Jul. 2010.
- [157] A. Ofan, L. Zhang, O. Gaathon, S. Bakhru, H. Bakhru, Y. Zhu, D. Welch, and R. M. Osgood, "Spherical solid He nanometer bubbles in an anisotropic complex oxide," *Phys. Rev. B*, vol. 82, no. 10, p. 104113, Sep. 2010.
- [158] E. Schmidt, T. Steinbach, and W. Wesch, "Ion-beam-induced thin film stress in lithium niobate," *J. Phys. D. Appl. Phys.*, vol. 47, no. 26, p. 265302, Jul. 2014.
- [159] H. Hartung, E.-B. Kley, A. Tünnermann, T. Gischkat, F. Schrempel, and W. Wesch, "Fabrication of ridge waveguides in zinc-substituted lithium niobate by means of ion-beam enhanced etching," *Opt. Lett.*, vol. 33, no. 20, pp. 2320–2322, Oct. 2008.
- [160] T.-J. Wang, J.-Y. He, C.-A. Lee, and H. Niu, "High-quality LiNbO₃ microdisk resonators by undercut etching and surface tension reshaping.," *Opt. Express*, vol. 20, no. 27, pp. 28119–24, Dec. 2012.
- [161] D. Lehr, J. Reinhold, I. Thiele, H. Hartung, K. Dietrich, C. Menzel, T. Pertsch, E.-B. Kley, and A. Tünnermann, "Enhancing Second Harmonic Generation in Gold Nanoring Resonators Filled with Lithium Niobate," *Nano Lett.*, vol. 15, no. 2, pp. 1025–1030, Feb. 2015.
- [162] Y. Kakehi, A. Okamoto, Y. Sakurai, Y. Nishikawa, T. Yotsuya, and S. Ogawa, "Epitaxial growth of LiNbO₃ thin films using pulsed laser deposition," *Appl. Surf. Sci.*, vol. 169–170, pp. 560–563, Jan. 2001.
- [163] Y. Shibata, K. Kaya, K. Akashi, M. Kanai, T. Kawai, and S. Kawai, "Epitaxial growth of LiNbO₃ thin films by excimer laser ablation method and their surface acoustic wave properties," *Appl. Phys. Lett.*, vol. 61, no. 8, p. 1000, Aug. 1992.
- [164] Y. Akiyama, K. Shitanaka, H. Murakami, Y.-S. Shin, M. Yoshida, and N. Imaishi, "Epitaxial growth of lithium niobate film using metalorganic chemical vapor deposition," *Thin Solid Films*, vol. 515, no. 12, pp. 4975–4979, Apr. 2007.
- [165] S. Miyazawa, S. Fushimi, and S. Kondo, "Optical waveguide of LiNbO₃ thin film grown by liquid phase epitaxy," *Appl. Phys. Lett.*, vol. 26, no. 1, p. 8, Sep. 1975.
- [166] S. Kondo, S. Miyazawa, S. Fushimi, and K. Sugii, "Liquid-phase-epitaxial growth of single-crystal LiNbO₃ thin film," *Appl. Phys. Lett.*, vol. 26, no. 9, p. 489, Sep. 1975.
- [167] S. Takada, "Optical waveguides of single-crystal LiNbO₃ film deposited by rf sputtering," *Appl. Phys. Lett.*, vol. 24, no. 10, p. 490, Oct. 1974.
- [168] R. Grange, F. Dutto, and A. Radenovic, *Niobates Nanowires: Synthesis, Characterization and Applications*. InTech, 2011.
- [169] R. Grange, J.-W. Choi, C.-L. Hsieh, Y. Pu, A. Magrez, R. Smajda, L. Forró, and D. Psaltis, "Lithium niobate nanowires synthesis, optical properties, and manipulation," *Appl. Phys. Lett.*, vol. 95, no. 14, p. 143105, Oct. 2009.
- [170] C.-L. Hsieh, R. Grange, Y. Pu, and D. Psaltis, "Three-dimensional harmonic holographic microscopy using nanoparticles as probes for cell imaging," *Opt. Express*, vol. 17, no. 4, p. 2880, Feb. 2009.
- [171] K. Nassau, H. J. Levinstein, G. M. Loiacono, B. T. Laboratories, and M. Hill, "FERROELECTRIC GROWTH, DOMAIN LITHIUM DISLOCATIONS," vol. 27, pp. 983–988, 1966.
- [172] R. S. Weis and T. K. Gaylord, vol. 203, pp. 191–203, 1985.
- [173] J. D. Jackson, *Classical Electrodynamics, 3rd Edition*. Wiley-VCH, 1998.

- [174] P. N. Butcher and D. Cotter, *The Elements of Nonlinear Optics*. Cambridge University Press, 1991.
- [175] S. Ducci, L. Lanco, V. Berger, A. De Rossi, V. Ortiz, and M. Calligaro, “Continuous-wave second-harmonic generation in modal phase matched semiconductor waveguides,” *Appl. Phys. Lett.*, vol. 84, no. 16, p. 2974, Apr. 2004.
- [176] R. Geiss, S. Saravi, A. Sergeyeve, S. Diziain, F. Setzpfandt, F. Schrempel, R. Grange, E.-B. Kley, A. Tünnermann, and T. Pertsch, “Fabrication of nanoscale lithium niobate waveguides for second-harmonic generation,” *Opt. Lett.*, vol. 40, no. 12, pp. 2715–2718, Jun. 2015.
- [177] H. Sekoguchi, Y. Takahashi, T. Asano, and S. Noda, “Photonic crystal nanocavity with a Q-factor of ~ 9 million,” *Opt. Express*, vol. 22, no. 1, pp. 916–24, Jan. 2014.
- [178] J. D. Joannopoulos, S. G. Johnson, J. N. Winn, and R. D. Meade, *Photonic crystals : molding the flow of light*. Princeton University Press, 2008.
- [179] K. Sakoda, *Optical properties of photonic crystals*. Springer Science & Business Media, 2004.
- [180] R. Iliew, C. Etrich, T. Pertsch, and F. Lederer, “Minimization of out-of-plane losses of photonic crystal membranes,” *Phys. Rev. B*, vol. 80, no. 3, p. 35123, Jul. 2009.
- [181] A. Taflove and S. C. Hagness, *Computational Electrodynamics: The Finite-Difference Time-Domain Method*, 3rd ed. Artech House, 2005.
- [182] P. Rai-Choudhury, *Handbook of microlithography, micromachining, and microfabrication: microlithography*. Iet, 1997.
- [183] G. Wiederrecht, *Handbook of nanofabrication*. Academic Press, 2010.
- [184] A. N. Broers, A. C. F. Hoole, and J. M. Ryan, “Electron beam lithography—Resolution limits,” *Microelectron. Eng.*, vol. 32, no. 1–4, pp. 131–142, Sep. 1996.
- [185] C. Mack, *Fundamental principles of optical lithography: the science of microfabrication*. John Wiley & Sons, 2008.
- [186] T. Ito and S. Okazaki, “Pushing the limits of lithography,” *Nature*, vol. 406, no. 6799, pp. 1027–31, Aug. 2000.
- [187] F. WATT, A. A. BETTIOL, J. A. VAN KAN, E. J. TEO, and M. B. H. BREESE, “ION BEAM LITHOGRAPHY AND NANOFABRICATION: A REVIEW,” *Int. J. Nanosci.*, vol. 04, no. 03, pp. 269–286, Jun. 2005.
- [188] S. Reyntjens and R. Puers, “A review of focused ion beam applications in microsystem technology,” *J. Micromechanics Microengineering*, vol. 11, no. 4, pp. 287–300, Jul. 2001.
- [189] J. Orloff, L. Swanson, and M. Utlaut, *High Resolution Focused Ion Beams: FIB and its Applications: Fib and Its Applications: The Physics of Liquid Metal Ion Sources and Ion Optics and Their Application to Focused Ion Beam Technology*. Springer Science & Business Media, 2003.
- [190] M. A. Draganski, E. Finkman, B. C. Gibson, B. A. Fairchild, K. Ganesan, N. Nabatova-Gabain, S. Tomljenovic-Hanic, A. D. Greentree, and S. Prawer, “The effect of gallium implantation on the optical properties of diamond,” *Diam. Relat. Mater.*, vol. 35, no. null, pp. 47–52, May 2013.
- [191] V. Castaldo, C. W. Hagen, P. Kruit, E. van Veldhoven, and D. Maas, “On the influence of the sputtering in determining the resolution of a scanning ion microscope,” *J. Vac. Sci. Technol. B Microelectron. Nanom. Struct.*, vol. 27, no. 6, p. 3196, Dec. 2009.
- [192] M. C. Lemme, D. C. Bell, J. R. Williams, L. A. Stern, B. W. H. Baugher, P. Jarillo-

- Herrero, and C. M. Marcus, "Etching of graphene devices with a helium ion beam.," *ACS Nano*, vol. 3, no. 9, pp. 2674–6, Sep. 2009.
- [193] V. Sidorkin, E. van Veldhoven, E. van der Drift, P. Alkemade, H. Salemink, and D. Maas, "Sub-10-nm nanolithography with a scanning helium beam," *J. Vac. Sci. Technol. B Microelectron. Nanom. Struct.*, vol. 27, no. 4, p. L18, Jul. 2009.
- [194] J. E. Mahan, *Physical vapor deposition of thin films*. WILEY-VCH Verlag Weinheim, 2000.
- [195] P. M. Martin, *Handbook of deposition technologies for films and coatings: science, applications and technology*. William Andrew, 2009.
- [196] I. Utke, P. Hoffmann, and J. Melngailis, "Gas-assisted focused electron beam and ion beam processing and fabrication," *J. Vac. Sci. Technol. B Microelectron. Nanom. Struct.*, vol. 26, no. 4, p. 1197, Aug. 2008.
- [197] M. Köhler, *Etching in microsystem technology*. John Wiley & Sons, 2008.
- [198] H. W. Lehmann, "Dry etching for pattern transfer," *J. Vac. Sci. Technol.*, vol. 17, no. 5, p. 1177, Sep. 1980.
- [199] P. Norgate and V. . Hammond, "Ion beam etching," *Phys. Technol.*, vol. 5, no. 3, pp. 186–203, Jan. 1974.
- [200] G. Götz and H. Karge, "Ion implantation into LiNbO₃," *Nucl. Instruments Methods Phys. Res.*, vol. 209–210, no. null, pp. 1079–1088, May 1983.
- [201] J. F. Ziegler, M. D. Ziegler, and J. P. Biersack, "SRIM – The stopping and range of ions in matter (2010)," *Nucl. Instruments Methods Phys. Res. Sect. B Beam Interact. with Mater. Atoms*, vol. 268, no. 11, pp. 1818–1823, 2010.
- [202] T. Gischkat, "Ionenstrahlverstärktes Ätzen für die 3D-Strukturierung von Lithiumniobat," Friedrich-Schiller-Universität Jena, 2010.
- [203] T. Baba, N. Fukaya, and J. Yonekura, "Observation of light propagation in photonic crystal optical waveguides with bends," *Electron. Lett.*, vol. 35, no. 8, p. 654, Apr. 1999.
- [204] S. Yamada, T. Koyama, Y. Katayama, N. Ikeda, Y. Sugimoto, K. Asakawa, N. Kawai, and K. Inoue, "Observation of light propagation in two-dimensional photonic crystal-based bent optical waveguides," *J. Appl. Phys.*, vol. 89, no. 2, p. 855, Jan. 2001.
- [205] M. Lončar, D. Nedeljković, T. P. Pearsall, J. Vučković, A. Scherer, S. Kuchinsky, and D. C. Allan, "Experimental and theoretical confirmation of Bloch-mode light propagation in planar photonic crystal waveguides," *Appl. Phys. Lett.*, vol. 80, no. 10, p. 1689, Mar. 2002.
- [206] S. Y. Lin, E. Chow, S. G. Johnson, and J. D. Joannopoulos, "Demonstration of highly efficient waveguiding in a photonic crystal slab at the 1.5- μm wavelength," *Opt. Lett.*, vol. 25, no. 17, p. 1297, Sep. 2000.
- [207] P. E. Barclay, K. Srinivasan, M. Borselli, and O. Painter, "Probing the dispersive and spatial properties of photonic crystal waveguides via highly efficient coupling from fiber tapers," *Appl. Phys. Lett.*, vol. 85, no. 1, p. 4, Jun. 2004.
- [208] S. I. Bozhevolnyi and L. Kuipers, "Near-field characterization of photonic crystal waveguides," *Semicond. Sci. Technol.*, vol. 21, no. 5, p. R1, 2006.
- [209] A. L. Campillo, J. W. P. Hsu, C. A. White, and A. Rosenberg, "Mapping the optical intensity distribution in photonic crystals using a near-field scanning optical microscope," *J. Appl. Phys.*, vol. 89, no. 5, p. 2801, Mar. 2001.
- [210] P. Kramper, M. Kafesaki, C. M. Soukoulis, A. Birner, F. Müller, U. Gsele, R. B.

- Wehrspohn, J. Mlynek, and V. Sandoghdar, "Near-field visualization of light confinement in a photonic crystal microresonator," *Opt. Lett.*, vol. 29, no. 2, p. 174, Jan. 2004.
- [211] H. Gersen, T. J. Karle, R. J. P. Engelen, W. Bogaerts, J. P. Korterik, N. F. van Hulst, T. F. Krauss, and L. Kuipers, "Real-Space Observation of Ultraslow Light in Photonic Crystal Waveguides," *Phys. Rev. Lett.*, vol. 94, no. 7, p. 073903, Feb. 2005.
- [212] J. C. Knight, G. Cheung, F. Jacques, and T. A. Birks, "Phase-matched excitation of whispering-gallery-mode resonances by a fiber taper," *Opt. Lett.*, vol. 22, no. 15, p. 1129, Aug. 1997.
- [213] T. J. Kippenberg, S. M. Spillane, D. K. Armani, and K. J. Vahala, "Fabrication and coupling to planar high-Q silica disk microcavities," *Appl. Phys. Lett.*, vol. 83, no. 4, p. 797, Jul. 2003.
- [214] P. E. Barclay, K. Srinivasan, M. Borselli, and O. Painter, "Efficient input and output fiber coupling to a photonic crystal waveguide," *Opt. Lett.*, vol. 29, no. 7, p. 697, Apr. 2004.
- [215] P. E. Barclay, K. Srinivasan, and O. Painter, "Nonlinear response of silicon photonic crystal micresonators excited via an integrated waveguide and fiber taper," *Opt. Express*, vol. 13, no. 3, p. 801, Feb. 2005.
- [216] D. Freeman, C. Grillet, M. W. Lee, C. L. C. Smith, Y. Ruan, A. Rode, M. Krolikowska, S. Tomljenovic-Hanic, C. M. de Sterke, M. J. Steel, B. Luther-Davies, S. Madden, D. J. Moss, Y.-H. Lee, and B. J. Eggleton, "Chalcogenide glass photonic crystals," *Photonics Nanostructures - Fundam. Appl.*, vol. 6, no. 1, pp. 3–11, Apr. 2008.
- [217] C. Schmidt, A. Chipouline, T. Pertsch, A. Tünnermann, O. Egorov, F. Lederer, and L. Deych, "Nonlinear thermal effects in optical microspheres at different wavelength sweeping speeds," *Opt. Express*, vol. 16, no. 9, p. 6285, Apr. 2008.
- [218] T. A. Birks and Y. W. Li, "The shape of fiber tapers," *J. Light. Technol.*, vol. 10, no. 4, pp. 432–438, Apr. 1992.
- [219] S. M. Spillane, T. J. Kippenberg, O. J. Painter, and K. J. Vahala, "Ideality in a Fiber-Taper-Coupled Microresonator System for Application to Cavity Quantum Electrodynamics," *Phys. Rev. Lett.*, vol. 91, no. 4, p. 043902, Jul. 2003.
- [220] K. Srinivasan and O. Painter, "Optical fiber taper coupling and high-resolution wavelength tuning of microdisk resonators at cryogenic temperatures," *Appl. Phys. Lett.*, vol. 90, no. 3, p. 031114, Jan. 2007.
- [221] K. Srinivasan, A. Stintz, S. Krishna, and O. Painter, "Photoluminescence measurements of quantum-dot-containing semiconductor microdisk resonators using optical fiber taper waveguides," *Phys. Rev. B*, vol. 72, no. 20, p. 205318, Nov. 2005.
- [222] J. Hendrickson, B. C. Richards, J. Sweet, S. Mosor, C. Christenson, D. Lam, G. Khitrova, H. M. Gibbs, T. Yoshie, A. Scherer, O. B. Shchekin, and D. G. Deppe, "Quantum dot photonic-crystal-slab nanocavities: Quality factors and lasing," *Phys. Rev. B*, vol. 72, no. 19, p. 193303, Nov. 2005.
- [223] C.-H. Hou, M.-P. Bernal, C.-C. Chen, R. Salut, C. Sada, N. Argiolas, M. Bazzan, and M. V. Ciampolillo, "Purcell effect observation in erbium doped lithium niobate photonic crystal structures," *Opt. Commun.*, vol. 281, no. 15–16, pp. 4151–4154, Aug. 2008.
- [224] M. W. McCutcheon, G. W. Rieger, I. W. Cheung, J. F. Young, D. Dalacu, S. Frédérick, P. J. Poole, G. C. Aers, R. L. Williams, and S. Frédérick, "Resonant scattering and

- second-harmonic spectroscopy of planar photonic crystal microcavities,” *Appl. Phys. Lett.*, vol. 87, no. 22, p. 221110, Nov. 2005.
- [225] L. Cai, Y. Wang, and H. Hu, “Low-loss waveguides in a single-crystal lithium niobate thin film,” *Opt. Lett.*, vol. 40, no. 13, p. 3013, Jun. 2015.
- [226] R. Geiss, J. Brandt, H. Hartung, A. Tünnermann, T. Pertsch, E.-B. Kley, and F. Schrempel, “Photonic microstructures in lithium niobate by potassium hydroxide-assisted ion beam-enhanced etching,” *J. Vac. Sci. Technol. B, Nanotechnol. Microelectron. Mater. Process. Meas. Phenom.*, vol. 33, no. 1, p. 010601, Jan. 2015.
- [227] A. Lapitskii, L. Shishkina, M. Pchelkina, and B. Stepanov, “ISSLEDOVANIE RASTVORIMOSTI BEZVODNYKH METANIوباتOV SHCHELOCHNYKH METALLOV METODOM MECHENYKH ATOMOV,” *ZHURNAL Obs. KHIMII*, vol. 25, no. 10, pp. 1862–1866, 1955.
- [228] K. J. Laidler, *Chemical kinetics*, 3rd ed. Prentice Hall, 1987.
- [229] Y. Q. Fu, N. K. A. Bryan, O. N. Shing, and N. P. Hung, “Influence of the Redeposition effect for Focused Ion Beam 3D Micromachining in Silicon,” *Int. J. Adv. Manuf. Technol.*, vol. 16, no. 12, pp. 877–880, Oct. 2000.
- [230] R. Geiss, S. Diziain, M. Steinert, F. Schrempel, E.-B. B. Kley, A. Tünnermann, and T. Pertsch, “Photonic crystals in lithium niobate by combining focussed ion beam writing and ion-beam enhanced etching,” *Phys. Status Solidi Appl. Mater. Sci.*, vol. 2425, no. 10, pp. 2421–2425, Jun. 2014.
- [231] R. Kremer, A. Boudrioua, P. Moretti, and J. Loulergue, “Measurements of the non-linear d33 coefficients of light-ion implanted lithium niobate by second harmonic generation in total reflection geometry,” *Opt. Commun.*, vol. 219, no. 1–6, pp. 389–393, Apr. 2003.
- [232] O. Vazquez-Mena, L. Gross, S. Xie, L. G. Villanueva, and J. Brugger, “Resistless nanofabrication by stencil lithography: A review,” *Microelectron. Eng.*, vol. 132, pp. 236–254, Jan. 2015.
- [233] H. Yun, S. Kim, H. Kim, J. Lee, K. McAllister, J. Kim, S. Pyo, J. Sung Kim, E. E. B. Campbell, W. Hyung Lee, and S. Wook Lee, “Stencil nano lithography based on a nanoscale polymer shadow mask: towards organic nanoelectronics,” *Sci. Rep.*, vol. 5, p. 10220, Jan. 2015.
- [234] L. Li, I. Bayn, M. Lu, C.-Y. Nam, T. Schröder, A. Stein, N. C. Harris, and D. Englund, “Nanofabrication on unconventional substrates using transferred hard masks,” *Sci. Rep.*, vol. 5, p. 7802, Jan. 2015.
- [235] S. Saravi, S. Diziain, M. Zilk, F. Setzpfandt, and T. Pertsch, “Phase-matched second-harmonic generation in slow-light photonic crystal waveguides,” *Phys. Rev. A*, vol. 92, no. 6, p. 063821, Dec. 2015.
- [236] S. Konno, T. Kojima, S. Fujikawa, and K. Yasui, “High-average-power, high-repetition, diode-pumped third-harmonic Nd:YAG laser,” in *Technical Digest. Summaries of papers presented at the Conference on Lasers and Electro-Optics. Postconference Technical Digest (IEEE Cat. No.01CH37170)*, 2001, p. 391.
- [237] B. Corcoran, C. Monat, C. Grillet, D. J. Moss, B. J. Eggleton, T. P. White, L. O’Faolain, and T. F. Krauss, “Green light emission in silicon through slow-light enhanced third-harmonic generation in photonic-crystal waveguides,” *Nat. Photonics*, vol. 3, no. 4, pp. 206–210, Mar. 2009.
- [238] F. Kajzar and R. Reinisch, Eds., *Beam Shaping and Control with Nonlinear Optics*, vol. 369. Boston: Kluwer Academic Publishers, 2002.

- [239] G. R. Meredith, "Cascading in optical third-harmonic generation by crystalline quartz," *Phys. Rev. B*, vol. 24, no. 10, pp. 5522–5532, Nov. 1981.
- [240] S. M. Saitel, A. A. Sukhorukov, and Y. S. Kivshar, "Chapter 1 – Multistep parametric processes in nonlinear optics," in *Progress in Optics*, vol. 47, 2005, pp. 1–73.
- [241] M. Marangoni, M. Lobino, and R. Ramponi, "Simultaneously phase-matched second- and third-harmonic generation from 1.55 μm radiation in annealed proton-exchanged periodically poled lithium niobate waveguides," *Opt. Lett.*, vol. 31, no. 18, p. 2707, Sep. 2006.
- [242] A. S. Solntsev, A. A. Sukhorukov, D. N. Neshev, R. Iliew, R. Geiss, T. Pertsch, and Y. S. Kivshar, "Cascaded third harmonic generation in lithium niobate nanowaveguides," *Appl. Phys. Lett.*, vol. 98, no. 23, p. 231110, 2011.
- [243] C. J. Barrelet, H.-S. Ee, S.-H. Kwon, and H.-G. Park, "Nonlinear mixing in nanowire subwavelength waveguides," *Nano Lett.*, vol. 11, no. 7, pp. 3022–5, Jul. 2011.
- [244] X. Zhang, H. He, J. Fan, C. Gu, X. Yan, M. Hu, X. Zhang, X. Ren, and C. Wang, "Sum frequency generation in pure zinc-blende GaAs nanowires," *Opt. Express*, vol. 21, no. 23, pp. 28432–7, Nov. 2013.
- [245] R. Grange, G. Brönstrup, M. Kiometzis, A. Sergeyeu, J. Richter, C. Leiterer, W. Fritzsche, C. Gutsche, A. Lysov, W. Prost, F.-J. Tegude, T. Pertsch, A. Tünnermann, and S. Christiansen, "Far-field imaging for direct visualization of light interferences in GaAs nanowires," *Nano Lett.*, vol. 12, pp. 5412–5417, Sep. 2012.
- [246] A. Casadei, E. F. Pecora, J. Trevino, C. Forestiere, D. Ruffer, E. Russo-averchi, F. Matteini, A. Fontcuberta i Morral, E. Russo-averchi, G. Tutuncuoglu, M. Heiss, and L. D. Negro, "Photonic-plasmonic coupling of GaAs single nanowires to optical nanoantennas," *Nano Lett.*, vol. 14, no. 5, pp. 2271–8, May 2014.
- [247] W. H. P. Pernice, C. Xiong, C. Schuck, and H. X. Tang, "Second harmonic generation in phase matched aluminum nitride waveguides and micro-ring resonators," *Appl. Phys. Lett.*, vol. 100, no. 22, p. 223501, May 2012.
- [248] R. Sanatinia, S. Anand, and M. Swillo, "Modal Engineering of Second-Harmonic Generation in Single GaP Nanopillars," *Nano Lett.*, vol. 14, no. 9, pp. 5376–81, Sep. 2014.
- [249] Y. Nakayama, P. J. Pauzauskie, A. Radenovic, R. M. Onorato, R. J. Saykally, J. Liphardt, and P. Yang, "Tunable nanowire nonlinear optical probe," *Nature*, vol. 447, no. 7148, pp. 1098–101, Jun. 2007.
- [250] A. Sergeyeu, R. Geiss, A. S. Solntsev, A. Steinbrück, F. Schrepel, E.-B. Kley, T. Pertsch, and R. Grange, "Second-harmonic generation in lithium niobate nanowires for local fluorescence excitation," *Opt. Express*, vol. 21, no. 16, pp. 19012–19021, Aug. 2013.
- [251] I. Shoji, T. Kondo, A. Kitamoto, M. Shirane, and R. Ito, "Absolute scale of second-order nonlinear-optical coefficients," *J. Opt. Soc. Am. B*, vol. 14, no. 9, pp. 17–19, 1997.
- [252] R. S. Wagner and W. C. Ellis, "VAPOR-LIQUID-SOLID MECHANISM OF SINGLE CRYSTAL GROWTH," *Appl. Phys. Lett.*, vol. 4, no. 5, p. 89, Dec. 1964.
- [253] M. Moewe, L. C. Chuang, S. Crankshaw, C. Chase, and C. Chang-Hasnain, "Atomically sharp catalyst-free wurtzite GaAs/AlGaAs nanoneedles grown on silicon," *Appl. Phys. Lett.*, vol. 93, no. 2, p. 023116, Jul. 2008.
- [254] M. S. Gudixsen and C. M. Lieber, "Diameter-Selective Synthesis of Semiconductor Nanowires," *J. Am. Chem. Soc.*, vol. 122, no. 36, pp. 8801–8802, Sep. 2000.

- [255] D. Staedler, T. Magouroux, C. Kasparian, G. Clarke, M. Germann, S. Schwung, R. Le Dantec, Y. Mugnier, D. Rytz, D. Ciepielewski, C. Galez, S. Gerber-lemaire, L. Juillerat-jeanneret, L. Bonacina, and J. Wolf, "Harmonic nanocrystals for biolabeling: a survey of optical properties and biocompatibility," *ACS Nano*, no. 3, pp. 2542–2549, 2012.
- [256] F. Dutto, C. Raillon, K. Schenk, and A. Radenovic, "Nonlinear optical response in single alkaline niobate nanowires," *Nano Lett.*, vol. 11, no. 6, pp. 2517–21, Jun. 2011.
- [257] H. He, X. Zhang, X. Yan, L. Huang, and C. Gu, "Broadband second harmonic generation in GaAs nanowires by femtosecond laser sources Broadband second harmonic generation in GaAs nanowires by femtosecond laser sources," *Appl. Phys. Lett.*, vol. 103, pp. 143110–4, 2013.
- [258] A. C. Santulli, H. Zhou, S. Berweger, M. B. Raschke, E. Sutter, and S. S. Wong, "Synthesis of single-crystalline one-dimensional LiNbO₃ nanowires," *CrystEngComm*, vol. 12, no. 10, p. 2675, 2010.
- [259] W. S. Yang, H.-Y. Lee, W. K. Kim, and D. H. Yoon, "Asymmetry ridge structure fabrication and reactive ion etching of LiNbO₃," *Opt. Mater. (Amst.)*, vol. 27, no. 10, pp. 1642–1646, Sep. 2005.
- [260] R. Geiss, A. Sergeev, H. Hartung, A. S. Solntsev, A. A. Sukhorukov, R. Grange, F. Schrepel, E.-B. Kley, A. Tünnermann, and T. Pertsch, "Fabrication of free-standing lithium niobate nanowaveguides down to 50 nm in width," *Nanotechnology*, vol. 27, no. 6, p. 065301, Feb. 2016.
- [261] A. Sergeev, R. Geiss, A. S. Solntsev, A. A. Sukhorukov, F. Schrepel, T. Pertsch, and R. Grange, "Enhancing Waveguided Second-Harmonic in Lithium Niobate Nanowires," *ACS Photonics*, p. 150603160227007, Jun. 2015.
- [262] L. Tong, R. R. Gattass, J. B. Ashcom, S. He, J. Lou, M. Shen, I. Maxwell, and E. Mazur, "Subwavelength-diameter silica wires for low-loss optical wave guiding.," *Nature*, vol. 426, no. 6968, pp. 816–9, Dec. 2003.
- [263] M. A. Foster, K. D. Moll, and A. L. Gaeta, "Optimal waveguide dimensions for nonlinear interactions," *Opt. Express*, vol. 12, no. 13, p. 2880, 2004.
- [264] J. Meier, W. S. Mohammed, A. Jugessur, L. Qian, M. Mojahedi, and J. S. Aitchison, "Group velocity inversion in AlGaAs nanowires," *Opt. Express*, vol. 15, no. 20, p. 12755, Oct. 2007.
- [265] A. C. Turner, C. Manolatou, B. S. Schmidt, M. Lipson, M. A. Foster, J. E. Sharping, and A. L. Gaeta, "Tailored anomalous group-velocity dispersion in silicon channel waveguides," *Opt. Express*, vol. 14, no. 10, p. 4357, 2006.
- [266] M. A. Foster, A. C. Turner, J. E. Sharping, B. S. Schmidt, M. Lipson, and A. L. Gaeta, "Broad-band optical parametric gain on a silicon photonic chip.," *Nature*, vol. 441, no. 7096, pp. 960–3, Jun. 2006.
- [267] I.-W. Hsieh, X. Chen, X. Liu, J. I. Dadap, N. C. Panoiu, C.-Y. Chou, F. Xia, W. M. Green, Y. A. Vlasov, and R. M. Osgood, "Supercontinuum generation in silicon photonic wires," *Opt. Express*, vol. 15, no. 23, p. 15242, Nov. 2007.
- [268] M. R. Lamont, B. Luther-Davies, D.-Y. Choi, S. Madden, and B. J. Eggleton, "Supercontinuum generation in dispersion engineered highly nonlinear ($\gamma = 10$ /W/m) As₂S₃ chalcogenide planar waveguide," *Opt. Express*, vol. 16, no. 19, p. 14938, Sep. 2008.
- [269] K. Harada, H. Takesue, H. Fukuda, T. Tsuchizawa, T. Watanabe, K. Yamada, Y. Tokura, and S. Itabashi, "Generation of high-purity entangled photon pairs using

- silicon wire waveguide,” *Opt. Express*, vol. 16, no. 25, p. 20368, Nov. 2008.
- [270] J. E. Sharping, K. F. Lee, M. A. Foster, A. C. Turner, B. S. Schmidt, M. Lipson, A. L. Gaeta, and P. Kumar, “Generation of correlated photons in nanoscale silicon waveguides,” *Opt. Express*, vol. 14, no. 25, p. 12388, 2006.
- [271] X. Yu, L. Scaccabarozzi, J. S. Harris, Jr., P. S. Kuo, and M. M. Fejer, “Efficient continuous wave second harmonic generation pumped at 1.55 μm in quasi-phase-matched AlGaAs waveguides,” *Opt. Express*, vol. 13, no. 26, p. 10742, 2005.
- [272] P. Sarrafi, E. Y. Zhu, B. M. Holmes, D. C. Hutchings, S. Aitchison, and L. Qian, “High-visibility two-photon interference of frequency-time entangled photons generated in a quasi-phase-matched AlGaAs waveguide,” *Opt. Lett.*, vol. 39, no. 17, pp. 5188–91, Sep. 2014.
- [273] P. Sarrafi, E. Y. Zhu, K. Dolgaleva, B. M. Holmes, D. C. Hutchings, J. S. Aitchison, and L. Qian, “Continuous-wave quasi-phase-matched waveguide correlated photon pair source on a III–V chip,” *Appl. Phys. Lett.*, vol. 103, no. 25, p. 251115, Dec. 2013.
- [274] D. Duchesne, K. A. Rutkowska, M. Volatier, F. Légaré, S. Delprat, M. Chaker, D. Modotto, A. Locatelli, C. De Angelis, M. Sorel, D. N. Christodoulides, G. Salamo, R. Arès, V. Aimez, and R. Morandotti, “Second harmonic generation in AlGaAs photonic wires using low power continuous wave light,” *Opt. Express*, vol. 19, no. 13, pp. 12408–17, Jun. 2011.
- [275] R. Regener, W. Sohler, and A. Physik, “Loss in low-finesse Ti:LiNbO₃ optical waveguide resonators,” *Appl. Phys. B Photophysics Laser Chem.*, vol. 36, no. 3, pp. 143–147, Mar. 1985.
- [276] R. Schiek, Y. Baek, and G. I. Stegeman, “Second-harmonic generation and cascaded nonlinearity in titanium-indiffused lithium niobate channel waveguides,” *J. Opt. Soc. Am. B*, vol. 15, no. 8, pp. 2255–2268, 1998.
- [277] T. Pertsch, R. Iwanow, R. Schiek, G. I. Stegeman, U. Peschel, F. Lederer, Y. H. Min, and W. Sohler, “Spatial ultrafast switching and frequency conversion in lithium niobate waveguide arrays,” *Opt. Lett.*, vol. 30, no. 2, p. 177, Jan. 2005.
- [278] M. Soljačić, C. Luo, J. D. Joannopoulos, and S. Fan, “Nonlinear photonic crystal microdevices for optical integration,” *Opt. Lett.*, vol. 28, no. 8, p. 637, Apr. 2003.
- [279] R. Iliew, C. Etrich, U. Peschel, and F. Lederer, “Microsized optical parametric oscillator in photonic crystals,” in *Lasers and Electro-Optics Europe, 2005. CLEO/Europe. 2005 Conference on*, 2005, p. 262–.
- [280] R. Iliew, C. Etrich, U. Peschel, and F. Lederer, “Microsized optical parametric oscillator in a photonic crystal,” *Sel. Top. Quantum Electron. IEEE J.*, vol. 12, no. 3, pp. 377–382, May 2006.
- [281] C. Deng, J. W. Haus, A. Sarangan, A. Mahfoud, C. Sibia, M. Scalora, and A. Zheltikov, “Photonic band-gap enhanced second-harmonic generation in a planar lithium niobate waveguide,” *Laser Phys.*, vol. 16, no. 6, pp. 927–947, Jun. 2006.
- [282] R. Iliew, F. Lederer, C. Etrich, and T. Pertsch, “Optical Parametric Oscillator in a Lithium Niobate Photonic Crystal Membrane,” in *Lasers and Electro-Optics, 2007 and the International Quantum Electronics Conference. CLEOE-IQEC 2007. European Conference on*, 2007, p. 1.
- [283] R. Iliew, C. Etrich, T. Pertsch, and F. Lederer, “Slow-light enhanced collinear second-harmonic generation in two-dimensional photonic crystals,” *Phys. Rev. B (Condensed Matter Mater. Physics)*, vol. 77, no. 11, p. 115124, Mar. 2008.
- [284] R. Iliew, C. Etrich, T. Pertsch, F. Lederer, and Y. S. Kivshar, “Huge enhancement of

- backward second-harmonic generation with slow light in photonic crystals,” *Phys. Rev. A*, vol. 81, no. 2, p. 23820, Feb. 2010.
- [285] J. Amet, F. I. Baida, G. W. Burr, and M.-P. Bernal, “The superprism effect in lithium niobate photonic crystals for ultra-fast, ultra-compact electro-optical switching,” *Photonics Nanostructures - Fundam. Appl.*, vol. 6, no. 1, pp. 47–59, Apr. 2008.
- [286] H. Hartung, R. Geiss, T. Gischkat, F. Schrempel, R. Iliew, T. Pertsch, F. Lederer, W. Wesch, E. B. Kley, and A. Tunnermann, “Photonic crystals in lithium niobate by ion-beam enhanced etching,” *2009 IEEELEOS Winter Top. Meet. Ser.*, pp. 64–65, 2009.
- [287] R. Geiss, S. Diziain, R. Iliew, C. Etrich, H. Hartung, N. Janunts, F. Schrempel, F. Lederer, T. Pertsch, and E.-B. Kley, “Light propagation in a free-standing lithium niobate photonic crystal waveguide,” *Appl. Phys. Lett.*, vol. 97, no. 13, p. 131109, 2010.
- [288] G. W. Burr, S. Diziain, and M.-P. Bernal, “Theoretical study of lithium niobate slab waveguides for integrated optics applications,” *Opt. Mater. (Amst.)*, vol. 31, no. 10, pp. 1492–1497, 2009.
- [289] S. Diziain, R. Geiss, M. Steinert, C. Schmidt, W.-K. Chang, S. Fasold, D. Föbel, Y.-H. Chen, and T. Pertsch, “Self-suspended micro-resonators patterned in Z-cut lithium niobate membranes,” *Opt. Mater. Express*, vol. 5, no. 9, p. 2081, Aug. 2015.
- [290] S. I. Bozhevolnyi, V. S. Volkov, T. Søndergaard, A. Boltasseva, P. I. Borel, M. Kristensen, T. Søndergaard, A. Boltasseva, P. I. Borel, and M. Kristensen, “Near-field imaging of light propagation in photonic crystal waveguides: Explicit role of Bloch harmonics,” *Phys. Rev. B*, vol. 66, no. 23, p. 235204, Dec. 2002.
- [291] S. I. Bozhevolnyi, B. Vohnsen, and E. A. Bozhevolnaya, “Transfer functions in collection scanning near-field optical microscopy,” *Opt. Commun.*, vol. 172, no. 1–6, pp. 171–179, Dec. 1999.
- [292] S. I. Bozhevolnyi and B. Vohnsen, “Near-field imaging of optical phase and its singularities,” *Opt. Commun.*, vol. 212, no. 4–6, pp. 217–223, Nov. 2002.
- [293] S. I. Bozhevolnyi, V. S. Volkov, T. Søndergaard, A. Boltasseva, P. I. Borel, and M. Kristensen, “Near-field imaging of light propagation in photonic crystal waveguides: Explicit role of Bloch harmonics,” *Phys. Rev. B*, vol. 66, no. 23, p. 235204, Dec. 2002.
- [294] S. Bin Hasan, C. Rockstuhl, T. Pertsch, and F. Lederer, “Second-order nonlinear frequency conversion processes in plasmonic slot waveguides,” *J. Opt. Soc. Am. B*, vol. 29, no. 7, p. 1606, Jun. 2012.
- [295] D. K. Gramotnev and S. I. Bozhevolnyi, “Plasmonics beyond the diffraction limit,” *Nat. Photonics*, vol. 4, no. 2, pp. 83–91, Jan. 2010.
- [296] S. Kim, J. Jin, Y.-J. Kim, I.-Y. Park, Y. Kim, and S.-W. Kim, “High-harmonic generation by resonant plasmon field enhancement,” *Nature*, vol. 453, no. 7196, pp. 757–60, Jun. 2008.
- [297] K. Chen, C. Durak, J. R. Heflin, and H. D. Robinson, “Plasmon-enhanced second-harmonic generation from ionic self-assembled multilayer films,” *Nano Lett.*, vol. 7, no. 2, pp. 254–8, Mar. 2007.
- [298] A. Di Falco, C. Conti, and G. Assanto, “Quadratic phase matching in slot waveguides,” *Opt. Lett.*, vol. 31, no. 21, p. 3146, Nov. 2006.
- [299] L. Liu, Z. Han, and S. He, “Novel surface plasmon waveguide for high integration,” *Opt. Express*, vol. 13, no. 17, p. 6645, Aug. 2005.
- [300] A. B. Matsko and V. S. Ilchenko, “Optical resonators with whispering-gallery modes-

- part I: basics,” *IEEE J. Sel. Top. Quantum Electron.*, vol. 12, no. 1, pp. 3–14, Jan. 2006.
- [301] V. S. Ilchenko and A. B. Matsko, “Optical resonators with whispering-gallery modes—part II: applications,” *IEEE J. Sel. Top. Quantum Electron.*, vol. 12, no. 1, pp. 15–32, Jan. 2006.
- [302] B. J. M. Hausmann, I. Bulu, V. Venkataraman, P. Deotare, and M. Lončar, “Diamond nonlinear photonics,” *Nat. Photonics*, vol. 8, no. 5, pp. 369–374, Apr. 2014.
- [303] C. Xiong, W. Pernice, K. K. Ryu, C. Schuck, K. Y. Fong, T. Palacios, and H. X. Tang, “Integrated GaN photonic circuits on silicon (100) for second harmonic generation,” *Opt. Express*, vol. 19, no. 11, p. 10462, May 2011.
- [304] B. Gayral, J. M. Gérard, A. Lemaître, C. Dupuis, L. Manin, and J. L. Pelouard, “High-Q wet-etched GaAs microdisks containing InAs quantum boxes,” *Appl. Phys. Lett.*, vol. 75, no. 13, p. 1908, Sep. 1999.
- [305] M. Soltani, S. Yegnanarayanan, and A. Adibi, “Ultra-high Q planar silicon microdisk resonators for chip-scale silicon photonics,” *Opt. Express*, vol. 15, no. 8, p. 4694, Apr. 2007.
- [306] H. Cai and A. W. Poon, “Optical manipulation of microparticles using whispering-gallery modes in a silicon nitride microdisk resonator,” *Opt. Lett.*, vol. 36, no. 21, p. 4257, Oct. 2011.
- [307] C. Schmidt, A. Chipouline, T. Käsebier, E.-B. Kley, A. Tünnermann, and T. Pertsch, “Thermal nonlinear effects in hybrid silica/polymer microdisks,” *Opt. Lett.*, vol. 35, no. 20, p. 3351, Oct. 2010.
- [308] Y. Akahane, T. Asano, B.-S. S. Song, and S. Noda, “High-Q photonic nanocavity in a two-dimensional photonic crystal,” *Nature*, vol. 425, no. 6961, pp. 944–947, Oct. 2003.
- [309] J. Vuckovic, M. Loncar, H. Mabuchi, and A. Scherer, “Optimization of the Q factor in photonic crystal microcavities,” *Quantum Electron. IEEE J.*, vol. 38, no. 7, pp. 850–856, 2002.
- [310] K. Srinivasan and O. Painter, “Momentum space design of high-Q photonic crystal optical cavities,” *Opt. Express*, vol. 10, no. 15, pp. 670–684, 2002.
- [311] N.-V.-Q. Tran, S. Combrié, A. De Rossi, and A. De Rossi, “Directive emission from high-Q photonic crystal cavities through band folding,” *Phys. Rev. B (Condensed Matter Mater. Physics)*, vol. 79, no. 4, p. 41101, Jan. 2009.
- [312] S. L. Portalupi, M. Galli, C. Reardon, T. F. Krauss, L. O’Faolain, L. C. Andreani, and D. Gerace, “Planar photonic crystal cavities with far-field optimization for high coupling efficiency and quality factor,” *Opt. Express*, vol. 18, no. 15, pp. 16064–73, Jul. 2010.
- [313] A. F. Oskooi, D. Roundy, M. Ibanescu, P. Bermel, J. D. Joannopoulos, and S. G. Johnson, “Meep: A flexible free-software package for electromagnetic simulations by the FDTD method,” *Comput. Phys. Commun.*, vol. 181, no. 3, pp. 687–702, Mar. 2010.
- [314] H. Altug and J. Vuckovic, “Polarization control and sensing with two-dimensional coupled photonic crystal microcavity arrays,” *Opt. Lett.*, vol. 30, no. 9, p. 982, May 2005.
- [315] S. Diziain, R. Geiss, M. Zilk, F. Schrempel, E.-B. Kley, A. Tünnermann, and T. Pertsch, “Mode analysis of photonic crystal L3 cavities in self-suspended lithium niobate membranes,” *Appl. Phys. Lett.*, vol. 103, no. 25, p. 251101, Dec. 2013.
- [316] S. Diziain, R. Geiss, M. Zilk, F. Schrempel, E.-B. Kley, A. Tünnermann, and T.

- Pertsch, "Second harmonic generation in free-standing lithium niobate photonic crystal L3 cavity," *Appl. Phys. Lett.*, vol. 103, no. 5, p. 51117, 2013.
- [317] K. Rivoire, Z. Lin, F. Hatami, W. T. Masselink, and J. Vučković, "Second harmonic generation in gallium phosphide photonic crystal nanocavities with ultralow continuous wave pump power," *Opt. Express*, vol. 17, no. 25, pp. 22609–22615, 2009.
- [318] M. W. McCutcheon, J. F. Young, G. W. Rieger, D. Dalacu, S. Frédérick, P. J. Poole, and R. L. Williams, "Experimental demonstration of second-order processes in photonic crystal microcavities at submilliwatt excitation powers," *Phys. Rev. B*, vol. 76, no. 24, p. 245104, Dec. 2007.
- [319] J. Chan, A. H. Safavi-Naeini, J. T. Hill, S. Meenehan, and O. Painter, "Optimized optomechanical crystal cavity with acoustic radiation shield," *Appl. Phys. Lett.*, vol. 101, no. 8, p. 081115, Aug. 2012.
- [320] R. Ohta, Y. Ota, M. Nomura, N. Kumagai, S. Ishida, S. Iwamoto, and Y. Arakawa, "Strong coupling between a photonic crystal nanobeam cavity and a single quantum dot," *Appl. Phys. Lett.*, vol. 98, no. 17, p. 173104, Apr. 2011.
- [321] K.-Y. Jeong, Y.-S. No, Y. Hwang, K. S. Kim, M.-K. Seo, H.-G. Park, and Y.-H. Lee, "Electrically driven nanobeam laser," *Nat. Commun.*, vol. 4, Nov. 2013.
- [322] Y. Chen, W. S. Fegadolli, W. M. Jones, A. Scherer, and M. Li, "Ultrasensitive Gas-Phase Chemical Sensing Based on Functionalized Photonic Crystal Nanobeam Cavities," *ACS Nano*, vol. 8, no. 1, pp. 522–527, Jan. 2014.
- [323] Q. Quan, P. B. Deotare, and M. Loncar, "Photonic crystal nanobeam cavity strongly coupled to the feeding waveguide," *Appl. Phys. Lett.*, vol. 96, no. 20, p. 203102, May 2010.
- [324] Q. Quan and M. Loncar, "Deterministic design of wavelength scale, ultra-high Q photonic crystal nanobeam cavities.," *Opt. Express*, vol. 19, no. 19, pp. 18529–42, Sep. 2011.

Publications

Journals

- R. Geiss, A. Sergeyevev, H. Hartung, A. S. Solntsev, A. A. Sukhorukov, R. Grange, F. Schrempel, E.-B. Kley, A. Tünnermann, and T. Pertsch, "Fabrication of free-standing lithium niobate nanowaveguides down to 50 nm in width," *Nanotechnology* **27**, 065301 (2016).
- M. Fruhnert, F. Kretschmer, R. Geiss, I. Perevyazko, D. Cialla-May, M. Steinert, N. Janunts, D. Sivun, S. Hoepfener, M. D. Hager, T. Pertsch, U. S. Schubert, and C. Rockstuhl, "Synthesis, Separation, and Hypermethod Characterization of Gold Nanoparticle Dimers Connected by a Rigid Rod Linker," *J. Phys. Chem. C* **150713161159006** (2015).
- R. Geiss, S. Saravi, A. Sergeyevev, S. Diziain, F. Setzpfandt, F. Schrempel, R. Grange, E.-B. Kley, A. Tünnermann, and T. Pertsch, "Fabrication of nanoscale lithium niobate waveguides for second-harmonic generation," *Opt. Lett.* **40**, 2715–2718 (2015).
- H. P. Chung, W. K. Chang, C. H. Tseng, R. Geiss, T. Pertsch, and Y. H. Chen, "Electro-optically spectrum tailorable intracavity optical parametric oscillator," *Opt. Lett.* **40**, 5132 (2015).
- E. Pshenay-Severin, I. Mukhin, S. Fasold, R. Geiss, A. Steinbrück, R. Grange, A. Chipouline, and T. Pertsch, "Relaxation time mapping of single quantum dots and substrate background fluorescence," *Письма в ЖЭТФ* **102**, 3 (2015).
- A. Sergeyevev, R. Geiss, A. S. Solntsev, A. A. Sukhorukov, F. Schrempel, T. Pertsch, and R. Grange, "Enhancing Waveguided Second-Harmonic in Lithium Niobate Nanowires," *ACS Photonics* **150603160227007** (2015).
- R. Geiss, J. Brandt, H. Hartung, A. Tünnermann, T. Pertsch, E.-B. Kley, and F. Schrempel, "Photonic microstructures in lithium niobate by potassium hydroxide-assisted ion beam-enhanced etching," *J. Vac. Sci. Technol. B, Nanotechnol. Microelectron. Mater. Process. Meas. Phenom.* **33**, 010601 (2015).
- S. Diziain, R. Geiss, M. Steinert, C. Schmidt, W.-K. Chang, S. Fasold, D. Füßel, Y.-H. Chen, and T. Pertsch, "Self-suspended micro-resonators patterned in Z-cut lithium niobate membranes," *Opt. Mater. Express* **5**, 2081 (2015).
- F. Kretschmer, M. Fruhnert, R. Geiss, U. Mansfeld, C. Höpfener, S. Hoepfener, C. Rockstuhl, T. Pertsch, and U. S. Schubert, "Plasmonic nanoparticle clusters with tunable plasmonic resonances in the visible spectral region," *J. Mater. Chem. C* **2**, 6415 (2014).
- R. Geiss, S. Diziain, M. Steinert, F. Schrempel, E.-B. B. Kley, A. Tünnermann, and T. Pertsch, "Photonic crystals in lithium niobate by combining focussed ion beam writing and ion-beam enhanced etching," *Phys. Status Solidi Appl. Mater. Sci.* **2425**, 2421–2425 (2014).
- A. Sergeyevev, R. Geiss, A. S. Solntsev, A. Steinbrück, F. Schrempel, E.-B. Kley, T. Pertsch, and R. Grange, "Second-harmonic generation in lithium niobate nanowires for local fluorescence excitation," *Opt. Express* **21**, 19012–19021 (2013).
- J. Thomas, V. Hilbert, R. Geiss, T. Pertsch, A. Tünnermann, and S. Nolte, "Quasi phase matching in femtosecond pulse volume structured x-cut lithium niobate," *Laser Photon. Rev.* (2013).
- S. Diziain, R. Geiss, M. Zilk, F. Schrempel, E.-B. Kley, A. Tünnermann, and T. Pertsch, "Mode analysis of photonic crystal L3 cavities in self-suspended lithium niobate membranes," *Appl. Phys. Lett.* **103**, 251101 (2013).

- F. Eilenberger, K. Prater, S. Minardi, R. Geiss, U. Röpke, J. Kobelke, K. Schuster, H. Bartelt, S. Nolte, A. Tünnermann, and T. Pertsch, "Observation of Discrete, Vortex Light Bullets," *Phys. Rev. X* **3**, 041031– (2013).
- S. Diziain, R. Geiss, M. Zilk, F. Schrempel, E.-B. Kley, A. Tünnermann, and T. Pertsch, "Second harmonic generation in free-standing lithium niobate photonic crystal L3 cavity," *Appl. Phys. Lett.* **103**, 51117 (2013).
- Y.-H. Chen, J.-W. Chang, C.-H. Lin, W.-K. Chang, N. Hsu, Y.-Y. Lai, Q.-H. Tseng, R. Geiss, T. Pertsch, and S. S. Yang, "Spectral narrowing and manipulation in an optical parametric oscillator using periodically poled lithium niobate electro-optic polarization-mode converters.," *Opt. Lett.* **36**, 2345–7 (2011).
- A. S. Solntsev, A. A. Sukhorukov, D. N. Neshev, R. Iliew, R. Geiss, T. Pertsch, and Y. S. Kivshar, "Cascaded third harmonic generation in lithium niobate nanowaveguides," *Appl. Phys. Lett.* **98**, 231110 (2011).
- R. Geiss, S. Diziain, R. Iliew, C. Etrich, H. Hartung, N. Janunts, F. Schrempel, F. Lederer, T. Pertsch, and E.-B. Kley, "Light propagation in a free-standing lithium niobate photonic crystal waveguide," *Appl. Phys. Lett.* **97**, 131109 (2010).
- R. Geiss, A. Chowdhury, C. M. Staus, H. M. Ng, S. S. Park, and J. Y. Han, "Low loss GaN at 1550 nm," *Appl. Phys. Lett.* **87**, 132107 (2005).

Conference Contributions

- S. Diziain, R. Geiss, M. Zilk, F. Schrempel, E.-B. Kley, A. Tünnermann, and T. Pertsch, "Enhancement of second harmonic generation in self-suspended lithium niobate photonic crystal cavities," in *2014 16th International Conference on Transparent Optical Networks (ICTON)* (IEEE, 2014), pp. 1–4.
- S. Diziain, R. Geiss, M. Zilk, F. Schrempel, E.-B. Kley, A. Tünnermann, and T. Pertsch, "Freestanding lithium niobate photonic crystal cavities for nonlinear optics applications," in *CLEO: 2013* (Optical Society of America, 2013), p. QTh4E.8.
- A. Sergeyev, R. Geiss, E.-B. Kley, T. Pertsch, and R. Grange, "Propagation of second-harmonic generation in LiNbO₃ nanowires," in *The European Conference on Lasers and Electro-Optics* (2013).
- R. Geiss, H. Hartung, S. Diziain, M. Steinert, F. Schrempel, E.-B. Kley, T. Pertsch, and A. Tünnermann, "Freestanding Photonic Crystals in Lithium Niobate," in *EIPBN, 57th International Conference on Electron, Ion, and Photon Beam Technology and Nanofabrication, Nashville, Tennessee* (2013).
- R. Geiss, H. Hartung, F. Schrempel, E.-B. Kley, T. Pertsch, and A. Tünnermann, "Lithium Niobate Nanowaveguides fabricated by Ion-Beam Enhanced Etching," in *EIPBN, 56th International Conference on Electron, Ion, and Photon Beam Technology and Nanofabrication, Waikoloa, Hawaii* (2012).
- R. Geiss, S. Diziain, R. Iliew, C. Etrich, F. Schrempel, F. Lederer, T. Pertsch, and E. B. Kley, "Transmission properties of a free-standing lithium niobate photonic crystal waveguide," *CLEO 2011 Laser Sci. to Photonic Appl.* 1–2 (2011).
- J. Thomas, V. Hilbert, R. Geiss, A. Tünnermann, and S. Nolte, "Femtosecond pulse written quasi phase matching element in x-cut lithium niobate," *2011 Conf. Lasers ElectroOptics Eur. 12th Eur. Quantum Electron. Conf. CLEO Eur.* 1–1 (2011).
- Y.-H. Chen, J.-W. Chang, Y.-Y. Lai, W.-K. Chang, N. Hsu, Q.-H. Tseng, R. Geiss, and T. Pertsch, "Spectral Narrowing and Manipulation in Optical Parametric Oscillator Using APPLN Electro-optic Polarization-mode Converter," in *CLEO:2011 - Laser Applications to Photonic Applications* (OSA, 2011), p. CMR4.

- I. Spaleniak, F. Giessler, R. Geiss, S. Minardi, T. Pertsch, R. Neuhaeuser, M. Becker, M. Rothhardt, F. Delplancke, A. Richichi, S. Ménardi, and C. Schmid, "MAMMUT: mirror vibration metrology for VLTI," in *Optical and Infrared Interferometry II*, W. C. Danchi, F. Delplancke, and J. K. Rajagopal, eds. (SPIE, 2010), Vol. 7734, p. 77343Y.
- R. Geiss, C. Helgert, H. Hartung, E. B. Kley, C. Rockstuhl, F. Schrempel, F. Lederer, A. Tünnermann, W. Wesch, and T. Pertsch, "Optical Metamaterials and Photonic Crystals: Aspects of Large-scale Micro- and Nanofabrication," in *Progress In Electromagnetics Research Symposium Abstracts, Xi'an, China, March 22, 26, 2010* (2010).
- H. Hartung, R. Geiss, T. Gischkat, F. Schrempel, E.-B. Kley, W. Wesch, and A. Tünnermann, "Freestanding Photonic Crystal Membranes in Lithium Niobate fabricated by Ion-Beam Enhanced Etching," in *EIPBN, 54th International Conference on Electron, Ion, and Photon Beam Technology and Nanofabrication, Anchorage, Alaska* (2010).
- R. Geiss, S. Diziain, H. Hartung, R. Iliew, C. Etrich, N. Janunts, F. Schrempel, F. Lederer, T. Pertsch, E.-B. Kley, and A. Tünnermann, "Light propagation in free standing lithium niobate photonic crystal membranes," in *NFO11, 11th International Conference on Near-Field Optics, Nanophotonics and Related Techniques, Aug 29 - Sept 2, 2010* (2010).
- R. Geiss, H. Hartung, R. Iliew, T. Gischkat, F. Schrempel, F. Setzpfandt, T. Pertsch, E.-B. Kley, F. Lederer, W. Wesch, and A. Tünnermann, "Radiation Losses of Photonic Crystal Waveguides in LiNbO₃ Membranes," in *Nonlinear Optics: Materials, Fundamentals and Applications* (Optical Society of America, 2009), p. NMD2.
- H. Hartung, R. Geiss, T. Gischkat, F. Schrempel, R. Iliew, T. Pertsch, F. Lederer, W. Wesch, E. B. Kley, and A. Tünnermann, "Photonic crystals in lithium niobate by ion-beam enhanced etching," 2009 IEEELEOS Winter Top. Meet. Ser. 64–65 (2009).
- F. Setzpfandt, R. Schiek, R. Geiss, W. Sohler, A. Tünnermann, and T. Pertsch, "Discrete Quadratic Solitons with Higher Order Modes in Lithium Niobate Waveguide Arrays," in *Nonlinear Optics: Materials, Fundamentals and Applications* (Optical Society of America, 2009), p. NMB6.
- C. H. Lin, W. K. Chang, Y.-H. C. Y.-H. Chen, S. Yang, R. Geiss, T. Pertsch, and A. Tünnermann, "Gain-enhanced and spectral-narrowed optical parametric oscillator using PPLN electro-optic polarization-mode converters," 2009 Conf. Lasers ElectroOptics 2009 Conf. Quantum Electron. Laser Sci. Conf. **1**, 3–4 (2009).
- R. Geiss, R. Schiek, T. Pertsch, A. Chipouline, O. Egorov, F. Lederer, W. Sohler, and A. Tünnermann, "Nonlinear effects in PPLN waveguide resonators," 2008 Conf. Lasers ElectroOptics 2008 Conf. Quantum Electron. Laser Sci. 1–2 (2008).
- C. Helgert, R. Geiss, E. Pshenay-Severin, T. Pertsch, E.-B. Kley, and A. Tünnermann, "Fabrication of large-area negative-index metamaterial by Electron-Beam-Lithography," in *EIPBN, 52th International Conference on Electron, Ion, and Photon Beam Technology and Nanofabrication, Portland, Oregon* (2008).
- H. M. Ng, R. Geiss, A. Chowdhury, M. Sergent, S. Srinivasan, and F. Ponce, "Optical Properties of GaN Nanowhiskers Produced by Photoelectrochemical Etching," *ECS Trans.* **3**, 415–419 (2006).

Acknowledgments

Besonderer Dank gilt Prof. Thomas Pertsch für die Bereitstellung und die inhaltliche Betreuung des Themas. Ernst-Bernhard Kley und Frank Schrepel danke ich für die umfassende Unterstützung in den Bereichen Mikrostrukturtechnik und Ionenstrahlphysik. Severine Diziain danke ich für die Zusammenarbeit, insbesondere beim Design und der optischen Charakterisierung photonischer Kristalle. Weiterhin sei allen gedankt, die zu dieser Arbeit direkt oder indirekt beigetragen haben.

Ehrenwörtliche Erklärung

Ich erkläre hiermit ehrenwörtlich, dass ich die vorliegende Arbeit selbständig, ohne unzulässige Hilfe Dritter und ohne Benutzung anderer als der angegebenen Hilfsmittel und Literatur angefertigt habe. Die aus anderen Quellen direkt oder indirekt übernommene Daten und Konzepte sind unter Angabe der Quelle gekennzeichnet. Bei der Auswahl und Auswertung folgenden Materials haben mir die nachstehend aufgeführten Personen in der jeweils beschriebenen Weise unentgeltlich geholfen:

1. Die Probenherstellung erfolgte unter der durch mich angeleiteten Beteiligung von Technikern und Kollegen der AG Mikrostrukturtechnik und der AG Nanooptik des IAP der FSU Jena. Unterstützung externer Partner wurde bei der CVD Beschichtung (Andreas Ihring, IPHT Jena) und bei der Ionenbestrahlung (Patrick Hoffmann, IFK, FSU Jena) in Anspruch genommen.
2. Juliane Brandt hat Versuche zum Ätzverhalten ionenbestrahlten LiNbO_3 in Hydroxidlösungen durchgeführt.
3. Rachel Grange, Anton Sergejev, Sina Saravi und Frank Setzpfandt waren an der experimentellen Untersuchung der optischen Eigenschaften nanoskaliger LiNbO_3 Rippenwellenleiter beteiligt.
4. Carsten Schmidt, Arstan Bisianov und Wei-Kun Chang waren an der experimentellen Untersuchung der optischen Eigenschaften von LiNbO_3 Mikrodiskresonatoren beteiligt.
5. Carsten Schmidt und Severine Diziain waren an der experimentellen Untersuchung der optischen Eigenschaften von LiNbO_3 Wellenleiterresonatoren aus photonischen Kristallen beteiligt.
6. SNOM Messungen und Messungen an LiNbO_3 Resonatoren aus photonischen Kristallen wurden von Severine Diziain durchgeführt.
7. Numerische Untersuchungen von photonischen Kristallen wurden von Rumen Iliew, Christoph Etrich und Severine Diziain durchgeführt.
8. Numerische Untersuchungen von nanoskaligen Rippenwellenleitern wurden von Alexander Solntsev, Anton Sergejev und Sina Saravi durchgeführt.
9. Numerische Untersuchungen von Mikrodiskresonatoren wurden von Carsten Schmidt und Severine Diziain durchgeführt.
10. An der Simulation von Ionenbestrahlung und Ätzen beim IBEE Verfahren war Holger Hartung beteiligt.
11. AFM Messungen zur Bestimmung der Oberflächenrauigkeit wurden von Severine Diziain durchgeführt.

Weitere Personen waren an der inhaltlich-materiellen Erstellung der vorliegenden Arbeit nicht beteiligt. Insbesondere habe ich hierfür nicht die entgeltliche Hilfe von Vermittlungs- bzw. Beratungsdiensten (Promotionsberater oder andere Personen) in Anspruch genommen. Niemand hat von mir unmittelbar oder mittelbar geldwerte Leistungen für Arbeiten erhalten, die im Zusammenhang mit dem Inhalt der vorgelegten Dissertation stehen.

Die Arbeit wurde bisher weder im In- noch im Ausland in gleicher oder ähnlicher Form einer anderen Prüfungsbehörde vorgelegt.

Die geltende Promotionsordnung der Physikalisch-Astronomischen Fakultät ist mir bekannt.

Ich versichere ehrenwörtlich, dass ich nach bestem Wissen die reine Wahrheit gesagt und nichts verschwiegen habe.